Energetically Efficient Control of Stochastic Thermodynamic Systems

by

Steven Blaber

M.Sc., University of Waterloo, 2019
B.Sc., Simon Fraser University, 2017

Thesis Submitted in Partial Fulfillment of the
Requirements for the Degree of
Doctor of Philosophy

in the
Department of Physics
Faculty of Science

SIMON FRASER UNIVERSITY
Spring 2023

Declaration of Committee

Name:	**Steven Blaber**
Degree:	**Doctor of Philosophy**
Thesis Title:	**Energetically Efficient Control of Stochastic Thermodynamic Systems**
Committee:	**Chair:** David Broun Associate Professor, Physics
	David Sivak Supervisor Associate Professor, Physics
	Nancy Forde Committee Member Professor, Physics
	John Bechhoefer Committee Member Professor, Physics
	Eldon Emberly Examiner Professor, Physics
	Sebastian Deffner External Examiner Associate Professor, Physics University of Maryland, Baltimore County

Abstract

This thesis presents recent advances in the optimal control of stochastic thermodynamic systems. It covers isothermal stochastic thermodynamics, including the use of linear response, thermodynamic geometry, and optimal transport. New techniques for identifying minimum-dissipation protocols for fast and strong control are introduced, and the thermodynamic-geometry framework is extended to minimizing higher-order moments of the work distribution. Higher-order corrections beyond linear response are also derived. These concepts are demonstrated using a model of driven barrier crossing relevant to DNA-hairpin experiments and applied to free-energy estimation.

Keywords: Optimal control; Thermodynamics; Stochastic; Biophysics

Acknowledgments

I thank my supervisor David Sivak for supporting and guiding me through my research at SFU, both during my Ph.D. and B.Sc.. Working with you has been a pleasure, and your mentorship has helped me grow into the researcher that I am today.

I would also like to thank the members of my advisory committee, Nancy Forde and John Bechhoefer, who have always been supportive and provided valuable advice and feedback during committee meetings, presentations, and poster sessions.

A special thank you to all current and former Sivak group members. The fun conversations in the office and discussions and feedback during group meeting have played an essential role in my progress throughout my PhD. I would especially like to thank Miranda Louwerse for working with me to develop STEP.

I give a heartfelt thank you to my partner Catherine Perkins. Your love and support has been vital to my success in all my studies. You have proof read so many documents and listened to many iterations of presentations with endless patience, I truly could not have done it without you.

I greatly appreciate the financial support I have received throughout my PhD, including the Graduate Dean's Entrance Scholarship awarded by SFU.

Table of Contents

List of Figures

Abbreviations

1P	one-parameter
2P	two-parameter
BAR	Bennett's acceptance ratio
CFCP	constrained final control parameter
CFD	constrained final distribution
CP	control parameter
FV	force variance
IFRR	initial force relaxation rate
LR	linear-response
STEP	short-time efficient protocol

List of Symbols

$\mathbf{r}$	position vector
x	one-dimensional position
t	time
Δt	protocol duration
Λ	parametric protocol
$\boldsymbol{\lambda}$	vector of control parameters
$p(\cdot)$	probability distribution
$P(\cdot)$	cumulative distribution
$\pi(\cdot)$	equilibrium probability distribution
$\Pi(\cdot)$	equilibrium cumulative distribution
$\mathcal{Q}(\cdot)$	quantile function
V_{tot}	total system energy
V_{land}	energy landscape
V_{trap}	quadratic trapping potential
$\mathbf{r}^{\mathrm{c}}$	trap-center vector
x^{c}	one-dimensional trap center
K	trap stiffness matrix
k	one-dimensional trap stiffness
E_{B}	barrier height
x_{m}	distance from minimum to barrier
ΔE	energy transduced per rotation
L	time-evolution operator
$\boldsymbol{v}$	mean local velocity
D	diffusivity
k_{B}	Boltzmann's constant
T	temperature
β	inverse temperature $\beta \equiv (k_{\mathrm{B}}T)^{-1}$

Q	heat flow into the system
W	work done on the system
S	dimensionless system entropy
F_{neq}	nonequilibrium free energy
F_{eq}	equilibrium free energy
S_{prod}	dimensionless entropy production
S_{env}	dimensionless entropy of the environment
W_{ex}	excess work $W_{\mathrm{ex}} \equiv W - \Delta F_{\mathrm{eq}}$
$\mathcal{W}(\cdot)^2$	squared L_2 Wasserstein distance
$\boldsymbol{\mu}$	mean position vector
Σ	covariance matrix
$\boldsymbol{f}$	conjugate force $\boldsymbol{f} \equiv -\partial V_{\mathrm{tot}}/\partial \boldsymbol{\lambda}$
ζ	Stokes' friction tensor
τ	integral relaxation time
$\zeta^{(2)}$	supra-Stokes' friction tensor
$\tau^{(2)}$	integral double relaxation time
$\widehat{\Delta F}$	free-energy estimator
N	number of samples
$\mathcal{C}$	integral correlation function
$D(\cdot\|\|\cdot)$	relative entropy (Kullback-Leibler divergence)
W_{save}	saved work
$R_{\lambda_{\mathrm{i}}}$	initial force relaxation rate
$P^{\mathrm{st}}_{\mathrm{save}}$	short-time power savings
G_{save}	gain in saved work
h	magnetic field

Chapter 1

Introduction

In this thesis I discuss recent progress in optimal control of stochastic thermodynamic systems. I study isothermal stochastic thermodynamics describing control by linear response, thermodynamic geometry, and optimal transport. I derive novel methods for determining minimum-dissipation protocols for fast and strong control. Additionally, I extend the thermodynamic-geometry framework to minimizing higher-order moments of the work distribution and derive higher-order corrections beyond standard linear response. These results are illustrated with model systems relevant to biophysical experiments and applications to free-energy estimation: driven barrier crossings, rotary motors, and Ising models. Portions of the introduction to this thesis have been adapted from my review article published as Ref. 1.

1.1 Relevant History of Thermodynamics

Thermodynamics as a modern science can be traced back to the 18^{th} century and the invention of the steam engine (Fig. 1.1). The Newcomen engine (1712, ~ 10 m) was designed to exploit vacuum pressure to draw water from flooded mines. Steam engines played a crucial role in the rise of the industrial revolution. By the 19^{th} century, steam engines were widely applied in mining but still remained inefficient.[2] Mindful of their inefficiency, Sadi Carnot studied the theoretical aspects and design of maximally efficient engines, published in his *Reflections on the Motive Power of Fire*.[2] This is widely considered the start of modern thermodynamics, leading to increases in engine efficiency and ultimately the development of the modern form of the first and second laws of thermodynamics by Clausius in 1850.[2] In 1877, Boltzmann began the development of statistical mechanics with the kinetic theory

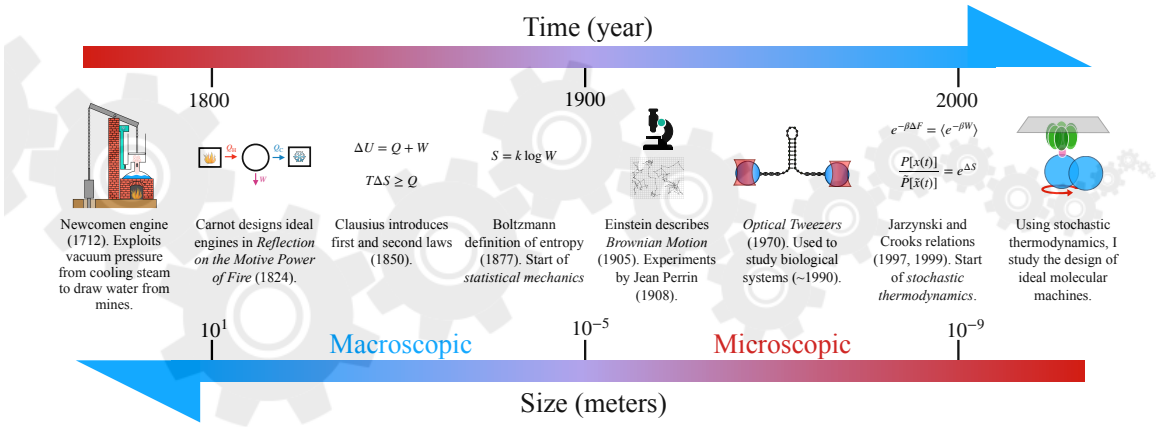

Fig 1.1. Relevant history of thermodynamics. Top: time increases from left to right, from the invention of the Newcomen engine in 1712 to the studies of molecular machines of the present day. Bottom: as time moves forward the systems that can be built or studied decreases in size from macroscopic (Newcomen engine, $\sim 10^{1}$ m), to microscopic (molecular machines, 10^{-6} m to 10^{-9} m).

of gases and a microscopically inspired definition of entropy. This led to the modern formulation of entropy and the second law,[3] placing fundamental bounds on the efficiency of thermodynamic machines. At this time the machines and motors were macroscopic, often the size of an entire building;[4] however, over time the systems of interest grew ever smaller, creating a desire for experimental and theoretical studies of microscopic systems.

Inspired by Boltzmann's work, Einstein theoretically described *Brownian motion* (1905),[5] a mathematical description of the motion of microscopic particles ($\sim 10^{-6}$ m) in a fluid. This was quickly experimentally confirmed by Jean Perrin,[6] who tracked the motion of gamboge and mastic grains under a microscope by hand on graph paper. With the discovery of optical tweezers in 1970,[7] researchers gained the ability to directly manipulate and drive microscopic systems. Additionally, optical tweezers can be used to indirectly manipulate and observe nanoscopic systems such as DNA hairpins[8–13] and molecular machines.[14–24]

Molecular machines are remarkable contraptions that harness free energy at the microscopic scale to perform useful tasks. For example, the rotary motor ATP synthase harnesses a proton gradient across the mitochondrial membrane to drive a crankshaft to synthesize ATP, an essential energy storage unit for the cell. This molecular machine has remarkable similarities to macroscopic thermodynamic machines: it transforms a thermodynamic free energy into work and heat to perform a task; however, it operates at a much smaller scale than macroscopic machines.

There are several properties unique to small-scale systems: due to their small scale they

are constantly bombarded by fluctuations which are comparable to their operational energy scale (of order $k_{\mathrm{B}}T$), and they operate on timescales comparable to their natural relaxation time implying that they are inherently out of thermodynamic equilibrium. Therefore, the macroscopic theory of thermodynamics cannot be directly applied to microscopic systems. This led to a desire for a thermodynamic theory of microscopic systems. The modern theory of the thermodynamics of small-scale systems goes under the name of *stochastic thermodynamics*, which describes the nonequilibrium energetics of fluctuating systems. Despite the apparent difficulty in describing nonequilibrium and fluctuating systems, stochastic thermodynamics has surprisingly general results such as the Crooks fluctuation theorem and the Jarzynski equality.[25,26]

Inspired by the study of maximally efficient engines at the macroscopic scale, I take a similar approach for small-scale systems. Studying efficient motors in stochastic thermodynamics leads to not only direct applications to improved experimental studies and free-energy estimates, but also improves the fundamental understanding of stochastic thermodynamic systems.

1.2 Overview of Thermodynamic Control

Historically, modern thermodynamic control began with the study of finite-time thermodynamics of macroscopic systems,[27–29] the natural extension beyond quasistatic (infinitely slow) processes. Any finite-time thermodynamic control will induce some degree of irreversibility, manifesting as energy dissipated into the environment. A goal of finite-time thermodynamics is to quantify and minimize this dissipation through the use of designed control strategies. For example, Ref. 30 studied the optimal cycle for finite-time operation of a heat engine and found that instantaneous jumps in control parameters are necessary to minimize dissipation.

In parallel, a thermodynamic-geometry framework was developed to provide a novel means to describe thermodynamic processes on a smooth (generally Riemannian) manifold.[31–33] Ref. 34 showed the connections between thermodynamic geometry and minimum-dissipation protocols, opening the door for the development of a geometric description of minimum-dissipation protocols. Although theoretically compelling, the utility of the framework was not fully realized until the development of stochastic thermodynamics.

The aforementioned descriptions focused on macroscopic systems that equilibrate rapidly and whose fluctuations are relatively small. The advent of modern experimental techniques, including single-molecule biophysical experiments, created demand for a theoretical description of the energetics of microscopic systems. To describe these small-scale systems, the field of stochastic thermodynamics was developed.[35,36] Just like its macroscopic counterpart, a

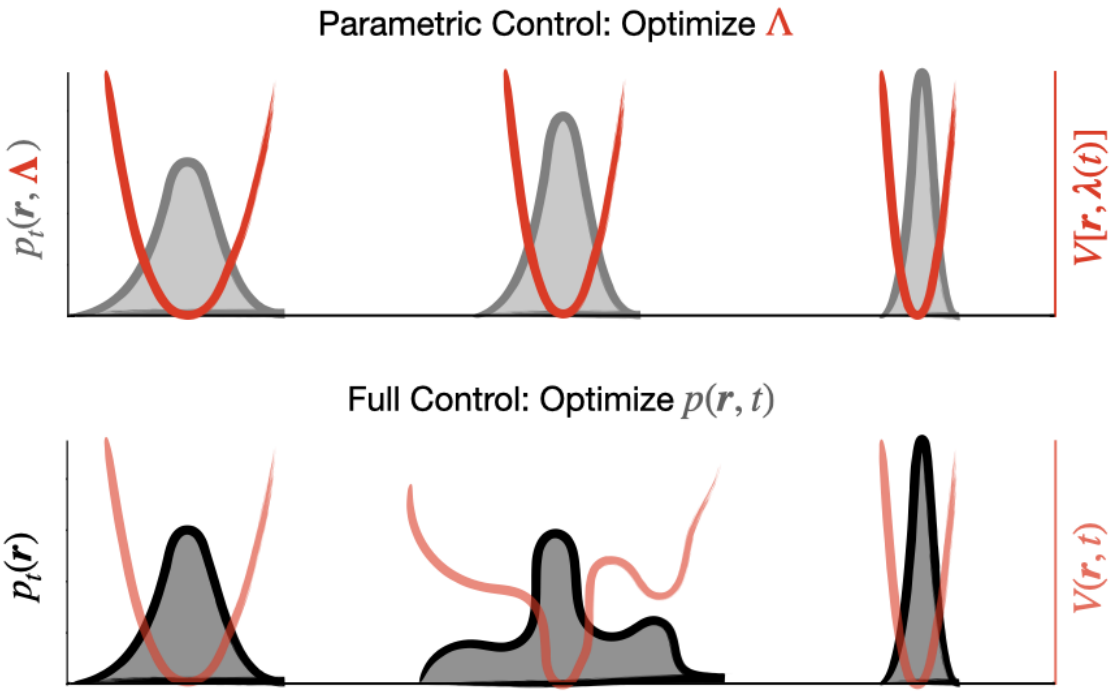

Fig 1.2. Schematic illustrating the differences between parametric control and full control. Parametric control (top) adjusts a finite number of control parameters $\boldsymbol{\lambda}(t)$ according to a protocol $\boldsymbol{\Lambda}$ between specified endpoints, thereby driving the probability distribution $p_t(\boldsymbol{r}, \boldsymbol{\Lambda})$. Full control (bottom) assumes complete control of the probability distribution $p_t(\boldsymbol{r})$ (shaded) which can be optimally driven between the endpoints by a time-dependent potential $V(\boldsymbol{r}, t)$ (red curves).

central goal of stochastic thermodynamics is the description of optimal control strategies: methods for performing a given task at minimum energetic cost.[37,38]

In this thesis I consider two distinct but related types of control: full control (section 4.1) and parametric control (section 4.2). Full control assumes complete control of the probability distribution[39] (Fig. 1.2, top). Parametric control adjusts a finite number of control parameters (Fig. 1.2, bottom) to drive the probability distribution. For a more general and detailed discussion of control theory and its applications to physics see Ref. 40.

1.2.1 Exact Solution

For either full or parametric control, the exact minimum-dissipation protocol is known if the probability distribution is Gaussian throughout the protocol.[41–43] These exact solutions provide a glimpse into the properties of optimal control processes. For example, just like the finite-time thermodynamic control described previously, the minimum-dissipation protocol has discontinuous changes in control parameters at the start and end of the protocol but remains continuous between these endpoints.[41] These discontinuities are present even for underdamped dynamics.[44] The control-parameter jumps have been observed in a number of different systems[44–46] and are now well understood and have been shown to be a general feature.[47]

1.2.2 Full Control

For more general solutions under full control, the study of minimum-dissipation protocols can be mapped onto optimal-transport theory, a well-developed branch of mathematics for which there exist numerous algorithms and methods for determining the optimal-transport map.[48,49] The connection between minimum-dissipation protocols and optimal-transport theory was first shown in Ref. 50 for overdamped dynamics: the protocol that minimizes dissipation when driving a system obeying overdamped Fokker-Planck dynamics between specified initial and final distributions is governed by the Wasserstein distance[51–54] and the Benamou-Brenier formula.[55] This technique eventually led to new fundamental lower bounds on the average work required for finite-time information erasure.[39,56] Initially only applicable to overdamped dynamics, the connections between optimal-transport theory and minimum-dissipation protocols have recently been shown for discrete-state and quantum systems.[53,57–61]

1.2.3 Parametric Control

General solutions for parametric control are typically difficult to determine, although recent progress has been made towards exact solutions for general systems building off of optimal-transport[59] or advanced numerical techniques.[45,62,63] Although exact solutions are convenient where possible, the determination of minimum-dissipation protocols can be considerably simplified through approximate methods. Inspired by a diagram presented in Ref. 64, I schematically show in Fig. 1.3 the limits where minimum-dissipation protocols are known.

Linear-response theory can be used to determine the minimum-dissipation protocol for weak perturbations and performs relatively well at any driving speed and beyond its strict

range of validity.[64,65] For slow control, the thermodynamic-geometry framework has been generalized to stochastic thermodynamic systems[33,66] and has been used to explore a diverse set of model systems,[66–79] including DNA-pulling experiments[80] and free-energy estimation.[81] In the opposite limit of fast control, minimum-dissipation protocols are described by short-time efficient protocols[47], which can be combined with the thermodynamic-geometry framework to design interpolated protocols that perform well at any driving speed.[82] Leveraging known solutions from optimal-transport theory, strong control can be described by the strong-trap approximation, yielding explicit solutions for minimum-dissipation protocols.[43]

1.2.4 Related Work

There are a number of related topics which are not covered in this thesis, such as optimal control of heat engines (including optimal cycles[78,79,83–86] and efficiency at maximum power[54,87–100]) and optimal control in quantum thermodynamics (including thermodynamic geometry[68,72,101,102] and shortcuts to adiabaticity[103–105]).

1.3 Organization

This thesis is organized as follows: I begin with examples of both experimental and theoretical model systems in chapter 2, followed by a brief introduction to stochastic thermodynamics of heat, work, and entropy production in chapter 3. Chapter 4 reviews recent progress in the optimal control of stochastic thermodynamics, including full control (section 4.1) and parametric control (section 4.2) under weak 4.2.1 or slow 4.2.2 driving. An introduction to free-energy estimation is presented in chapter 5. Chapter 6 extends the slow-control approximations to account for higher-order corrections and moments of the work distribution, chapter 7 derives a novel approximation and method for determining minimum-dissipation protocols for fast driving, and chapter 8 derives an approximation for determining minimum-dissipation protocols for strong control, filling out all the sides of the diagram in Fig. 1.3. Chapter 9 then applies all these techniques to driven barrier crossing, before chapter 10 concludes with a perspective and outlook.

Chapters 1, 2, 3, 4, and 5 are adapted from my review published as Ref. 1. Chapter 6 is adapted from Ref. 81, chapter 7 from Ref. 47, chapter 8 from Ref. 43, and chapter 9 from Ref. 82. In all cases I am the first author and performed the majority of the writing, editing, and analysis. The Ising-model calculations and analysis in chapter 7 were performed by coauthor Miranda D. Louwerse, whereas all other numerical calculations were performed by me as described in appendix A.

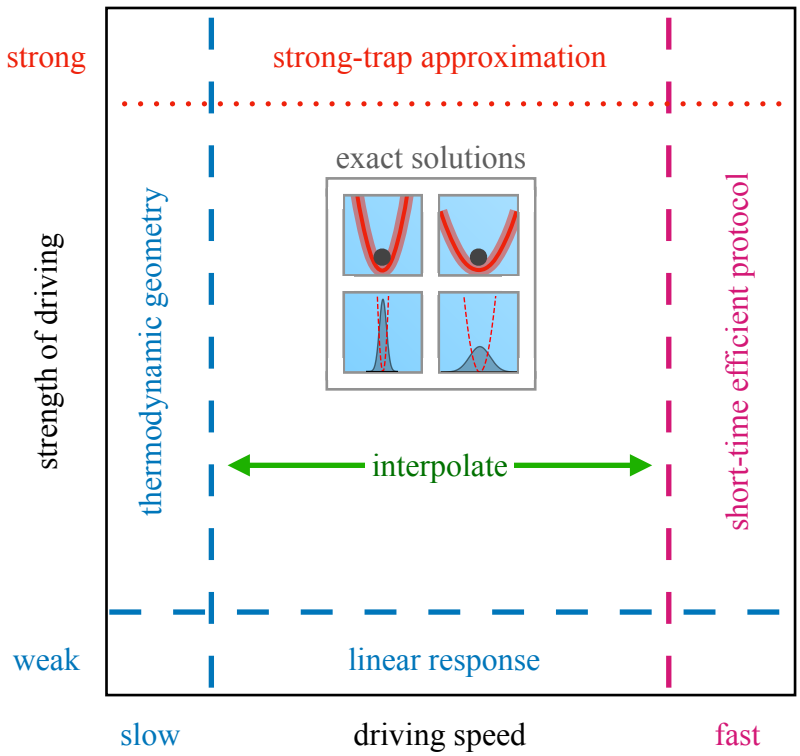

Fig 1.3. The space of thermodynamic control. The horizontal axis is the driving speed from slow to fast, and the vertical axis is the strength of driving from weak to strong. Linear-response theory is applicable to weak and slow driving (blue), and for slow driving can be simplified to a thermodynamic-geometry framework. Short-time efficient protocols are valid for fast driving (purple) and can be combined with thermodynamic geometry to bridge the space between slow and fast with interpolated protocols (green). The strong-trap approximation (red) is only valid for overdamped dynamics, with region of applicability schematically indicated by a distinct dotted line. Exact solutions for Gaussian distributions serve as a window into the properties of minimum-dissipation protocols and are valid at any driving speed or strength of driving.

Chapter 2

Model Systems

In this chapter I provide a brief introduction to paradigmatic model systems that motivate and guide the study of optimal control in stochastic thermodynamics. As discussed in chapter 1, the growth of stochastic thermodynamics coincides with the advent of new experimental techniques used to manipulate and measure single-molecule biophysical systems.[14–24] First and foremost among these techniques are laser optical tweezers[106–108] which can be used to trap microscopic Brownian systems.

2.1 Quadratic Trap

The simplest experimental apparatus for studying stochastic thermodynamics is that of a microscopic bead trapped in an optical potential. From a theoretical perspective, this system is well approximated by continuous overdamped Brownian motion in a quadratic constraining potential. In these experiments, the center and stiffness of the trapping potential can be dynamically controlled to manipulate the system. With the use of feedback control, this experimental apparatus can be augmented to realize a virtual constraining potential of any form[109–111] and can, for example, be used to study fundamental bounds on information processing through bit erasure.[112–116]

The system is driven by a quadratic trapping potential

$$V_{\text{trap}}[\boldsymbol{r}, \boldsymbol{r}_t^{\text{c}}, K_t] = \frac{1}{2}\left[\boldsymbol{r} - \boldsymbol{r}_t^{\text{c}}\right]^\top K_t \left[\boldsymbol{r} - \boldsymbol{r}_t^{\text{c}}\right] \ . \tag{2.1}$$

$\boldsymbol{r}$ is the position vector of the bead, $\boldsymbol{r}_t^{\text{c}}$ is the position of the trap center, K is the symmetric stiffness matrix, superscript $\top$ is the vector transpose, and subscript t denotes a variable at time t.

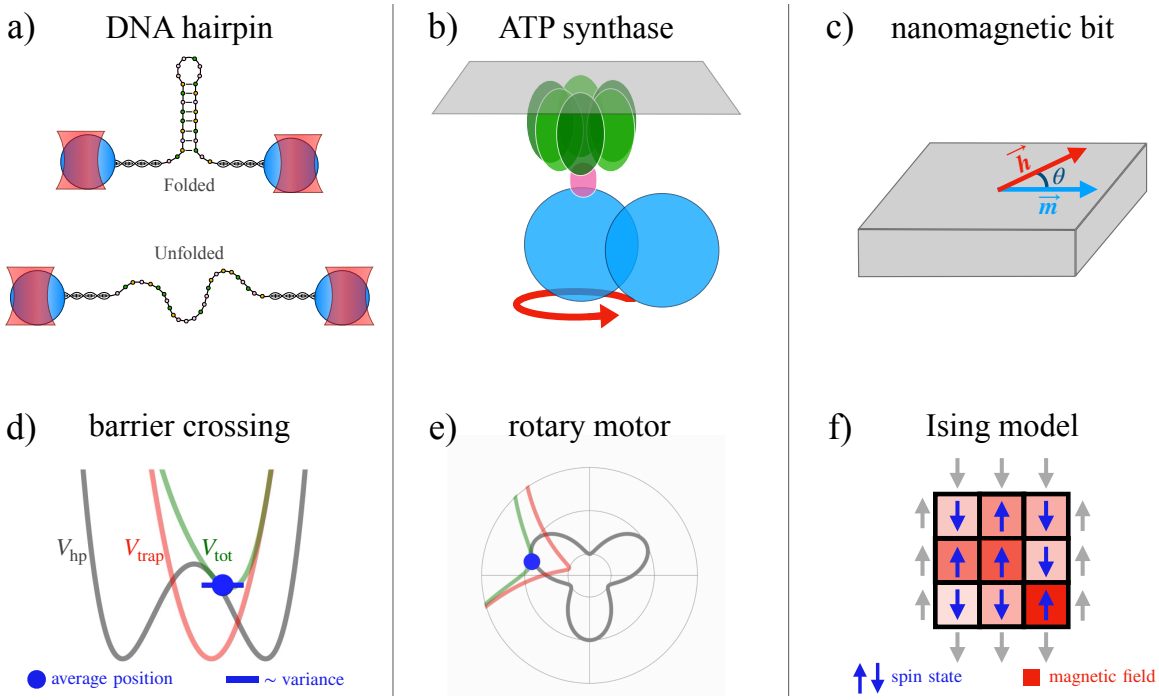

Fig 2.1. Model systems typical of stochastic thermodynamic control (top): a) DNA hairpin driven between folded and unfolded states by laser optical tweezers, b) ATP synthase driven by a magnetic trapping potential, and c) nanomagnetic bit driven by an external magnetic field. Simplified theoretical descriptions (bottom) of the model systems in the top row: d) symmetric barrier-crossing model, e) Brownian rotary motor model, and f) nine-spin Ising model with independent magnetic fields applied to each spin.

2.2 Barrier Crossing

Microscopic beads trapped by laser optical tweezers can be attached to biopolymers to probe their properties. For example, dual-trap optical tweezers can be used to fold and unfold DNA or RNA hairpins by modulating the separation between the trapping potentials (Fig. 2.1 a).[8–13] Monitoring the positions of the probe beads provides insight into the properties of the indirectly observed biopolymers. The simplest model representing this process is that of a driven barrier crossing,[117] where a Brownian system is dynamically driven over an energy barrier by a time-varying quadratic trapping potential (Fig. 2.1 d).[66,82]

The total potential $V_{\rm tot}[x, x^{\rm c}(t), k(t)] = V_{\rm land}[x] + V_{\rm trap}[x, x^{\rm c}(t), k(t)]$ is the sum of the static energy landscape $V_{\rm land}[x]$ and time-dependent trap potential $V_{\rm trap}[x, x^{\rm c}(t), k(t)]$ (shown schematically in Fig. 2.1d). For this model the static energy landscape is given by the hairpin potential $V_{\rm hp}$, which is modeled as a static double well (symmetric for simplicity) with the two minima at $x = 0$ and $x = \Delta x_{\rm m}$ respectively representing the folded and unfolded states,[12,13,66,117]

$$V_{\rm hp}(x) = E_{\rm b}\left[\left(\frac{2x - \Delta x_{\rm m}}{\Delta x_{\rm m}}\right)^2 - 1\right]^2 , \tag{2.2}$$

for position x, barrier height $E_{\rm b}$, distance $x_{\rm m}$ from the minimum to barrier, and distance $\Delta x_{\rm m} = 2x_{\rm m}$ between the minima. The system is driven by a quadratic trap (2.1) with time-dependent stiffness and center.

2.3 Rotary Motor

Magnetic traps can be used to probe the F1 component of the rotary motor ATP synthase (Fig. 2.1 b),[14–16] which is driven periodically to synthesize ATP, an essential and portable energy source for the cell. Once again, microscopic beads are used to probe the properties of the molecular machine and can be dynamically driven (Fig. 2.1 e); however, the control differs from driven barrier crossing in that the driving is periodic.

As a simple model rotary motor, consider a one-dimensional energy landscape (Fig. 2.1e),

$$V_{\rm land}(x) = \frac{E_{\rm b}}{2}\left(1 - \cos\frac{2\pi}{\Delta x_{\rm m}}x\right) + \frac{\Delta E}{\Delta x_{\rm m}}x , \tag{2.3}$$

consisting of periodic (first term) and linear (second term) contributions to the energy landscape. The barrier height is $E_{\rm b}$, the distance from peak to well is $x_{\rm m}$, the distance

between wells is $\Delta x_{\mathrm{m}} = 2x_{\mathrm{m}}$, and the machine transduces energy ΔE per barrier crossing. The system is driven by a quadratic trap (2.1) with time-dependent stiffness and center.

2.4 Nanomagnetic Bit

As a final example, consider a nanomagnetic bit characterized by its spin state or average magnetization (Fig. 2.1 c). By applying an external magnetic field, the system state can be driven from all spin-down to all spin-up, reversing the magnetization and resulting in a bit flip.[118] This type of system is typically modeled with a discrete state space, e.g., the Ising model (Fig. 2.1 f), and optimal control of this system has been investigated.[75–77] Due to the discrete state space, the properties of optimal control can differ from those for a system with a continuous state space.

Chapter 3

Dynamics and Thermodynamics

Stochastic thermodynamics as presented in this thesis uses dynamical probabilistic models of microscopic systems to determine nonequilibrium transformations of energy through work, heat, and entropy production. In relation to classical approaches to thermodynamics and nonequilibrium thermodynamics, stochastic thermodynamics focuses on microscopic fluctuating systems. These small-scale systems have relatively large fluctuations which require a stochastic treatment giving rise to unique thermodynamic properties.[35] In this chapter the dynamical equations of motion for the nonequilibrium probability distribution of the system are introduced. Definitions of thermodynamic quantities such as energy, heat, work, entropy, and free energy are given in the context of the first law of thermodynamics. The Crooks relation and Jarzynski's equality are presented and give insight into the second law of thermodynamics. Excess work and entropy production are introduced as measures of energy dissipation and their applicability to model systems is discussed. This chapter defines the mathematical framework employed for the remainder of this thesis.

3.1 Dynamics

I focus on thermodynamics at the distribution level, which is described by dynamics of the form

$$\frac{\partial p_t(\boldsymbol{r})}{\partial t} = L[\boldsymbol{r}, t]\ p_t(\boldsymbol{r})\ , \tag{3.1}$$

governing the time evolution of a nonequilibrium probability distribution $p_t(\boldsymbol{r})$ over position vector $\boldsymbol{r}$ at time t according to the time-evolution operator $L[\boldsymbol{r}, t]$. For Fokker-Planck

dynamics L is the drift/diffusion operator, and for master-equation dynamics it is the transition-rate matrix.

For either Fokker-Planck or master-equation dynamics, the solution to (3.1) can be formally expressed as

$$p_t(\boldsymbol{r}) = \mathcal{T} \exp\left\{\int_0^t \mathrm{d}t' L[\boldsymbol{r},t]\right\} p_0(\boldsymbol{r}) \ , \tag{3.2}$$

with $\mathcal{T}$ the time-ordering operator; i.e., the solution is the ordered exponential of $L[\boldsymbol{r},t]$ (expressed as a sum)

$$p_t(\boldsymbol{r}) = \sum_{n=0}^{\infty} \int_0^t \mathrm{d}t'_n \int_0^{t'_n} \mathrm{d}t'_{n-1} \cdots \int_0^{t'_2} \mathrm{d}t'_1 \ L[\boldsymbol{r},t'_n] L[\boldsymbol{r},t'_{n-1}] \cdots L[\boldsymbol{r},t'_1] \ p_0(\boldsymbol{r}) \ . \tag{3.3}$$

Although typically not exactly solvable, this formal solution gives intuition and helps guide approximations to exact solutions of (3.1).

Continuous-space stochastic systems are described by the Fokker-Planck equation, which for overdamped dynamics has the time-evolution operator

$$L[\boldsymbol{r},t] = \nabla \cdot \boldsymbol{v}(\boldsymbol{r},t) + \boldsymbol{v}(\boldsymbol{r},t) \cdot \nabla \ , \tag{3.4}$$

for mean local velocity[52]

$$\boldsymbol{v}(\boldsymbol{r},t) \equiv -D\nabla \left[\beta V_{\mathrm{tot}}(\boldsymbol{r},t) + \ln p_t(\boldsymbol{r})\right] \ , \tag{3.5}$$

total potential V_{tot}, diffusivity D, and $\beta \equiv (k_{\mathrm{B}}T)^{-1}$ for temperature T and Boltzmann's constant k_{B}. For the example of driven barrier crossing, the total potential includes both the hairpin and trapping potential, and the time dependence arises from dynamic changes in the trap center and stiffness which drive the system over the barrier.

For Fokker-Planck dynamics, Eq. (3.1) can be expressed as

$$\frac{\partial p_t(\boldsymbol{r})}{\partial t} = -\nabla \cdot \left[\boldsymbol{v}(\boldsymbol{r},t) p_t(\boldsymbol{r})\right] \ , \tag{3.6}$$

which has the formal solution[119]

$$p_t(\boldsymbol{r}) = \int \mathrm{d}\boldsymbol{r}_0 \ \delta[\boldsymbol{r} - \boldsymbol{\xi}(t|\boldsymbol{r}_0)] p_0(\boldsymbol{r}_0) \ , \tag{3.7}$$

where $\boldsymbol{\xi}(t|\boldsymbol{r}_0)$ solves the auxiliary dynamics

$$\frac{\partial \boldsymbol{\xi}(t)}{\partial t} = \boldsymbol{v}[\boldsymbol{\xi}(t|\boldsymbol{r}_0), t] \ , \tag{3.8}$$

with initial condition $\boldsymbol{\xi}(0|\boldsymbol{r}_0) = \boldsymbol{r}_0$. This formal solution nicely ties into solutions in optimal transport through the Benamou-Brenier formula[55] as discussed in chapter 4.

3.2 First Law

The first law of thermodynamics is a statement of conservation of energy: any change in energy is associated with work done on the system and heat dissipated into the environment.

The average energy of the system is

$$\langle V_{\text{tot}} \rangle = \int \mathrm{d}\boldsymbol{r}\ V_{\text{tot}}(\boldsymbol{r}, t) p_t(\boldsymbol{r}) \ , \tag{3.9}$$

with rate of change

$$\frac{\mathrm{d}\langle V_{\text{tot}} \rangle}{\mathrm{d}t} = \int \mathrm{d}\boldsymbol{r} \left[\frac{\partial V_{\text{tot}}(\boldsymbol{r}, t)}{\partial t} p_t(\boldsymbol{r}) + \frac{\partial p_t(\boldsymbol{r})}{\partial t} V_{\text{tot}}(\boldsymbol{r}, t) \right] \ . \tag{3.10}$$

The first righthand-side term quantifies the rate of change in work $\langle \dot{W} \rangle$ done on the system by an external agent controlling the potential $V_{\text{tot}}(\boldsymbol{r}, t)$ (e.g., an experimentalist dynamically driving a trapping potential), and the second quantifies the rate of change of heat $\langle \dot{Q} \rangle$ into the system from changes in the system distribution $p_t(\boldsymbol{r})$ (e.g., the system responding and relaxing towards a new equilibrium distribution in response to movement of the center and stiffness of the trapping potential):

$$\langle \dot{W} \rangle \equiv \int \mathrm{d}\boldsymbol{r}\ \frac{\partial V_{\text{tot}}(\boldsymbol{r}, t)}{\partial t} p_t(\boldsymbol{r}) \ , \tag{3.11}$$

$$\langle \dot{Q} \rangle \equiv \int \mathrm{d}\boldsymbol{r}\ \frac{\partial p_t(\boldsymbol{r})}{\partial t} V_{\text{tot}}(\boldsymbol{r}, t) \ . \tag{3.12}$$

Within this chapter a dot above a variable denotes the rate of change with respect to time of a path-dependent quantity. Substituting (3.11) and (3.12) into (3.10) and integrating over time gives the first law of thermodynamics: any change in system energy equals work and heat flows into the system

$$\langle \Delta V_{\text{tot}} \rangle = \langle W \rangle + \langle Q \rangle \ . \tag{3.13}$$

I define the nonequilibrium free energy

$$F_{\text{neq}} \equiv \langle V_{\text{tot}} \rangle - \beta^{-1} S \tag{3.14a}$$

$$= \int \mathrm{d}\boldsymbol{r}\ \left[V_{\text{tot}}(\boldsymbol{r}, t)\, p_t(\boldsymbol{r}) + \beta^{-1}\, p_t(\boldsymbol{r}) \ln p_t(\boldsymbol{r}) \right] \tag{3.14b}$$

and dimensionless entropy

$$S \equiv -\int \mathrm{d}\boldsymbol{r}\; p_t(\boldsymbol{r}) \ln p_t(\boldsymbol{r}) \;. \tag{3.15}$$

If the probabilities in (3.14a) are equilibrium distributions, then the nonequilibrium free energy reduces to the equilibrium free energy F_{eq}, and the first law (3.13) is expressed as

$$\Delta F_{\mathrm{eq}} = \langle W \rangle + \langle Q \rangle - \beta^{-1} \Delta S \tag{3.16a}$$

$$\Delta F_{\mathrm{eq}} = \langle W \rangle - \beta^{-1} \Delta S_{\mathrm{prod}} \;, \tag{3.16b}$$

for entropy production $\Delta S_{\mathrm{prod}} = \Delta S - \beta \langle Q \rangle$. Any change in equilibrium free energy is associated with work and entropy production.

3.3 Fluctuation Theorems and the Second Law

Some of the earliest and greatest achievements of stochastic thermodynamics are *fluctuation theorems*. Many fluctuation theorems can be thought of as the modern form of the second law of thermodynamics, but they contain much richer and more detailed information than the classical second law.

Foremost among them is the Crooks relation,[26,120] which constrains the probability of forward (subscript F) and reverse (subscript R) work measurements as

$$p_{\mathrm{F}}(W) e^{-\beta(W - \Delta F_{\mathrm{eq}})} = p_{\mathrm{R}}(-W) \;. \tag{3.17}$$

The reverse work measurement is taken during the reverse protocol, namely the time-reversal of the forward protocol, starting at equilibrium in the end state of the forward protocol (the distribution over microstates it would reach after equilibrating after the forward protocol completes). Although this equation appears simple, it yields profound insights about thermodynamics: it relates nonequilibrium work measurements and probabilities to the equilibrium free energy. Equation (3.17) is of practical use in free-energy estimation as discussed in chapter 5.

To gain further theoretical insight, I integrate (3.17) over W, producing Jarzynski's equality[25]

$$\left\langle e^{-\beta(W - \Delta F_{\mathrm{eq}})} \right\rangle = 1 \;, \tag{3.18}$$

from which the equilibrium free energy can be directly computed through the exponentially averaged nonequilibrium work. I have dropped any dependence on forward or reverse protocols, under the assumption that the free-energy change is measured in the same direction

as the protocol. Applying Jensen's inequality gives

$$\langle W \rangle \geq \Delta F_{\text{eq}} \ , \tag{3.19}$$

which is a statement of the second law: the average work performed on a system is always greater than or equal to the equilibrium free-energy change. Substituting the definition of the equilibrium free energy (3.14a) and the first law (3.13), the second law can be expressed as

$$\beta^{-1} \Delta S - \langle Q \rangle \geq 0 \ . \tag{3.20}$$

The Crooks relation and Jarzynski equality imply the second law of thermodynamics, but whereas the second law is an inequality, the Crooks and Jarzynski equations are equalities which hold arbitrarily far from equilibrium and contain more detailed information about the thermodynamics of the system. This detailed information will prove extremely useful for applications to free-energy estimation (chapter 5) and for uncovering novel properties of nonequilibrium work statistics (chapter 6). A detailed discussion of fluctuation theorems can be found in Refs. 35 and 36.

3.4 Work and Entropy Production

For an isothermal process the rate of change in free energy (3.14a) is

$$\frac{\mathrm{d}F_{\text{neq}}}{\mathrm{d}t} = \frac{\mathrm{d}\langle V_{\text{tot}} \rangle}{\mathrm{d}t} - \beta^{-1} \frac{\mathrm{d}S}{\mathrm{d}t} \ , \tag{3.21a}$$

$$= \langle \dot{W} \rangle + \langle \dot{Q} \rangle - \beta^{-1} \frac{\mathrm{d}S}{\mathrm{d}t} \ , \tag{3.21b}$$

$$= \langle \dot{W} \rangle - \beta^{-1} \dot{S}_{\text{prod}} \ . \tag{3.21c}$$

The dimensionless entropy production is

$$\dot{S}_{\text{prod}} \equiv \frac{\mathrm{d}S}{\mathrm{d}t} + \frac{\mathrm{d}S_{\text{env}}}{\mathrm{d}t} \tag{3.22a}$$

$$= \frac{\mathrm{d}S}{\mathrm{d}t} - \beta \langle \dot{Q} \rangle \tag{3.22b}$$

$$\geq 0 \ , \tag{3.22c}$$

for environmental entropy S_{env}. Equation (3.22a) states that the rate of entropy production is the sum of the rates of entropy production of both the system and environment. Equation (3.22b) equates the change in entropy of the environment with the heat flow into the

environment, $\mathrm{d}S_{\mathrm{env}}/\mathrm{d}t = -\beta\langle\dot{Q}\rangle$, and (3.22c) follows from the second law of thermodynamics (3.20). Importantly, this definition of entropy production only accounts for dissipation during the protocol; if the system is not in equilibrium at the end of the protocol, additional energy may be dissipated into the environment during subsequent relaxation.

A measure of energy dissipation which accounts for relaxation to equilibrium even after the protocol terminates is the excess work $W_{\mathrm{ex}} \equiv W - \Delta F_{\mathrm{eq}}$, the amount of work done in excess of the equilibrium free-energy difference. The excess work and entropy production are related by

$$\langle W_{\mathrm{ex}}\rangle = \Delta F_{\mathrm{neq}} - \Delta F_{\mathrm{eq}} + \beta^{-1}\Delta S_{\mathrm{prod}} \ , \tag{3.23}$$

for entropy production $\Delta S_{\mathrm{prod}} \equiv \int_0^{\Delta t} \mathrm{d}t\, \dot{S}_{\mathrm{prod}}$, nonequilibrium free-energy difference ΔF_{neq} between the initial $p_0(\boldsymbol{r})$ and final $p_{\Delta t}(\boldsymbol{r})$ distributions, and equilibrium free-energy difference ΔF_{eq} between the initial and final equilibrium distributions.

Equation (3.23) clarifies the distinction between entropy production and excess work: if both the initial and final states of the system are at equilibrium, the two quantities are equal, otherwise the difference between the two equals the difference between the nonequilibrium and equilibrium free-energy changes. If the system is allowed to relax to equilibrium, then this excess energy is dissipated into the environment, resulting in additional entropy production not accounted for in the present definition (3.22a), so that the total entropy production for such a process is (3.22a) plus the entropy production from the subsequent relaxation. In contrast, the excess work always includes the energy dissipated into the environment from the system relaxing towards equilibrium after the protocol terminates. Quantifying dissipation by the entropy production in (3.22a) assumes one can harness the nonequilibrium free energy at the conclusion of the protocol to perform a useful task (generally true for periodically driven systems like ATP synthase), while excess work quantifies dissipation when all the excess free energy is dissipated into the environment after the protocol terminates (generally true for two-state barrier crossings like hairpin experiments).

Optimal control in thermodynamics is often discussed in terms of minimizing either entropy production or excess work incurred during the protocol. Since periodically driven systems (e.g., ATP synthase) do not have the opportunity to relax to equilibrium, their dissipation is quantified by entropy production (3.22a). Additionally, for full control the final distribution can be constrained and dissipation is also determined by the entropy production (section 4.1). Excess work is used for parametric control (section 4.2) which is relevant to model systems such as DNA hairpins and nanomagnetic bits which are driven between control-parameter endpoints rather than periodically. Systems driven between control-parameter endpoints are allowed to equilibrate after each driving protocol, so excess work is the relevant measure of dissipation.

Chapter 4

Optimal Control

In this chapter I provide an introduction to optimal control in stochastic thermodynamics, from full to parametric control. Full control assumes complete control over the probability distribution, which is leveraged to determine minimum-dissipation protocols based on optimal transport theory. The exact solution for the minimum-dissipation protocols is known for one-dimensional and Gaussian systems. For parametric control, a finite number of control parameters are dynamically varied to drive a system between specified initial and final control-parameter values. Using linear-response theory, approximate solutions can be determined for weak and slow control. The results discussed in this chapter form the background which will be built upon in Chapters 6-8.

4.1 Full Control

Assuming full control over the probability distribution $p_t(\boldsymbol{r})$ (e.g., from complete control over the shape of the potential $V_{\rm tot}(\boldsymbol{r},t)$ for one-dimensional continuous-state systems) considerably simplifies the optimization process by making connections with known results from optimal-transport theory.[50,52,121] Optimal transport originally described the most efficient methods to move mass (e.g., a pile of sand) from one location to another; this is useful for describing methods that minimize dissipation in transporting probability from an initial to a final distribution.[48]

Since the final distribution is constrained, the energy dissipated into the environment throughout the protocol is determined by the average entropy produced in driving from

initial probability distribution $p_0(\boldsymbol{r})$ to final probability distribution $p_{\Delta t}(\boldsymbol{r})$ as[52]

$$\Delta S_{\text{prod}} = \frac{1}{D}\int_0^{\Delta t} \mathrm{d}t\ \langle \boldsymbol{v}(\boldsymbol{r},t)\cdot\boldsymbol{v}(\boldsymbol{r},t)\rangle\ . \tag{4.1}$$

Angle brackets $\langle\cdots\rangle$ denote an average over $p_t(\boldsymbol{r})$.

Expressing the entropy production in this form makes precise the connections between optimal-transport and minimum-dissipation protocols. In optimal transport a common measure of the distance between two distributions is the squared L_2-Wasserstein distance, defined in the Benamou and Brenier dual representation as[55]

$$\mathcal{W}(p_0,p_{\Delta t})^2 \equiv \min_v \Delta t\int_0^{\Delta t} \mathrm{d}t\ \langle \boldsymbol{v}(\boldsymbol{r},t)\cdot\boldsymbol{v}(\boldsymbol{r},t)\rangle\ . \tag{4.2}$$

Therefore, the entropy production is bounded by the squared L_2-Wasserstein distance between initial (p_0) and final ($p_{\Delta t}$) probability distributions:[52]

$$\Delta S_{\text{prod}} \geq \frac{\mathcal{W}\left(p_0,p_{\Delta t}\right)^2}{D\Delta t}\ . \tag{4.3}$$

Existing procedures from optimal transport can therefore be used to determine protocols that minimize entropy production.[48,49] Notably, the exact solution is known in two situations: one-dimensional systems and Gaussian probability distributions (section 4.1.1).

Extending minimum-dissipation full control and the connections to optimal-transport theory to more general forms of dynamics (e.g., discrete state spaces) is a rapidly advancing area of active research.[53,57–61]

4.1.1 Exact solutions

For a one-dimensional system $\boldsymbol{r} = x$, the entropy production (4.1) of the optimal-transport process can be simplified considerably as[39,50,51,56,84,122]

$$\Delta S_{\text{prod}} \geq \frac{1}{D\Delta t}\int_0^1 \mathrm{d}y\,[\mathcal{Q}_{\text{f}}(y)-\mathcal{Q}_{\text{i}}(y)]^2\ , \tag{4.4}$$

where $\mathcal{Q}_{\text{f}}$ and $\mathcal{Q}_{\text{i}}$ are respectively the final and initial quantile functions (inverse cumulative distribution functions).[82] The entropy production is minimized if the quantiles are driven so as to change linearly in time between their fixed initial and final values;[39,51,56,84] from this the time-dependent probability distribution can be computed, and then the Fokker-Planck equation inverted to determine the potential $V_{\text{tot}}(x,t)$ to be applied to achieve the control

that minimizes the entropy production:

$$V_{\rm tot}(x,t) = -\beta^{-1}\ln p_t(x) + (\beta D)^{-1}\int_{\infty}^{x} \mathrm{d}x'\ \frac{1}{p_t(x')}\int_{-\infty}^{x'} \mathrm{d}x''\ \frac{\partial p_t(x'')}{\partial t}\ . \tag{4.5}$$

Although this calculation is often analytically intractable, it is straightforward to compute numerically for any time-dependent probability distribution.

If the initial and final distributions are Gaussian, $p_t(\boldsymbol{r}) = \mathcal{N}(\mu_t, \Sigma_t)$ for time-dependent mean μ_t and covariance Σ_t, the entropy-production bound (4.3) is[42,123,124]

$$\Delta S_{\rm prod} \geq \frac{1}{D\Delta t}\left\{\Delta\boldsymbol{\mu}^2 + \mathrm{Tr}\left[\Sigma_0 + \Sigma_{\Delta t} - 2(\Sigma_{\Delta t}^{\frac{1}{2}}\Sigma_0\Sigma_{\Delta t}^{\frac{1}{2}})^{\frac{1}{2}}\right]\right\}, \tag{4.6}$$

with subscripts 0, t, and Δt respectively denoting the initial, time-dependent, and final values of the corresponding variable. Equality is achieved and the entropy production is minimized when following the optimal-transport map between the initial and final distributions, which for Gaussian distributions is completely specified by the mean and covariance:

$$\boldsymbol{\mu}_t = \boldsymbol{\mu}_0 + \frac{\Delta\boldsymbol{\mu}}{\Delta t}\ t \tag{4.7a}$$

$$\Sigma_t = \left[\left(1 - \frac{t}{\Delta t}\right)I + \frac{t}{\Delta t}C\right]\Sigma_0\left[\left(1 - \frac{t}{\Delta t}\right)I + \frac{t}{\Delta t}C\right]\ . \tag{4.7b}$$

Here $\Delta\boldsymbol{\mu} \equiv \boldsymbol{\mu}_{\Delta t} - \boldsymbol{\mu}_0$ is the total change in mean position, I is the identity matrix, and $C \equiv \Sigma_{\Delta t}^{\frac{1}{2}}(\Sigma_{\Delta t}^{\frac{1}{2}}\Sigma_0\Sigma_{\Delta t}^{\frac{1}{2}})^{-\frac{1}{2}}\Sigma_{\Delta t}^{\frac{1}{2}}$ reduces in one dimension to the ratio of final and initial standard deviations. If the covariance matrix Σ is diagonal, then (4.7b) implies

$$\Sigma_t^{\frac{1}{2}} = \Sigma_0^{\frac{1}{2}} + \frac{\Delta\Sigma^{\frac{1}{2}}}{\Delta t}\ t\ , \tag{4.8}$$

with $\Delta\Sigma^{\frac{1}{2}} \equiv \Sigma_{\Delta t}^{\frac{1}{2}} - \Sigma_0^{\frac{1}{2}}$. Thus for diagonal covariance the optimal-transport process linearly drives the standard deviation between its endpoint values. For a detailed description of minimum-dissipation protocols for general multidimensional Gaussian distributions see Ref. 42.

In both analytically solvable cases (one dimension and Gaussian) the general design principle is that the minimum-dissipation protocol linearly drives the quantiles between specified initial and final values. Linearly driving the quantiles of the probability distribution can be used as a guiding principle for designing more general minimum-dissipation protocols and arises independently for parametric control.[82]

4.2 Parametric Control

While full-control solutions are convenient when possible, many applications do not permit sufficient control to fully constrain the probability distribution throughout the entire protocol. In such cases the controller is constrained by a finite set of control parameters $\boldsymbol{\lambda}(t)$ which can be used to drive the system. Since there are insufficient control parameters to fully control the probability distribution, the endpoints of the protocol are constrained by the control-parameter values rather than the distribution. Therefore, I focus on optimizing the excess work, which is an accurate measure of dissipation provided the system equilibrates after the protocol terminates.

In this section I assume the control is the result of time-dependent control parameters $\boldsymbol{\lambda}(t)$, in which case the excess work (3.11) is

$$\langle W_{\text{ex}} \rangle_\Lambda = -\int_0^{\Delta t} \mathrm{d}t \; \langle \delta \mathbf{f}^\top(t) \rangle_\Lambda \dot{\boldsymbol{\lambda}}(t) \;, \tag{4.9}$$

where I have defined the conjugate force $\mathbf{f} \equiv -\partial V_{\text{tot}}/\partial \boldsymbol{\lambda}$ to express the work explicitly in terms of the control parameters, and δ denotes a difference from the equilibrium average. For parametric control, I denote a nonequilibrium average (dependent on the entire protocol history) as $\langle \cdot \rangle_\Lambda$ and an equilibrium average (at the current control parameter value $\boldsymbol{\lambda}(t)$) as $\langle \cdot \rangle_{\boldsymbol{\lambda}(t)}$. Since the control-parameter protocol is externally specified, the only unknown is $\langle \delta \mathbf{f}^\top(t) \rangle_\Lambda$. This quantity is particularly difficult to deal with since the nonequilibrium average depends on the entire protocol history.

For example, Ref. 41 showed that—even in one dimension—optimization requires solving the nonlocal Euler-Lagrange equation. Therefore, there are very few cases where the minimum-work protocol can be determined analytically. Promising approaches for obtaining general solutions include optimal-transport theory with limited control[59] and advanced numerical techniques.[45,62,63]

The minimum-work protocol can be determined exactly for a Brownian particle in a harmonic trap, where the optimal protocol, originally derived in one dimension[41], is identical to the full-control solution for Gaussian distributions described in section 4.1. This exact solution serves as a window into the properties of minimum-dissipation protocols and gives considerable insight into what to heuristically expect from optimized protocols: e.g., the minimum-dissipation protocols have control-parameter jumps at the start and end but remain continuous in between.

Although exact solutions are nice when possible, since general solutions are intractable I turn to approximate methods to gain insight into the general properties of minimum-dissipation protocols. The first approximation to consider is linear response, which is valid for weak or slow perturbations, and in the slow limit simplifies to a geometric framework

for determining minimum-dissipation protocols from a Riemannian metric.

4.2.1 Weak Control

Linear-response theory can be used to determine the minimum-dissipation protocol for weak perturbations and performs relatively well at any driving speed, well beyond its strict range of validity.[64,65] For fast driving, the minimum-dissipation protocols determined from linear-response theory have jumps at the start and end of the protocol.

As mentioned in section 4.2, the central quantity that needs to be determined to perform any optimization of the excess work is the nonequilibrium average force. In linear response, the deviation of the nonequilibrium average force from equilibrium is approximated by the integrated equilibrium force covariance

$$\langle \delta f_j(t) \rangle_\Lambda \approx - \int_0^t \mathrm{d}t' \; \langle \delta f_j(t-t') \; \delta f_\ell(0) \rangle_{\lambda(t)} \; \dot{\lambda}_\ell(t') \; . \tag{4.10}$$

Throughout the remainder of this thesis I use the Einstein summation convention of implied summation over all repeated indices; e.g., $A_j B_j$ represents $\sum_j A_j B_j$. The linear-response approximation greatly simplifies the optimization procedure, since the equilibrium average depends only on the current control-parameter value and not on the entire history of control. Substituting this into the excess work (4.9) gives

$$\langle W_{\mathrm{ex}} \rangle_\Lambda \;\approx\; \int_0^{\Delta t} \mathrm{d}t \int_0^t \mathrm{d}t' \;\; \dot{\lambda}_j(t) \; \langle \delta f_j(t-t') \; \delta f_\ell(0) \rangle_{\lambda(t)} \; \dot{\lambda}_\ell(t') \; , \tag{4.11}$$

which can be optimized directly by numerical methods and can perform well at any driving speed.[64,65]

4.2.2 Slow Control

The next approximation to consider is valid for slow near-equilibrium processes. This approach generalizes the paradigm of thermodynamic geometry to stochastic thermodynamics.[33,125] The generalized friction tensor endows the space of thermodynamic states with a Riemannian metric where minimum-dissipation protocols correspond to geodesics of the friction tensor. This method is widely applicable, yields a relatively simple prescription for determining minimum-dissipation protocols, and has been extended to more general settings and different forms of control.[73,126–128] The protocols determined from this method are continuous; however, it is known from exact solutions that minimum-dissipation protocols can have jump discontinuities,[41] which are never optimal within the geometric framework of

slow control. This arises from the slow near-equilibrium approximation used; indeed, in the limit of a slow protocol the jumps in the exact optimal protocol become negligible.

In addition to the linear-response approximation, I assume the control parameters are driven slowly compared to the system's natural relaxation timescale, so the approximation for the nonequilibrium average force (4.10) simplifies to

$$\langle \delta f_j(t) \rangle_\Lambda \approx -\dot{\lambda}_\ell(t) \int_0^\infty \mathrm{d}t' \, \langle \delta f_j(t') \, \delta f_\ell(0) \rangle_{\lambda(t)} \, . \tag{4.12}$$

Substituting into (4.9) yields the leading-order contribution to the excess work:[125]

$$\langle W_{\mathrm{ex}} \rangle_\Lambda \approx \int_0^{\Delta t} \mathrm{d}t \, \frac{\mathrm{d}\boldsymbol{\lambda}^\top}{\mathrm{d}t} \, \zeta[\boldsymbol{\lambda}(t)] \, \frac{\mathrm{d}\boldsymbol{\lambda}}{\mathrm{d}t} \, , \tag{4.13}$$

in terms of the generalized friction tensor with elements

$$\zeta_{j\ell}(\lambda) \equiv \beta \int_0^\infty \mathrm{d}t \, \langle \delta f_j(t) \delta f_\ell(0) \rangle_{\boldsymbol{\lambda}} \, . \tag{4.14}$$

In analogy with fluid dynamics, this rank-two tensor is the *Stokes' friction*, since it produces a drag force that depends linearly on velocity.

$\zeta_{j\ell}$ is the Hadamard product $\beta \langle \delta f_j \delta f_\ell \rangle_{\boldsymbol{\lambda}} \circ \tau_{j\ell}$ of the conjugate-force covariance (the force fluctuations) and the integral relaxation time

$$\tau_{j\ell} \equiv \int_0^\infty \mathrm{d}t \, \frac{\langle \delta f_j(t) \delta f_\ell(0) \rangle_{\boldsymbol{\lambda}}}{\langle \delta f_j \delta f_\ell \rangle_{\boldsymbol{\lambda}}} \, , \tag{4.15}$$

the characteristic time for these fluctuations to die out.

For overdamped dynamics, the friction can be calculated directly from the total energy as[71]

$$\zeta_{j\ell}(\boldsymbol{\lambda}) = \int_{-\infty}^\infty \mathrm{d}x \, \frac{\partial_{\lambda_j} \Pi_{\mathrm{eq}}(x, \boldsymbol{\lambda}) \partial_{\lambda_\ell} \Pi_{\mathrm{eq}}(x, \boldsymbol{\lambda})}{\pi_{\mathrm{eq}}(x, \boldsymbol{\lambda})} \, , \tag{4.16}$$

where $\Pi_{\mathrm{eq}}(x, \boldsymbol{\lambda}) \equiv \int_{-\infty}^x \mathrm{d}x' \pi_{\mathrm{eq}}(x', \boldsymbol{\lambda})$ is the equilibrium cumulative distribution function, ∂_{λ_j} is the partial derivative with respect to λ_j, and $\pi_{\mathrm{eq}}(x', \boldsymbol{\lambda}) = \exp[-\beta V_{\mathrm{tot}}(x, \boldsymbol{\lambda})] \; / \; \int \mathrm{d}x \exp[-\beta V_{\mathrm{tot}}(x, \boldsymbol{\lambda})]$ is the equilibrium probability distribution.

Within the slow-protocol approximation, the excess work is minimized by a protocol with constant excess power.[125] This is due to the geometric structure of (4.13), the friction acts as a Riemannian metric so protocols that minimize the excess work are those with constant excess power just as paths that minimize the arc length in a Riemannian metric

(geodesics) have constant speed. For a single control parameter, this amounts to proceeding with velocity $\mathrm{d}\lambda^{\mathrm{LR}}/\mathrm{d}t \propto \zeta(\lambda)^{-1/2}$, which when normalized to complete the protocol in a fixed allotted time Δt gives

$$\frac{\mathrm{d}\lambda^{\mathrm{LR}}}{\mathrm{d}t} = \frac{\int_{\lambda_\mathrm{i}}^{\lambda_\mathrm{f}} \mathrm{d}\lambda' \, \sqrt{\zeta(\lambda')}}{\Delta t \sqrt{\zeta(\lambda)}} \, . \tag{4.17}$$

For multi-parameter control, the minimum-dissipation protocol solves the Euler-Lagrange equation

$$\zeta_{j\ell} \frac{\mathrm{d}^2\lambda_\ell}{\mathrm{d}t^2} + \frac{\partial \zeta_{j\ell}}{\partial \lambda_m} \frac{\mathrm{d}\lambda_\ell}{\mathrm{d}t} \frac{\mathrm{d}\lambda_m}{\mathrm{d}t} = \frac{1}{2} \frac{\partial \zeta_{\ell m}}{\partial \lambda_j} \frac{\mathrm{d}\lambda_\ell}{\mathrm{d}t} \frac{\mathrm{d}\lambda_m}{\mathrm{d}t} \, . \tag{4.18}$$

This can be solved to determine geodesics that minimize excess work within the slow control approximation, as demonstrated in chapter 9.

A useful quantity for gauging the performance of designed protocols is the ratio of naive (constant velocity protocol) to designed excess work. For one-parameter control in the slow-control approximation this ratio is given by

$$\frac{\langle W_{\mathrm{ex}} \rangle_{\mathrm{naive}}}{\langle W_{\mathrm{ex}} \rangle_{\mathrm{des}}} \approx \frac{\Delta\lambda \int_{\lambda_\mathrm{i}}^{\lambda_\mathrm{f}} \mathrm{d}\lambda \, \zeta(\lambda)}{\left[\int_{\lambda_\mathrm{i}}^{\lambda_\mathrm{f}} \mathrm{d}\lambda \, \sqrt{\zeta(\lambda)}\right]^2} \, . \tag{4.19}$$

For a friction coefficient that is independent of the control parameter, i.e., a flat friction landscape, the naive and designed protocols are equivalent and this ratio is equal to one. For control parameter dependent friction the designed protocol will outperform the naive and the ratio will be larger than one.

Extensions to the slow-control approximation

The slow-control approximation has been generalized and extended to transitions between nonequilibrium steady states,[126,127] discrete control,[73] and stochastic control.[128]

Section 4.2 assumed that the system starts in equilibrium; however, this is not always the case in applications. Periodically driven machines such as ATP synthase are often driven for a sufficiently long time as to reach a nonequilibrium steady state, breaking the initial-equilibrium and near-equilibrium assumptions. Such systems may need to transition between steady states in order to increase or decrease their output in response to variable conditions (e.g., increasing/decreasing rate of ATP production). Although determining the correct definition of dissipation is more subtle for nonequilibrium steady states (see Refs. 129–136 for detailed discussion), the slow-protocol approximation has been generalized to slow transitions between nonequilibrium steady states making use of a near-steady-state ap-

proximation.[126,127] This approximation has an analogous form to the friction-tensor approximation and can be used to determine minimum-dissipation protocols for slow transitions between nonequilibrium steady states.

So far it has been assumed that the protocol is continuous; however, many biological and chemical systems convert free energy stored in nonequilibrium chemical-potential differences into useful work through a series of reactions involving binding/unbinding or catalysis of small molecules. These chemical reactions typically occur on timescales much faster than the protein conformational rearrangements they couple to. Therefore, these changes are effectively instantaneous, leading to discrete control protocols. Building off of quasistatic results,[137] it has been shown that the linear-response approximation can be applied to discretely driven systems to yield an approximation analogous to the friction tensor, which can be used to determine minimum-dissipation protocols.[73]

Chapter 5

Free-Energy Estimation

Computational and experimental measurements of free-energy differences are essential to the determination of stable equilibrium phases of matter, relative reaction rates, and binding affinities of chemical species,[138] and the identification and design of novel protein-binding ligands for drug discovery.[139–142] Current methods for determining free-energy differences rely on costly experimentation, which can be reduced through screening with efficient computational techniques.[138–145] It has been shown that the precision and accuracy of standard free-energy estimators are reduced when estimated from a protocol inducing large dissipation,[81,146,147] and that thermodynamic geometry can be applied to improve free-energy estimates.[81,147–151]

Free-energy differences are often estimated by measuring the work incurred during a parametric control protocol that drives the system between control-parameter endpoints corresponding to target states. Unidirectional estimators determine the free-energy difference from the work done by a forward protocol driving from initial to final control-parameter values, while bidirectional (forward and reverse) estimators additionally use reverse protocols that drive from final to initial control-parameter values. The simplest estimator is the mean-work estimator,[146]

$$\widehat{\Delta F}_{\mathrm{MW}} = \frac{1}{N}\sum_{j=1}^{N} W^{(j)}, \tag{5.1}$$

which estimates the free-energy difference by the average work and for any non-quasistatic (finite-speed) protocol yields a biased estimate. For an unbiased estimate, the Jarzynski

estimator (derived from the Jarzynski equality[25])

$$\widehat{\Delta F}_{\mathrm{Jar}} = -\frac{1}{\beta} \ln \frac{1}{N} \sum_{j=1}^{N} e^{-\beta W^{(j)}} \ , \tag{5.2}$$

estimates the free-energy difference from the exponentially averaged work. The mean-work and Jarzynski estimators can be used as either uni- or bidirectional estimators; however, if bidirectional data is available the maximum log-likelihood estimator is Bennett's acceptance ratio (BAR)[152]

$$\sum_{j=1}^{N_{\mathrm{F}}} \left\{ 1 + \exp\left[\beta \left(W^{(j)} - \widehat{\Delta F}_{\mathrm{BAR}} \right) \right] \right\}^{-1} = \sum_{\ell=1}^{N_{\mathrm{R}}} \left\{ 1 + \exp\left[-\beta \left(W^{(\ell)} - \widehat{\Delta F}_{\mathrm{BAR}} \right) \right] \right\}^{-1} \ , \tag{5.3}$$

with $W^{(j)}$ the jth measurement of work from driving the system, N the total number of samples, and in (5.3) I have assumed an equal number of samples in the forward N_{F} and reverse N_{R} directions with $N = N_{\mathrm{F}} + N_{\mathrm{R}}$. Equation (5.3) must be solved numerically for $\widehat{\Delta F}_{\mathrm{BAR}}$. For a large number of samples, Bennett's acceptance ratio yields the minimum variance of any unbiased estimator.[153,154]

There have been a number of hints towards connections between the amount of excess work (work done above and beyond the free-energy difference) and error in both equilibrium and nonequilibrium estimates of free-energy differences. Most obviously, the bias in thermodynamic integration is exactly the excess work; however, the connection is deeper than that. Near equilibrium it can be shown that both the bias and variance of the mean-work, and Jarzynski estimators increase with increased dissipation. For the Jarzynski estimator, the number of trajectories necessary to obtain a given level of accuracy increases exponentially with the amount of excess work.[146] The bias from excess work can be alleviated somewhat through the use of a bidirectional estimator, the bias in BAR instead depends on the difference between forward and reverse excess works.[155]

Ref. 153 has shown that, in the limit of a large number of samples, the minimum variance of any asymptotically unbiased estimator $\widehat{\Delta F}$ is,

$$\left\langle \left(\widehat{\Delta F} - \left\langle \widehat{\Delta F} \right\rangle \right)^2 \right\rangle \geq \frac{1}{N} \left\{ 2 \langle [1 + \cosh(W - \Delta F)]^{-1} \rangle^{-1} - 4 \right\} \ , \tag{5.4}$$

where for simplicity I have once again assumed an equal number of samples in the forward N_{F} and reverse N_{R} directions, and the average $\langle \cdots \rangle$ is over a total of $N = N_{\mathrm{F}} + N_{\mathrm{R}}$ work measurements. This form demonstrates an explicit connection between the minimum variance of a free-energy estimator and the excess work $W_{\mathrm{ex}} \equiv W - \Delta F$. Evidently the variance is minimized at 0 when $W_{\mathrm{ex}} = 0$, in which case only a single measurement would be required. For any finite-time protocol the excess work will in general be non-zero. How

large it is will significantly effect the scaling of the variance with excess work.

There is currently no simple bound on the bias of free-energy estimates; however, Ref. 156 provides a detailed comparison of the biases from the mean-work, Jarzynski, and BAR estimators.

There many reviews discussing best practices for both equilibrium and nonequilibrium free-energy estimates; e.g., Ref. 144 gives a review specific to drug discovery while Refs. 157,158 give more general reviews. Best practices specifically for nonequilibrium free-energy estimations are described in Ref. 145. In order to obtain accurate error estimates, the amount of excess work must be small ($\sim 1-2k_{\mathrm{B}}T$) and BAR should be used when possible. In the following sections I explore in more detail the connection between excess work, bias, and variance for both unidirectional and bidirectional free-energy estimators.

5.1 Small Dissipation

To leading order when dissipation is small ($\beta W_{\mathrm{ex}} \ll 1$), or only a single sample is taken ($N = 1$), the estimators are all equivalent to the mean-work estimator, which for unidirectional estimates has bias and variance

$$\left\langle \widehat{\Delta F} \right\rangle - \Delta F_{\mathrm{eq}} \approx \frac{1}{N} \langle W_{\mathrm{ex}} \rangle \tag{5.5a}$$

$$\left\langle \left(\widehat{\Delta F} - \left\langle \widehat{\Delta F} \right\rangle \right)^2 \right\rangle \approx \frac{2}{\beta N} \langle W_{\mathrm{ex}} \rangle \ . \tag{5.5b}$$

For bidirectional estimates in the forward (subscript F) and reverse (subscript R) directions, the bias and variance can similarly be approximated by

$$\left\langle \widehat{\Delta F} \right\rangle - \Delta F_{\mathrm{eq}} \approx \frac{1}{N} \left(\langle W_{\mathrm{ex}} \rangle_{\mathrm{F}} - \langle W_{\mathrm{ex}} \rangle_{\mathrm{R}} \right) \tag{5.6a}$$

$$\left\langle \left(\widehat{\Delta F} - \left\langle \widehat{\Delta F} \right\rangle \right)^2 \right\rangle \approx \frac{2}{\beta N} \left(\langle W_{\mathrm{ex}} \rangle_{\mathrm{F}} + \langle W_{\mathrm{ex}} \rangle_{\mathrm{R}} \right) \ . \tag{5.6b}$$

The bias of a bidirectional estimate depends on the difference of dissipation between the forward and reverse directions; i.e., a process with equal dissipation from forward and reverse protocols is unbiased even for finite samples. Furthermore, (5.6b) is the leading-order correction to (5.4) for small dissipation, and therefore also serves as an estimate of the minimum variance possible.

To demonstrate the variance of BAR and the validity of (5.4) and (5.5b), Fig. 5.1 shows the variance of BAR from Gaussian work measurements as a function of dissipation for variable N. When there is only a single sample in each forward and reverse direction ($N =$

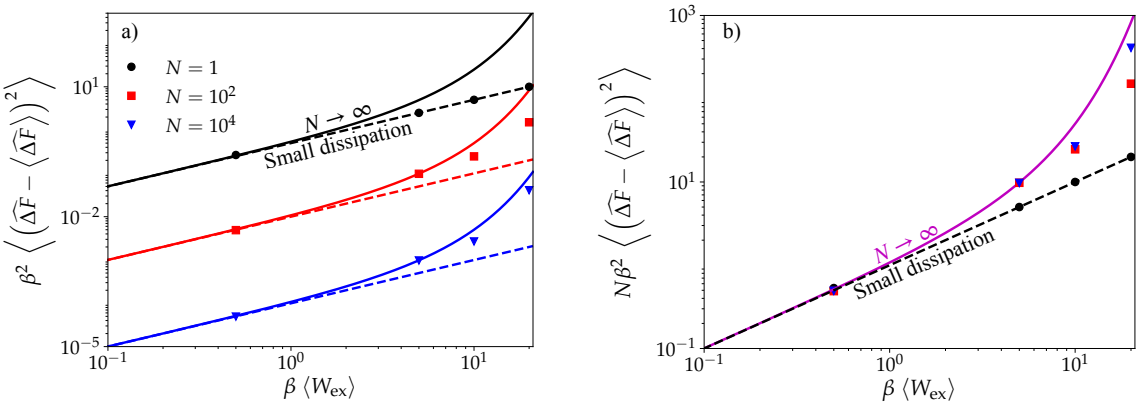

Fig 5.1. Variance of Bennett's acceptance ratio from a Gaussian work distribution. Large-N estimate of the variance (5.4) (solid) and approximation (5.5b) (dashed). The variance is shown in (a) and N times the variance in (b) for $N = 1, 10^2$, and 10^4 (black circles, red squares, and blue triangles, respectively). Calculations assume a Gaussian distribution with mean $\langle W_{ex} \rangle$ and variance $2\beta^{-1}\langle W_{ex} \rangle$. Bootstrap-resampled 95% confidence intervals are smaller than the data points.

2), the approximation of (5.5b) is exact. For more samples, (5.5b) is a good approximation when dissipation is small. As the number of samples becomes very large, the variance of BAR approaches (5.4) from below. Since for finite N BAR has lower variance than the large N bound, it may be best used as a large-N estimate of the variance rather than as a lower bound. For a Gaussian work distribution, the bias of BAR is exactly zero, even for a finite number of samples, since the distribution is symmetric about $W = \Delta F$.

Chapter 6

Skewed Thermodynamic Geometry

Free-energy differences determine the equilibrium phases of thermodynamic systems as well as the relative reaction rates and binding affinities of chemical species.[138] Computational and experimental techniques which accurately and precisely predict free-energy differences are therefore highly desirable. One important application is in pharmaceutical drug discovery, where computation of free-energy differences can aid in the identification and design of ligands for targeted protein binding.[139–142]

Regardless of the estimator, non-quasistatic control-parameter protocols result in excess work (work in excess of the free-energy difference), which increases the bias and variance (decreases the accuracy and precision, respectively) of free-energy estimates. This excess work (equaling the dissipation), and hence the error, can be reduced by following a different path through control-parameter space and varying the velocity along the path while keeping the protocol duration fixed.[159–161] Near equilibrium, this can be mapped onto the thermodynamic-geometry framework: for the mean-work estimator, the bias and variance from finite-time protocols is improved by following geodesics of a thermodynamic metric, the *force-variance* (FV) metric, a Riemannian metric defined by the covariance matrix of conjugate-force fluctuations;[31,33,34,162,163] similarly, for Bennett's acceptance ratio (BAR), the variance (but not the bias) is minimized if the protocol follows geodesics of the FV metric.[147] This has been used to improve the precision of calculated binding potentials of mean force.[148–151]

The FV metric only minimizes the variance of the mean-work estimator and BAR if the relaxation time is independent of the control parameters. The *friction-tensor* metric,[68,125] the product of the covariance and integral relaxation time of conjugate-force fluctuations (6.19), is more general than the FV and provides a relatively simple prescription for reducing excess work in more general near-equilibrium processes, where minimum-dissipation protocols follow geodesics of the Riemannian metric induced by the friction

tensor. For common unidirectional estimators near equilibrium, the bias and variance are proportional to the first moment (mean) of the excess work, and hence minimum-dissipation protocols defined by the friction tensor minimize both the bias and variance.

For bidirectional estimators, the variance is proportional to the sum of the second moments of the excess work from forward and reverse protocols (5.6b), while the bias is proportional to the difference of the first moments (5.6a).[155] This chapter extends the thermodynamic-geometry framework beyond the leading-order friction-tensor approximation, to higher-order moments of the excess work. For bidirectional estimators near equilibrium, minimum-variance protocols follow geodesics of the Riemannian metric induced by the friction tensor, while minimum-bias protocols follow geodesics of a cubic Finsler metric. For the simple model system of a Brownian particle in a quadratic trap with time-dependent stiffness (a *breathing harmonic trap*), the minimum-variance and minimum-bias protocols can improve variance by a factor of $3-4$ and bias by over a factor of 10 (Fig. 6.3). This chapter is adapted from the article published in Ref. 81.

6.1 Derivation

Chapter 4 introduced a geometric framework based on linear-response and slow-control approximations for determining protocols that minimize the average excess work (4.9), and chapter 5 discussed the relationship between the accuracy of free-energy estimates with excess work. Building on these results, the slow-control approximation is extended to account for both higher-order moments and higher-order corrections to excess work. This is then applied to improve the bias and variance of free-energy estimates.

The time derivative of the second moment of the excess-work distribution is[81]

$$\frac{\mathrm{d}\langle W_{\mathrm{ex}}^2\rangle_\Lambda}{\mathrm{d}t} = 2\dot{\lambda}_j(t)\int_0^t \mathrm{d}t'\ \langle \delta f_j(t)\delta f_\ell(t')\rangle_\Lambda\, \dot{\lambda}_\ell(t')\ . \tag{6.1}$$

For a sufficiently slow protocol, the nonequilibrium average $\langle\cdots\rangle_\Lambda$ is replaced with the equilibrium average $\langle\cdots\rangle_{\boldsymbol{\lambda}(t)}$ at fixed control parameters $\boldsymbol{\lambda}(t)$:

$$\frac{\mathrm{d}\langle W_{\mathrm{ex}}^2\rangle_\Lambda}{\mathrm{d}t} \approx 2\dot{\lambda}_j(t)\dot{\lambda}_\ell(t)\int_0^t \mathrm{d}t''\ \langle \delta f_j(0)\delta f_\ell(t'')\rangle_{\boldsymbol{\lambda}(t)}\ , \tag{6.2}$$

where I used the stationarity of the equilibrium average, defined $t'' \equiv t' - t$, and assumed smooth protocols to expand the control-parameter velocity to zeroth order, $\dot{\lambda}(t-t'') \approx \dot{\lambda}(t)$. Finally, assuming correlations in the conjugate forces relax quickly relative to the protocol duration, the integration bound t is replaced with ∞ (Appendix B.2) simplifying

the approximation to

$$\frac{\mathrm{d}\langle W_{\mathrm{ex}}^2\rangle_\Lambda}{\mathrm{d}t} \approx \frac{2}{\beta}\,\zeta_{j\ell}^{(1)}[\boldsymbol{\lambda}(t)]\dot{\lambda}_j(t)\dot{\lambda}_\ell(t)\ , \tag{6.3}$$

for the friction tensor

$$\zeta_{j\ell}^{(1)}[\boldsymbol{\lambda}(t)] \equiv \beta\int_0^\infty \mathrm{d}t''\,\langle \delta f_j(0)\delta f_\ell(t'')\rangle_{\boldsymbol{\lambda}(t)}\ . \tag{6.4}$$

In analogy with fluid dynamics, this rank-two tensor is the *Stokes' friction*, since it produces a drag force that depends linearly on velocity. In this chapter the Stokes' friction is denoted by a superscript (1) since it is the leading-order contribution to dissipation.[125] The Stokes' friction was previously presented in chapter 4 in (4.14) without a superscript.

Following parallel arguments, the third moment of the excess-work distribution is approximated as

$$\frac{\mathrm{d}\langle W_{\mathrm{ex}}^3\rangle_\Lambda}{\mathrm{d}t} \approx \frac{3}{\beta^2}\,\zeta_{j\ell m}^{(2)}[\boldsymbol{\lambda}(t)]\dot{\lambda}_j(t)\dot{\lambda}_\ell(t)\dot{\lambda}_m(t)\ , \tag{6.5}$$

for the rank-three tensor

$$\zeta_{j\ell m}^{(2)}[\boldsymbol{\lambda}(t)] \equiv -\beta^2\int_0^\infty \mathrm{d}t''\int_0^\infty \mathrm{d}t'''\,\langle \delta f_j(0)\delta f_\ell(t'')\delta f_m(t''')\rangle_{\boldsymbol{\lambda}(t)}\ . \tag{6.6}$$

(The factor of three in (6.5) results from grouping the index permutations $\{j\ell m, \ell jm, mj\ell\}$ into one term, making use of the invariance of the sum under exchange of indices, e.g., $\zeta_{j\ell m}^{(2)}\dot{\lambda}_j\dot{\lambda}_\ell\dot{\lambda}_m = \zeta_{\ell jm}^{(2)}\dot{\lambda}_j\dot{\lambda}_\ell\dot{\lambda}_m$.) I call the rank-three tensor (Eq. (6.6)) the *supra-Stokes'* tensor and index it by superscript (2), as it corresponds to the leading-order correction to dissipation beyond the Stokes' friction (6.12).

For fourth and higher moments, Appendix B.2 shows that the integration bounds must remain finite since the n-time covariance functions do not decay to zero at long time, so there is no clear analogy to frictional drag forces. Nevertheless, they can still be approximated by

$$\frac{\mathrm{d}\langle W_{\mathrm{ex}}^n\rangle_\Lambda}{\mathrm{d}t} \approx n\mathcal{C}_{\nu_1\cdots\nu_n}^{(n-1)}[\boldsymbol{\lambda}(t),t]\prod_{i=1}^n \dot{\lambda}_{\nu_j}(t)\ , \tag{6.7}$$

with index notation $\nu_1,\nu_2,\nu_3\cdots$ instead of j,ℓ,m, and integral n-time covariance functions

$$\mathcal{C}_{\nu_1\cdots\nu_n}^{(n-1)}[\boldsymbol{\lambda}(t),t] \equiv (-\beta)^n\prod_{i=2}^n\int_0^t \mathrm{d}t_j\left\langle\prod_{j=2}^n \delta f_{\nu_1}(0)\delta f_{\nu_\ell}(t_\ell)\right\rangle_{\boldsymbol{\lambda}(t)}\ . \tag{6.8}$$

This implies that higher-order moments of the excess work are higher order in control-parameter velocity and are therefore smaller for slow protocols. The approximations of (6.3), (6.5), and (6.7) are the leading-order contributions to each respective moment of the excess work.

To derive the next-order contribution, I exploit the connection between time-reversed protocols through the Crooks relation (3.17),[26,120] which constrains the probability of forward and reverse work measurements. Integrating (3.17) over W_{ex} produces Jarzynski's equality (3.18),[25] while first multiplying by W_{ex} then integrating leads to

$$\langle W_{\text{ex}} e^{-\beta W_{\text{ex}}} \rangle_{\Lambda} = -\langle W_{\text{ex}} \rangle_{\Lambda^\dagger} \ . \tag{6.9}$$

In this chapter, the forward protocol is denoted by Λ and the reverse protocol (starting at equilibrium in the end state of the forward protocol) by $\Lambda^\dagger$.

Taylor expanding the exponential in (3.18) and (6.9) to third order in excess work gives

$$\langle W_{\text{ex}} \rangle_{\Lambda} \approx \tfrac{1}{2}\beta \langle W_{\text{ex}}^2 \rangle_{\Lambda} - \tfrac{1}{6}\beta^2 \langle W_{\text{ex}}^3 \rangle_{\Lambda} \tag{6.10a}$$

$$\langle W_{\text{ex}} \rangle_{\Lambda^\dagger} \approx -\langle W_{\text{ex}} \rangle_{\Lambda} + \beta \langle W_{\text{ex}}^2 \rangle_{\Lambda} - \tfrac{1}{2}\beta^2 \langle W_{\text{ex}}^3 \rangle_{\Lambda} \ . \tag{6.10b}$$

According to (6.7), near equilibrium the higher-order moments of the excess work are higher order in control-parameter velocity and therefore can be neglected for slow protocols. The leading-order contributions to the sum and difference of the excess work are

$$\langle W_{\text{ex}} \rangle_{\Lambda} + \langle W_{\text{ex}} \rangle_{\Lambda^\dagger} \approx \beta \langle W_{\text{ex}}^2 \rangle_{\Lambda} \tag{6.11a}$$

$$\langle W_{\text{ex}} \rangle_{\Lambda} - \langle W_{\text{ex}} \rangle_{\Lambda^\dagger} \approx \tfrac{1}{6}\beta^2 \langle W_{\text{ex}}^3 \rangle_{\Lambda} \ . \tag{6.11b}$$

Differentiating (6.11a) and (6.11b) with respect to time, substituting in (6.3) and (6.5) respectively, then adding the two equations gives

$$\frac{\mathrm{d}\langle W_{\text{ex}} \rangle_{\Lambda}}{\mathrm{d}t} \approx \left\{ \zeta^{(1)}_{j\ell}[\boldsymbol{\lambda}(t)] + \frac{1}{4}\zeta^{(2)}_{j\ell m}[\boldsymbol{\lambda}(t)] \ \dot{\lambda}_m(t) \right\} \dot{\lambda}_j(t)\dot{\lambda}_\ell(t) \ . \tag{6.12}$$

Differentiating (6.10a) and substituting (6.12) and (6.5) gives

$$\frac{\mathrm{d}\langle W_{\text{ex}}^2 \rangle_{\Lambda}}{\mathrm{d}t} \approx \frac{2}{\beta} \left\{ \zeta^{(1)}_{j\ell}[\boldsymbol{\lambda}(t)] + \frac{3}{4}\zeta^{(2)}_{j\ell m}[\boldsymbol{\lambda}(t)] \ \dot{\lambda}_m(t) \right\} \dot{\lambda}_j(t)\dot{\lambda}_\ell(t) \ . \tag{6.13}$$

Approximations for higher-order moments are derived by following parallel arguments.

Multiplying (3.17) by $W_{\rm ex}^n$ and integrating over $W_{\rm ex}$ gives

$$\langle (-W_{\rm ex})^n \rangle_{\Lambda^\dagger} = \langle W_{\rm ex}^n \rangle_\Lambda - \beta \langle W_{\rm ex}^{n+1} \rangle_\Lambda + \frac{\beta^2}{2} \langle W_{\rm ex}^{n+2} \rangle_\Lambda + \cdots \ . \tag{6.14}$$

Adding $\langle (-W_{\rm ex})^n \rangle_{\Lambda^\dagger}$ and rearranging leads to

$$\langle W_{\rm ex}^n \rangle_\Lambda + \langle (-W_{\rm ex})^n \rangle_{\Lambda^\dagger} = 2 \langle (-W_{\rm ex})^n \rangle_{\Lambda^\dagger} + \beta \langle W_{\rm ex}^{n+1} \rangle_\Lambda - \frac{\beta^2}{2} \langle W_{\rm ex}^{n+2} \rangle_\Lambda + \cdots \ , \tag{6.15}$$

while subtracting $\langle (-W_{\rm ex})^n \rangle_{\Lambda^\dagger}$ yields

$$\langle W_{\rm ex}^n \rangle_\Lambda - \langle (-W_{\rm ex})^n \rangle_{\Lambda^\dagger} = \beta \langle W_{\rm ex}^{n+1} \rangle_\Lambda - \frac{\beta^2}{2} \langle W_{\rm ex}^{n+2} \rangle_\Lambda + \cdots \ . \tag{6.16}$$

For $n > 2$, the higher-order powers of the excess work are also higher order in control-parameter velocity ($n = 1$ (6.12) and $n = 2$ (6.13) are the same order in control-parameter velocity); therefore, the leading-order contributions to the sum (6.15) and difference (6.16) for $n > 2$ are

$$\langle W_{\rm ex}^n \rangle_\Lambda + \langle (-W_{\rm ex})^n \rangle_{\Lambda^\dagger} \approx 2 \langle (-W_{\rm ex})^n \rangle_\Lambda \tag{6.17a}$$

$$\langle W_{\rm ex}^n \rangle_\Lambda - \langle (-W_{\rm ex})^n \rangle_{\Lambda^\dagger} \approx \beta \langle W_{\rm ex}^{n+1} \rangle_\Lambda \ , \tag{6.17b}$$

which implies

$$\beta^{n-1} \frac{\mathrm{d} \langle W_{\rm ex}^n \rangle_\Lambda}{\mathrm{d}t} \approx \left\{ n \, \mathcal{C}^{(n-1)}_{\nu_1 \cdots \nu_n}[\boldsymbol{\lambda}(t), t] + \frac{n+1}{2} \, \mathcal{C}^{(n)}_{\nu_1 \cdots \nu_{n+1}}[\boldsymbol{\lambda}(t), t] \ \dot{\lambda}_{\nu_{n+1}}(t) \right\} \prod_{i=1}^{n} \dot{\lambda}_{\nu_j}(t) \ . \tag{6.18}$$

Equations (6.12), (6.13), and (6.18) are the central results of this chapter, which have applications to designing minimum-dissipation and optimal free energy estimation protocols.

6.2 Next-order contribution to excess work

The approximation of (6.12) can improve near-equilibrium estimates of the excess work. The leading-order term is the usual linear-response approximation (4.14) and is positive for all protocols. The Stokes' friction (6.4) is an autocovariance function,

$$\zeta^{(1)}_{j\ell}[\boldsymbol{\lambda}(t)] = \langle \delta f_j \delta f_\ell \rangle_{\boldsymbol{\lambda}(t)} \circ \tau^{(1)}_{j\ell}[\boldsymbol{\lambda}(t)] \ , \tag{6.19}$$

the Hadamard (entry-by-entry) product, $\circ$, of the conjugate-force covariance $\langle \delta f_j \delta f_\ell \rangle_{\boldsymbol{\lambda}(t)}$ and integral relaxation time

$$\tau^{(1)}_{j\ell}[\boldsymbol{\lambda}(t)] \equiv \int_0^\infty \mathrm{d}t'' \frac{\langle \delta f_j(0) \delta f_\ell(t'') \rangle_{\boldsymbol{\lambda}(t)}}{\langle \delta f_j \delta f_\ell \rangle_{\boldsymbol{\lambda}(t)}} \ . \tag{6.20}$$

The Stokes' friction is largest when the conjugate-force fluctuations are largest (large covariance) and most persistent (long relaxation time). In contrast to the positive contribution from the Stokes' friction, the contribution from the supra-Stokes' tensor (second term in (6.12)) changes sign under time reversal because it is cubic in control-parameter velocity. The supra-Stokes' tensor (6.6)

$$\zeta^{(2)}_{j\ell m}[\boldsymbol{\lambda}(t)] = -\langle \delta f_j \delta f_\ell \delta f_m \rangle_{\boldsymbol{\lambda}(t)} \circ \tau^{(2)}_{j\ell m}[\boldsymbol{\lambda}(t)] \tag{6.21}$$

is not positive semidefinite, and is the Hadamard product of the unnormalized coskewness $\langle \delta f_j \delta f_\ell \delta f_m \rangle_{\boldsymbol{\lambda}(t)}$ (related to skewness as covariance is related to variance) and the integral double relaxation time

$$\tau^{(2)}_{j\ell m}[\boldsymbol{\lambda}(t)] \equiv \int_0^\infty \mathrm{d}t'' \int_0^\infty \mathrm{d}t''' \frac{\langle \delta f_j(0) \delta f_\ell(t'') \delta f_m(t''') \rangle_{\boldsymbol{\lambda}(t)}}{\langle \delta f_j \delta f_\ell \delta f_m \rangle_{\boldsymbol{\lambda}(t)}} \ . \tag{6.22}$$

For a protocol with positive velocity, the contribution to dissipation from the supra-Stokes' tensor quantifies the increase (decrease) in excess work from negatively (positively) skewed conjugate-force fluctuation.

The leading-order friction-tensor approximation (first term in (6.12)) endows the control-parameter space with a Riemannian metric, such that minimum-work protocols follow geodesics of the Stokes' friction tensor. With the addition of the next-order contribution (6.6), the excess work can be expressed as

$$\langle W_{\mathrm{ex}} \rangle_\Lambda \approx \int_0^{\Delta t} \mathrm{d}t \, \zeta^{\mathrm{tot}}_{j\ell}[\boldsymbol{\lambda}(t), \dot{\boldsymbol{\lambda}}(t)] \ \dot{\lambda}_j(t) \dot{\lambda}_\ell(t) \ , \tag{6.23}$$

for total friction tensor

$$\zeta^{\mathrm{tot}}_{j\ell}[\boldsymbol{\lambda}(t), \dot{\boldsymbol{\lambda}}(t)] \equiv \zeta^{(1)}_{j\ell}[\boldsymbol{\lambda}(t)] + \tfrac{1}{4} \zeta^{(2)}_{j\ell m}[\boldsymbol{\lambda}(t)] \ \dot{\lambda}_m(t) \tag{6.24}$$

that explicitly depends on the protocol velocity. Minimum-dissipation protocols follow geodesics of the generalized cubic Finsler metric $\zeta^{\mathrm{tot}}_{j\ell}[\boldsymbol{\lambda}(t), \dot{\boldsymbol{\lambda}}(t)]$, an extension of the Riemannian metric $\zeta^{(1)}_{j\ell}[\boldsymbol{\lambda}(t)]$. A Finsler metric defines a space where distances depend not only on positions (points) but also on directions (tangent vectors). Nevertheless, the usual concepts of length, curvature, and geodesics from Riemannian geometry generalize, and there are standard procedures for calculating geodesics[164] (Appendix B.3). For small

control-parameter velocities, the total friction is positive semi-definite; however, for large control-parameter velocities the approximation breaks down and no longer guarantees positive semidefiniteness, leading to the unphysical possibility of negative excess work.

To illustrate some general properties of the friction, Fig. 6.1 shows, for the model system of a *breathing harmonic trap* (Brownian particle in a harmonic trap where the control parameter is the time-dependent stiffness, Appendix B.1), the (a) force variance, (b) Stokes' friction, (c) supra-Stokes' contribution, and (d) total friction. The force variance and Stokes' friction are independent of control-parameter velocity. In general, the force variance differs from the Stokes' friction by a factor of the integral relaxation time, which varies with the control-parameter value (trap stiffness) for the breathing harmonic trap. The contribution from the supra-Stokes' tensor (c) is antisymmetric in control-parameter velocity, becoming negative for negative velocity. This antisymmetric contribution skews the total friction (d), which depends on the control-parameter velocity and lacks any symmetry under time reversal.

Geodesics (solid curves in Fig. 6.1) are protocols that minimize the contribution from the corresponding metric to the excess work. For relatively fast protocols (average scaled velocities of $\dot{\lambda}^* = \dot{k}/k_\mathrm{i} \gtrsim 0.5$ or $\lesssim -0.5$, for initial stiffness k_i), the velocity is significantly smaller in regions of high friction and larger in regions of low friction (or force variance).

6.3 Precision and accuracy of free-energy estimates

In this thesis, the precision of a free-energy estimator is quantified by its variance. In the limit of many samples, the expected variance of any unbiased estimator $\widehat{\Delta F}$ is bounded by a nonequilibrium average over a total of $N = N_\mathrm{F} + N_\mathrm{R}$ forward and reverse work measurements (5.4).[153]

Assuming small excess work, the variance is expanded as

$$\left\langle \left(\widehat{\Delta F} - \Delta F_\mathrm{eq} \right)^2 \right\rangle \approx \frac{\langle W_\mathrm{ex}^2 \rangle_\Lambda + \langle W_\mathrm{ex}^2 \rangle_{\Lambda^\dagger}}{2N} \tag{6.25a}$$

$$\approx \frac{2}{\beta N} \int_0^{\Delta t} \mathrm{d}t \, \zeta_{j\ell}^{(1)}[\boldsymbol{\lambda}(t)] \; \dot{\lambda}_j(t) \dot{\lambda}_\ell(t) \; , \tag{6.25b}$$

where the second line assumes the slow-control approximation for the variance (6.13). Equation (6.25a) also holds for very few samples, since then BAR is equivalent to the average of the sum of the forward and reverse work measurements.[155] The protocol designed to reduce the variance follows geodesics of $\zeta_{j\ell}^{(1)}$, and for one-dimensional control proceeds at velocity $\dot{\lambda} \propto \left(\zeta^{(1)} \right)^{-1/2}$.

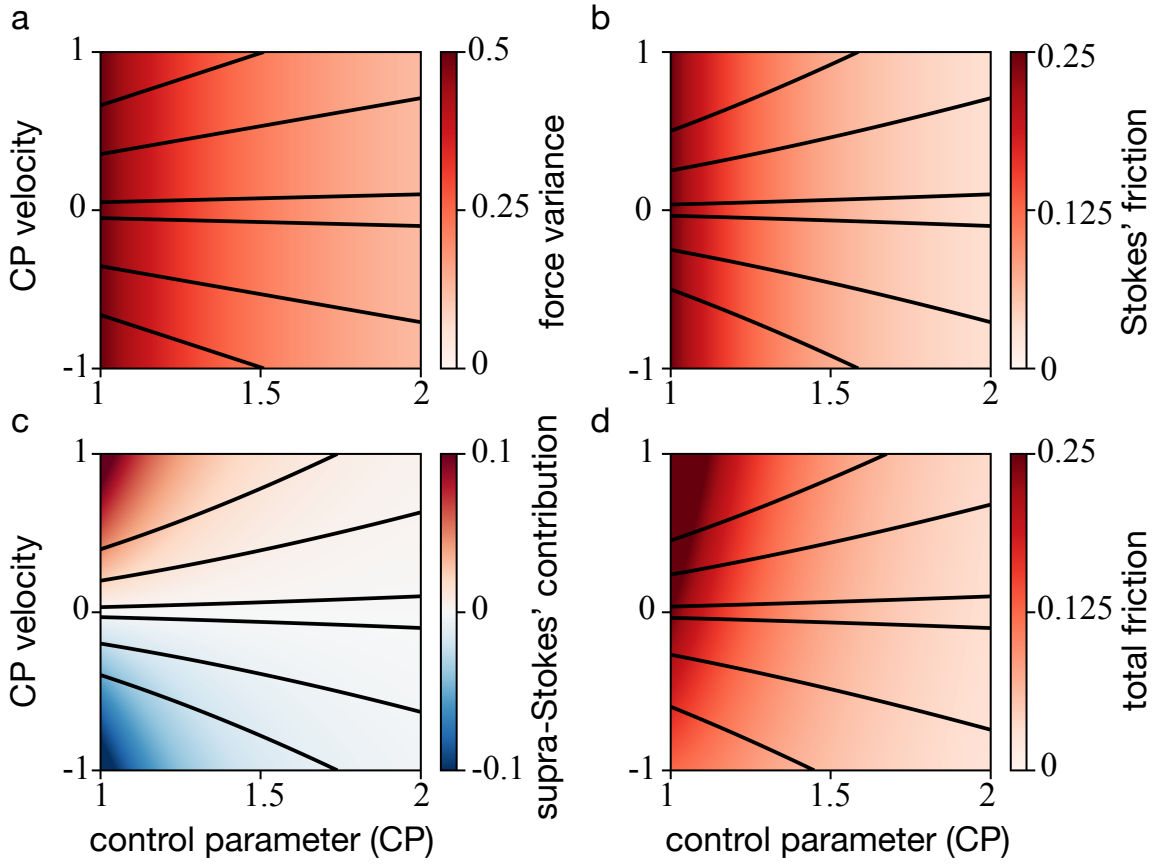

Fig 6.1. Friction as a function of control-parameter velocity $\dot{\lambda}^*$ and control parameter λ^* for the breathing harmonic trap. Scaled (a) force variance $\langle \delta f^2 \rangle^* \equiv \beta^2 k_\mathrm{i}^2 \langle \delta f^2 \rangle$, (b) Stokes' friction $\zeta^{(1)*} \equiv \beta^3 D k_\mathrm{i}^3 \zeta^{(1)}$, (c) supra-Stokes' contribution $\frac{1}{4}\dot{\lambda}^* \zeta^{(2)*} \equiv \frac{1}{4}\beta^3 D k_\mathrm{i}^3 \dot{k} \zeta^{(2)}$, and (d) total friction $\zeta^{\mathrm{tot}*} \equiv \beta^3 D k_\mathrm{i}^3 \zeta^{\mathrm{tot}}$, for initial trap stiffness k_i and diffusivity D. The control parameter is the trap stiffness, given in dimensionless form as $\lambda^* \equiv k/k_\mathrm{i}$ with velocity $\dot{\lambda}^* = \dot{k}/(\beta D k_\mathrm{i}^2)$. Geodesics (solid curves) minimize the magnitude of the corresponding metric's contribution to the excess work, with distinct curves representing different average protocol velocities.

Unlike the protocol that minimizes the variance, the protocol that maximizes the accuracy (minimum-bias) is different for unidirectional and bidirectional estimators. For unidirectional Jarzynski and mean-work estimators, near equilibrium the minimum-bias protocol is simply the minimum-dissipation protocol (protocol that minimizes (6.12)) and therefore to leading order is optimized by the same protocol that minimizes (6.25b). For BAR, for small excess work (or few samples), the bias instead is proportional to the difference between the forward and reverse excess work:[155]

$$\left\langle \widehat{\Delta F} \right\rangle - \Delta F_{\mathrm{eq}} \approx \frac{1}{2N} \left(\langle W_{\mathrm{ex}} \rangle_{\Lambda} - \langle W_{\mathrm{ex}} \rangle_{\Lambda^\dagger} \right) \tag{6.26a}$$

$$\approx \frac{1}{4N} \int_0^{\Delta t} \mathrm{d}t \, \zeta^{(2)}_{j\ell m}[\boldsymbol{\lambda}(t)] \, \dot{\lambda}_j(t) \dot{\lambda}_\ell(t) \dot{\lambda}_m(t) \ , \tag{6.26b}$$

where the second line follows from the supra-Stokes' approximation for the mean work (6.12). The protocol designed to reduce the (magnitude of) bias thus follows geodesics of the cubic Finsler metric $\zeta^{(2)}_{j\ell m}$, simplifying for one-dimensional control to $\dot{\lambda} \propto \left(\zeta^{(2)}\right)^{-1/3}$. Figure 6.2 plots these protocols for the model system of a breathing harmonic trap (Appendix B.1) alongside the naive (constant-velocity) protocol.

To illustrate the potential benefit of protocols designed to reduce variance and bias, Fig. 6.3 shows approximations for the variance (6.25a) and bias (6.26a) of designed and naive protocols, as well as their ratio, as a function of protocol duration, for the model system of a breathing harmonic trap (Appendix B.1). For a slow protocol (protocol duration longer than the slowest relaxation time, $\Delta t / \tau_{\mathrm{f}}^{(1)} \gtrsim 1$), the designed protocols reduce the variance by a factor of $3 - 4$ (Fig. 6.3c), with the precise protocol (designed to reduce variance) performing the best (smallest ratio). For the bias, the accurate protocol (designed to reduce bias) performs the best (smallest ratio), with reductions by an order of magnitude for the slowest protocols shown (Fig. 6.3d). For fast protocols (protocol duration shorter than the slowest relaxation time, $\Delta t / \tau_{\mathrm{f}}^{(1)} \lesssim 1$), the approximations break down, and the naive protocol can outperform the designed in both bias and variance (ratio larger than one). For this system the minimum-variance and minimum-bias protocols achieve similar amounts of bias and variance in all cases, likely due to their similar functional form (Fig. 6.2).

6.4 Discussion

This chapter has developed near-equilibrium approximations for moments of the excess work, (6.12), (6.13), and (6.18), that incorporate time-reversal symmetric and antisymmetric contributions. The antisymmetric contribution to the first moment (6.12) yields the next-order contribution beyond linear response, which asymmetrically skews the Riemannian metric (6.4) into a generalized cubic Finsler metric (6.24). The Stokes' friction

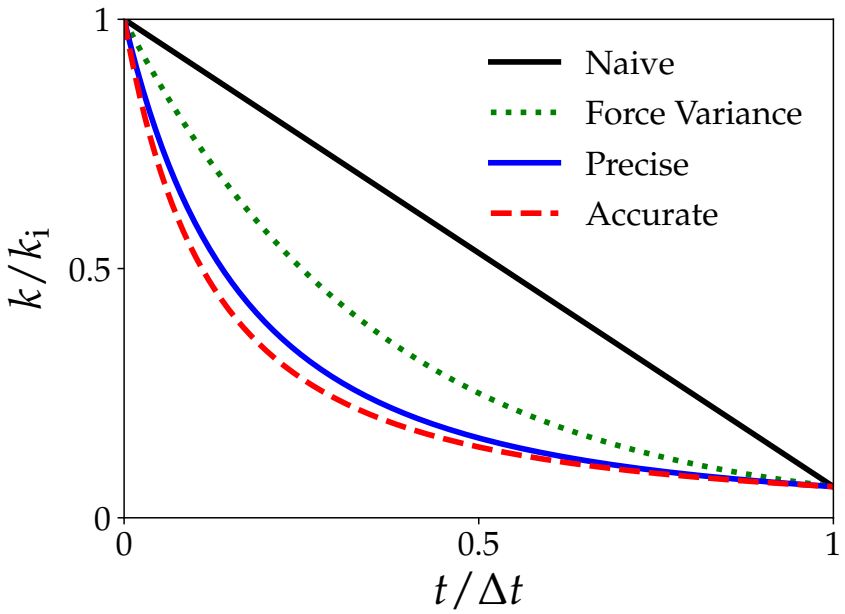

Fig 6.2. The control parameter (trap stiffness k) as a function of time for three different protocols in the model system of a breathing harmonic trap. The control-parameter protocol drives the system between relatively strongly and weakly confined states ($k_\mathrm{f}/k_\mathrm{i} = 1/16$). "Naive" denotes the constant-velocity protocol, "Force Variance" the force-variance-optimized protocol proceeding according to $\dot{k} \propto k$, "Accurate" the minimum-variance protocol with $\dot{k} \propto k^{3/2}$, and "Precise" the minimum-bias protocol with $\dot{k} \propto k^{5/3}$.

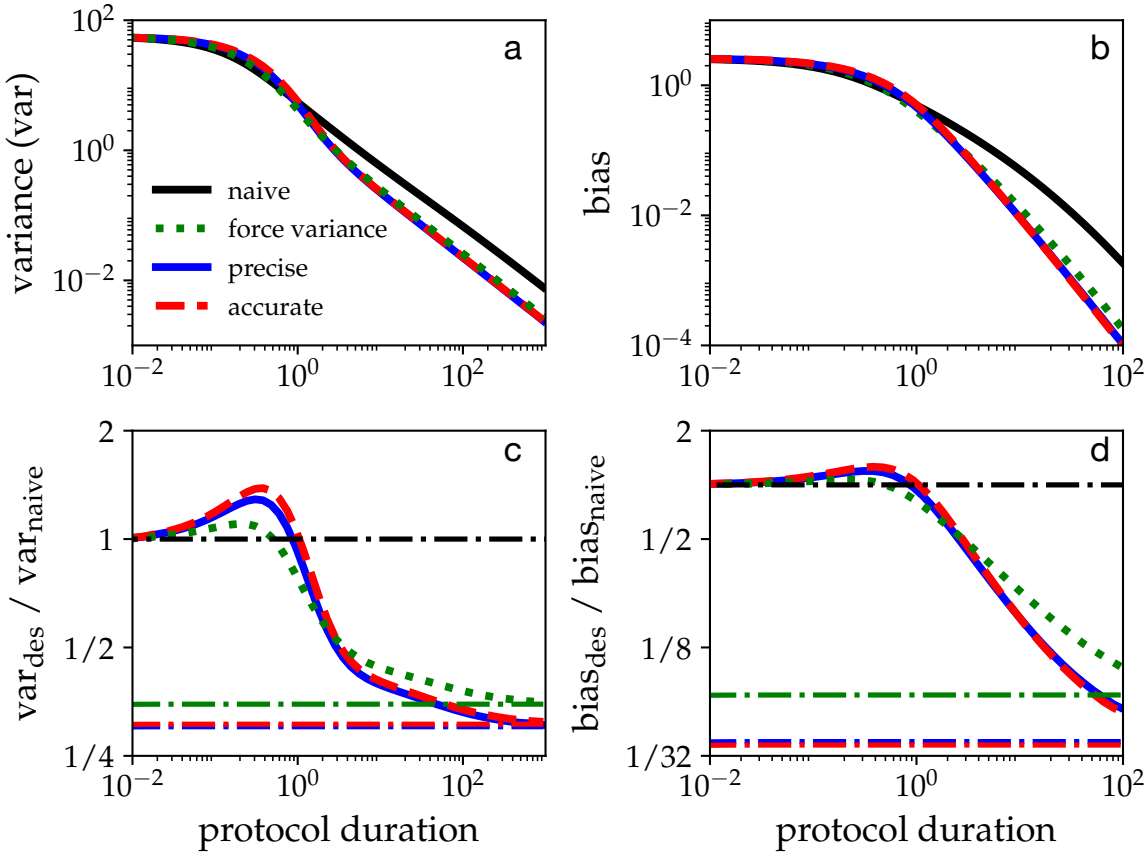

Fig 6.3. (a) Scaled variance $\langle(\beta\,\delta\widehat{\Delta F})^2\rangle/N$ (6.25a) and (b) scaled bias $\langle\beta\,\delta\widehat{\Delta F}\rangle/N$ (6.26a) as functions of scaled protocol duration $\Delta t/\tau_{\rm f}^{(1)}$ (for slowest relaxation time $\tau_{\rm f}^{(1)} = (2\beta D k_{\rm f})^{-1}$), for the breathing harmonic trap. Ratios of designed and naive (c) variances $\langle(\delta\widehat{\Delta F})^2\rangle_{\rm des}/\langle(\delta\widehat{\Delta F})^2\rangle_{\rm naive}$ and (d) biases $\langle\delta\widehat{\Delta F}\rangle_{\rm des}/\langle\delta\widehat{\Delta F}\rangle_{\rm naive}$. Subscript "naive" denotes the constant-velocity protocol, and "des" the designed protocols, which are the force-variance-optimized "force variance", the minimum-variance "accurate", and the minimum-bias "precise" protocols. Dash-dotted lines denote the limits for short (black) and long duration (colors). Final control-parameter value (trap stiffness) is $k_{\rm f}/k_{\rm i} = 1/16$.

tensor (6.4) controls the leading-order contribution to the variance of both unidirectional and bidirectional free-energy estimators (6.13), such that minimum-variance protocols follow geodesics of the Stokes' friction. For unidirectional estimators, these same protocols also minimize the bias; however, for bidirectional estimators such as BAR the leading-order contribution to the bias is from the supra-Stokes' tensor (6.26b), and therefore minimum-bias protocols instead follow geodesics of the supra-Stokes' tensor. From these near-equilibrium approximations, protocols are designed that increase the precision and accuracy of standard nonequilibrium free-energy estimators (Fig. 6.3).

The addition of the supra-Stokes' tensor has several physical implications. Notably, it accounts for time-reversal asymmetric dissipation, which arises from skewed conjugate-force fluctuations. Since the supra-Stokes' contribution is antisymmetric, it cancels out for equal numbers of forward and reverse protocols, which has implications for the design principles of molecular machines: many molecular machines (e.g., kinesin walking toward a microtubule's plus end[165] or ATP synthase synthesizing ATP[166]) achieve directed behavior; the supra-Stokes' tensor quantifies the leading-order energetic cost of directed operation compared to a coequal forward and reverse process.

In some cases the minimum-work protocols can be calculated exactly,[41,44] or minimum-variance protocols solved numerically,[167,168] which would yield more accurate and precise estimators; however, to date these optimizations are limited to simple systems and do not permit straightforward generalization. The present formalism can be applied to more general settings than exact calculations and makes fewer approximations than Ref. 147, which only examines the force-variance metric and does not consider minimizing bias.

This chapter considered continuous protocols, but free energies are often estimated from sampling discrete states.[169–172] Additionally, for discrete-state sampling in replica-exchange[173] or parallel-tempering[174] simulations it is important to consider the acceptance probability between states.[175–183] The force-variance metric has been applied in this context,[147] and the linear-response framework of Ref. 125 has been generalized to discrete control.[73] As Ref. 147 has shown, spacing the states along geodesics of the force variance not only reduces the variance of the free-energy estimator but also increases the acceptance probability. Analogous principles may hold for designing minimum-variance and minimum-bias protocols for discrete-state sampling using the milder approximations derived in this chapter.

Chapter 7

Fast Control

While minimum-dissipation protocols for slowly driven systems are relatively well understood, comparatively little is known about rapidly driven systems. In this chapter I focus on fast protocols and find a universal design principle: the minimum-dissipation protocol consists of jumps at the beginning and end of the protocol, spending the entire duration at the control-parameter value that optimally balances the *initial force-relaxation rate* (IFRR) (7.5b) with the jump size (7.11). The results in this chapter are physically intuitive, apply to a wide range of stochastic systems, and generalize easily to multiparameter control. To illustrate this, minimum-dissipation protocols are calculated for a diverse set of systems described by Fokker-Planck or master-equation dynamics with single- (Fig. 7.1) or multiparameter control (Fig. 7.4). Combining results with known minimum-dissipation protocols in the slow limit,[125] it is demonstrated that a simple interpolation scheme produces protocols that reduce dissipation at all speeds (Fig. 7.3). This chapter is adapted from the published article in Ref. 47.

7.1 Derivation

Consider a stochastic thermodynamic system described by dynamics of the form (3.1); e.g., Fokker-Planck or Master-equation dynamics. If the total duration Δt is short compared to the system's natural relaxation time τ (a fast protocol), expanding the probability distribution in $\Delta t/\tau$ around an initial equilibrium distribution $\pi_{\mathrm{i}}(\boldsymbol{r})$ gives

$$p_s(\boldsymbol{r},\boldsymbol{\Lambda}) = \pi_{\mathrm{i}}(\boldsymbol{r}) + p_s^{(1)}(\boldsymbol{r},\boldsymbol{\Lambda})\frac{\Delta t}{\tau} + \mathcal{O}\left[\left(\frac{\Delta t}{\tau}\right)^2\right] , \tag{7.1}$$

for $s \equiv t/\Delta t$ and first-order coefficient $p_s^{(1)}(\boldsymbol{r}, \boldsymbol{\Lambda})$. Plugging (7.1) up to $\mathcal{O}(\Delta t/\tau)$ into (3.1) gives

$$\frac{\partial p_s^{(1)}(\boldsymbol{r}, \boldsymbol{\Lambda})}{\partial s} \approx \mathcal{L}[x, \boldsymbol{\lambda}(s)]\, \pi_{\mathrm{i}}(\boldsymbol{r}) \;, \tag{7.2}$$

with $\mathcal{L} \equiv \tau L$ the dimensionless time-evolution operator. Solving for $p_s^{(1)}(\boldsymbol{r}, \boldsymbol{\Lambda})$ and substituting into (7.1) yields

$$p_s(\boldsymbol{r}, \boldsymbol{\Lambda}) \approx \pi_{\mathrm{i}}(\boldsymbol{r}) + \frac{\Delta t}{\tau} \int_0^s \mathrm{d}s' \mathcal{L}[x, \boldsymbol{\lambda}(s')]\, \pi_{\mathrm{i}}(\boldsymbol{r}) \;. \tag{7.3}$$

Multiplying by conjugate forces $\mathbf{f}$, integrating over microstates x, and changing the time variable back to t gives

$$\langle \mathbf{f}(t) \rangle_\Lambda \approx \langle \mathbf{f} \rangle_{\boldsymbol{\lambda}_{\mathrm{i}}} + \int_0^t \mathrm{d}t'\, \mathbf{R}_{\boldsymbol{\lambda}_{\mathrm{i}}}[\boldsymbol{\lambda}(t')] \;, \tag{7.4}$$

for the *initial force-relaxation rate* (IFRR)

$$\mathbf{R}_{\boldsymbol{\lambda}_{\mathrm{i}}}[\boldsymbol{\lambda}(t)] \equiv \int \mathrm{d}\boldsymbol{r}\; \mathbf{f}(\boldsymbol{r})\, L[x, \boldsymbol{\lambda}(t)]\, \pi_{\mathrm{i}}(\boldsymbol{r}) \tag{7.5a}$$

$$= \left. \frac{\mathrm{d}\langle \mathbf{f} \rangle_{\boldsymbol{\lambda}_{\mathrm{i}}}}{\mathrm{d}t} \right|_{\boldsymbol{\lambda}(t)} \;, \tag{7.5b}$$

the rate of change of the conjugate forces at the current control-parameter values (averaged over the initial equilibrium distribution).

Within this approximation, the average excess work (4.9) is

$$\langle W_{\mathrm{ex}} \rangle_\Lambda \approx \langle W_{\mathrm{ex}} \rangle_{\boldsymbol{\lambda}_{\mathrm{i}}} - \int_0^{\Delta t} \mathrm{d}t\, \frac{\mathrm{d}\boldsymbol{\lambda}^{\mathrm{T}}}{\mathrm{d}t} \int_0^t \mathrm{d}t'\, \mathbf{R}_{\boldsymbol{\lambda}_{\mathrm{i}}}[\boldsymbol{\lambda}(t')] \;. \tag{7.6}$$

The first RHS term is the excess work during an instantaneous jump between the initial and final control-parameter values, which equals the *relative entropy* $k_{\mathrm{B}}TD(\pi_{\mathrm{i}}||\pi_{\mathrm{f}}) \equiv k_{\mathrm{B}}T \int \mathrm{d}x\; \pi_{\mathrm{i}} \ln[\pi_{\mathrm{i}}/\pi_{\mathrm{f}}]$ between the initial π_{i} and final π_{f} equilibrium probability distributions.[73] Integrating (7.6) by parts gives this chapter's main theoretical result: for sufficiently short duration, the excess work is

$$\langle W_{\mathrm{ex}} \rangle_\Lambda \approx k_{\mathrm{B}}TD(\pi_{\mathrm{i}}||\pi_{\mathrm{f}}) - \int_0^{\Delta t} \mathrm{d}t\, \mathbf{R}_{\boldsymbol{\lambda}_{\mathrm{i}}}^{\mathrm{T}}[\boldsymbol{\lambda}(t)]\, [\boldsymbol{\lambda}_{\mathrm{f}} - \boldsymbol{\lambda}(t)] \;. \tag{7.7}$$

The second RHS term is the first-order correction in Δt, an approximation for the saved work $W_{\mathrm{save}} \equiv k_{\mathrm{B}}TD(\pi_{\mathrm{i}}||\pi_{\mathrm{f}}) - W_{\mathrm{ex}}$ compared to an instantaneous protocol. I emphasize that

these results stem from the short-time approximation of (7.1) and do not involve any linear-response approximation. Rather than the small-force and long-duration approximations typical of linear-response and steady-state frameworks,[184–186] I make no direct assumptions on the strength of driving and instead assume a short duration so that the probability distribution remains near the initial equilibrium distribution.

7.2 Initial Force-Relaxation Rate

The IFRR can be intuitively understood by considering one-parameter exponential relaxation. For a discrete jump from initial control-parameter value λ_i to an intermediate value λ, an exponentially relaxing mean conjugate force obeys

$$\langle f(t)\rangle_\Lambda = \langle f\rangle_{\lambda_\mathrm{i}} + (\langle f\rangle_\lambda - \langle f\rangle_{\lambda_\mathrm{i}})\, e^{-t/\tau(\lambda)} \;, \tag{7.8}$$

where $\tau(\lambda)$ is the relaxation time of the conjugate force. The IFRR is the initial slope of the mean conjugate force as it relaxes towards equilibrium (7.5b), which for exponential relaxation is

$$R_{\lambda_\mathrm{i}}(\lambda) = \frac{\langle f\rangle_{\lambda_\mathrm{i}} - \langle f\rangle_\lambda}{\tau(\lambda)} \;. \tag{7.9}$$

Under simple exponential relaxation, $\tau(\lambda)$ is the same relaxation time defined in Ref. 125 for slow protocols, thereby connecting short- and long-duration control.

For a small control-parameter jump $\lambda - \lambda_\mathrm{i}$, static linear-response theory, $\langle f\rangle_{\lambda_\mathrm{i}} - \langle f\rangle_\lambda \approx \beta(\lambda - \lambda_\mathrm{i})\langle \delta f^2\rangle_{\lambda_\mathrm{i}}$, implies that the IFRR further simplifies to

$$R_{\lambda_\mathrm{i}}(\lambda) \approx \frac{\langle \delta f^2\rangle_{\lambda_\mathrm{i}}(\lambda - \lambda_\mathrm{i})}{\tau(\lambda)} \;. \tag{7.10}$$

The relaxation rate is zero at the initial control-parameter value and increases with larger control-parameter jumps which drive the system further from equilibrium.

7.3 Minimum-dissipation protocols

Equation (7.7) allows for relatively straightforward optimization to determine the *short-time efficient protocol* (STEP), satisfying the Euler-Lagrange equation

$$\frac{\partial}{\partial \boldsymbol{\lambda}} \left[\mathbf{R}^\mathrm{T}_{\boldsymbol{\lambda}_\mathrm{i}}(\boldsymbol{\lambda}) \left(\boldsymbol{\lambda}_\mathrm{f} - \boldsymbol{\lambda}^\mathrm{STEP} \right) \right] \Big|_{\boldsymbol{\lambda}^\mathrm{STEP}} = \mathbf{R}_{\boldsymbol{\lambda}_\mathrm{i}} \left(\boldsymbol{\lambda}^\mathrm{STEP} \right) \;. \tag{7.11}$$

As an algebraic equation, the solution is a point in control-parameter space, thus the STEP consists of two jumps: a jump at the start from its initial value to the optimal value $\boldsymbol{\lambda}^{\mathrm{STEP}}$, and at the end from the optimal value to the final value. The STEP is a jump protocol provided the time-evolution operator L is independent of time derivatives of the control parameters. For Fokker-Planck dynamics this is satisfied if the system is driven by a (generally time-dependent) scalar potential.

To illustrate the two-step minimum-dissipation protocol the STEP has been calculated for diverse model systems (Fig. 7.1). In the translating- and breathing-trap systems described by Fokker-Planck dynamics (Appendix C.1), the STEP jumps halfway between the two endpoints, consistent with the results of Ref. 41. The single-spin-flip and two-state binding/unbinding reaction systems are described by master-equation dynamics (Appendices C.2 and C.3), with STEPs that jump to points that are respectively more and less than halfway between the initial and final control-parameter values. Specific jump sizes for the STEP depend on the functional form of the IFRR, but the minimum-dissipation protocol always consists of jumps to and from an intermediate control-parameter value.

The STEP jumps to the point in control-parameter space that maximizes the *short-time power savings*

$$P^{\mathrm{st}}_{\mathrm{save}}(\boldsymbol{\lambda}) \equiv \mathbf{R}^{\mathrm{T}}_{\boldsymbol{\lambda}_{\mathrm{i}}}(\boldsymbol{\lambda})(\boldsymbol{\lambda}_{\mathrm{f}} - \boldsymbol{\lambda}) \tag{7.12}$$

due to relaxation at intermediate $\boldsymbol{\lambda}$. The STEP balances fast relaxation rate $\mathbf{R}_{\boldsymbol{\lambda}_{\mathrm{i}}}$ with large final jump $\boldsymbol{\lambda}_{\mathrm{f}} - \boldsymbol{\lambda}$. The STEP spends the duration Δt relaxing at $\boldsymbol{\lambda}^{\mathrm{STEP}}$, so for short duration $P^{\mathrm{st}}_{\mathrm{save}}(\boldsymbol{\lambda}^{\mathrm{STEP}})\Delta t$ is the work saved relative to an instantaneous protocol.

To demonstrate the energetics of the STEP, consider the thermodynamic cycle consisting of tightening and loosening a harmonic trap (Fig. 7.2). For a quasistatic (infinitely slow) protocol, work equals the free-energy difference, which exactly cancels for a cyclic process. An instantaneous protocol has an additional contribution, which for tightening (loosening) the trap equals the relative entropy between the open (closed) and closed (open) states. The relative entropy is dissipated as heat during equilibration between tightening and loosening the trap (outer vertical arrows). The STEP spends the duration relaxing at an intermediate control-parameter value, resulting in saved work approximated by the area of the rectangle with width given by the final jump size $\lambda_{\mathrm{f}} - \lambda^{\mathrm{STEP}}$ and height by $R_{\lambda_{\mathrm{i}}}(\lambda^{\mathrm{STEP}})\Delta t$. To maximize the saved work (rectangle area) the STEP optimally balances the IFRR (determining the height) with final jump size (width). The saved work and IFRR at the STEP value are larger when tightening the trap compared to loosening since the relaxation rate is limited by diffusion when loosening the trap while the relaxation when tightening is sped up by the force applied by the trap.

For a single control parameter, if the duration is sufficiently short the *gain* $G_{\mathrm{save}} \equiv$

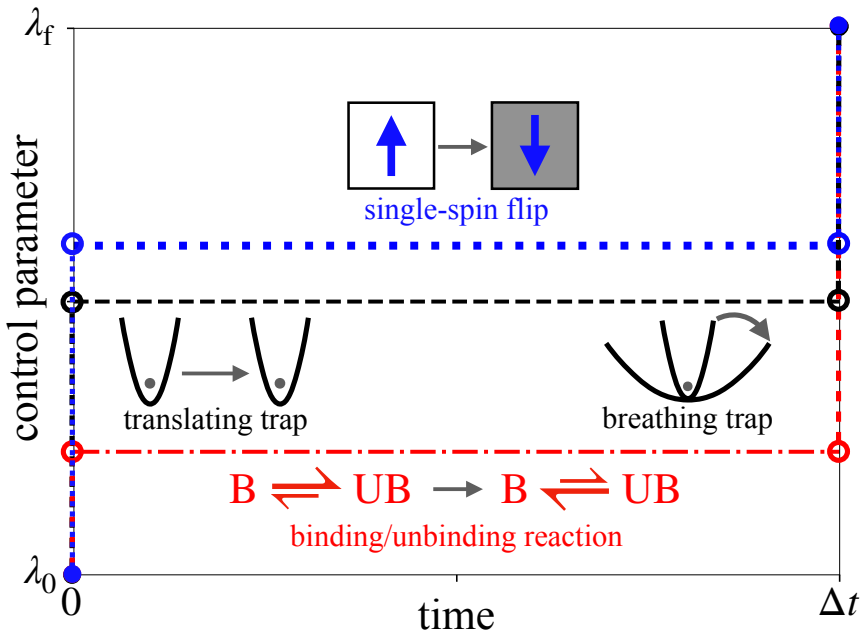

Fig 7.1. Short-time efficient protocols (STEPs) for a single spin in a time-dependent magnetic field (blue dots), Brownian particle in a translating harmonic potential (black dashed), Brownian particle in a harmonic potential with time-dependent stiffness (black dashed), and a two-state binding/unbinding reaction system with variable binding and unbinding rates controlled by the chemical-potential difference (red dash-dotted). For the single-spin system the initial and final magnetic fields are $\beta h_\mathrm{i} = -2$ and $\beta h_\mathrm{f} = 2$, and for the binding/unbinding reaction the initial and final chemical potentials are $\beta\mu_\mathrm{i}^\mathrm{chem} = -3 + \ln 2$ and $\beta\mu_\mathrm{f}^\mathrm{chem} = 3 + \ln 2$. For the breathing and translating traps the STEP value is always halfway between the control-parameter endpoints.

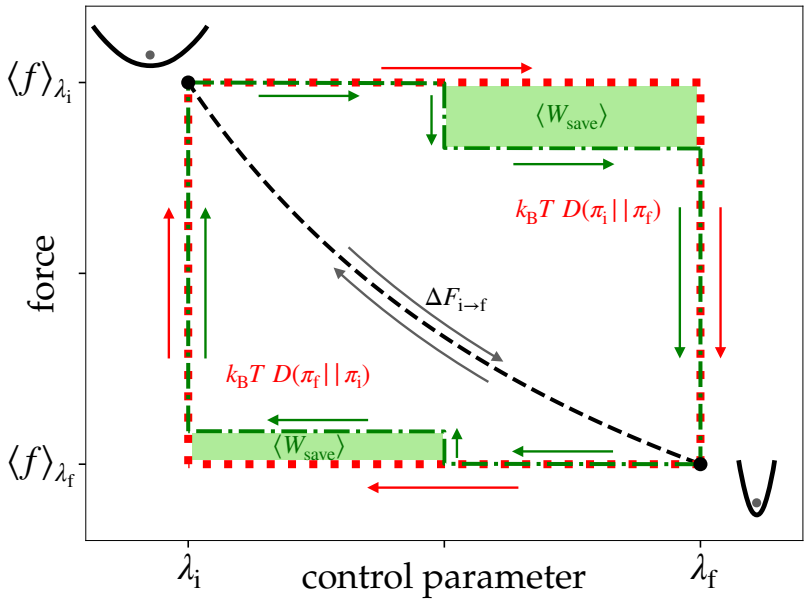

Fig 7.2. Thermodynamic cycle in the force vs. control parameter plane for the breathing harmonic trap driven by instantaneous (red dotted), STEP (green dash-dotted), and quasistatic (black dashed) protocols. Arrows denote protocol direction for transitions between open (λ_i) and closed (λ_f) states, shown schematically. The area under each curve gives the average work done by the respective protocol, the area under the quasistatic curve is the free-energy difference $\Delta F_{i\to f} = F_f - F_i$, the area between the instantaneous (dotted) and quasistatic (dashed) curves is the relative entropy (e.g., $\langle W \rangle_{\lambda_i} - \Delta F_{i\to f} = k_B T D(\pi_i || \pi_f)$), and the area between the STEP (dash-dotted) and instantaneous (dotted) curves is the saved work $\langle W_{\rm save} \rangle$ (shaded rectangles). Control-parameter endpoints satisfy $\lambda_i/\lambda_f = 1/2$, with duration $\Delta t/\tau = 2/5$ for fastest relaxation time $\tau = 1/(2\beta D \lambda_f)$.

$\langle W_{\rm save}\rangle_\Lambda^{\rm des}/\langle W_{\rm save}\rangle_\Lambda^{\rm naive}$ in saved work by the STEP is

$$G_{\rm save}^{\rm STEP} \approx \frac{\max_{\boldsymbol{\lambda}}[P_{\rm save}^{\rm st}(\lambda)]}{\overline{P_{\rm save}^{\rm st}(\lambda)}} \ , \tag{7.13}$$

where an overbar denotes the spatial average $\overline{P_{\rm save}^{\rm st}(\lambda)} \equiv (\Delta\lambda)^{-1}\int_{\lambda_{\rm i}}^{\lambda_{\rm f}} {\rm d}\lambda\ P_{\rm save}^{\rm st}(\lambda)$, "naive" the constant-velocity protocol, and "des" a designed protocol. The gain from a STEP is greatest when the power savings $P_{\rm save}^{\rm st}(\lambda)$ is sharply peaked.

7.4 Interpolated Protocols

In order to design a protocol that performs well for any duration, the STEP (optimal for fast protocols) is combined with the minimum-dissipation protocol from linear-response theory (optimal for slow protocols) to create an interpolated protocol. The linear-response protocol is continuous and when driven by a single control parameter proceeds at velocity ${\rm d}\lambda/{\rm d}t \propto [\zeta(\lambda)]^{-1/2}$, where $\zeta(\lambda)$ is the generalized friction coefficient.[125] For the interpolated protocol, the shape of the protocol from linear-response theory is maintained (i.e., ${\rm d}\lambda/{\rm d}t \propto [\zeta(\lambda)]^{-1/2}$) but with added initial jump $(\lambda^{\rm STEP}-\lambda_{\rm i})/(1+\Delta t/\tau)^\alpha$ and final jump $(\lambda_{\rm f}-\lambda^{\rm STEP})/(1+\Delta t/\tau)^\alpha$, where the constant α controls the crossover from slow to fast approximations. For the simple systems considered in this chapter it was empirically determined that $\alpha = 1$ performs relatively well.

Figure 7.3 shows the improvement from designed protocols relative to naive (constant-velocity) for the model system of a breathing harmonic trap. The difference between naive and designed work (Fig. 7.3a) shows the expected asymptotic behavior in the short- and long-duration limits: scaling as Δt (slope of one) for small $\Delta t/\tau$ and $(\Delta t)^{-1}$ (slope of negative one) for large $\Delta t/\tau$. Both the fast and slow designed protocols perform worse than naive (the difference is negative) for large and small $\Delta t/\tau$, respectively. The fast-protocol approximation (7.7) breaks down for long duration because the conjugate-force relaxation rate decreases as the system approaches equilibrium at $\boldsymbol{\lambda}$, whereas (7.7) assumes a constant relaxation time. However, the interpolated protocol performs well for any duration, and the largest work saved compared to naive is for intermediate duration. The gain $G_{\rm save}$ quantifies the percent increase in saved work from designed protocols relative to naive, where a gain greater than one indicates the designed does less work than the naive. For this system, the largest gain in saved work occurs in the fast limit (small $\Delta t/\tau$) for the STEP, interpolated, and exact optimal protocols.

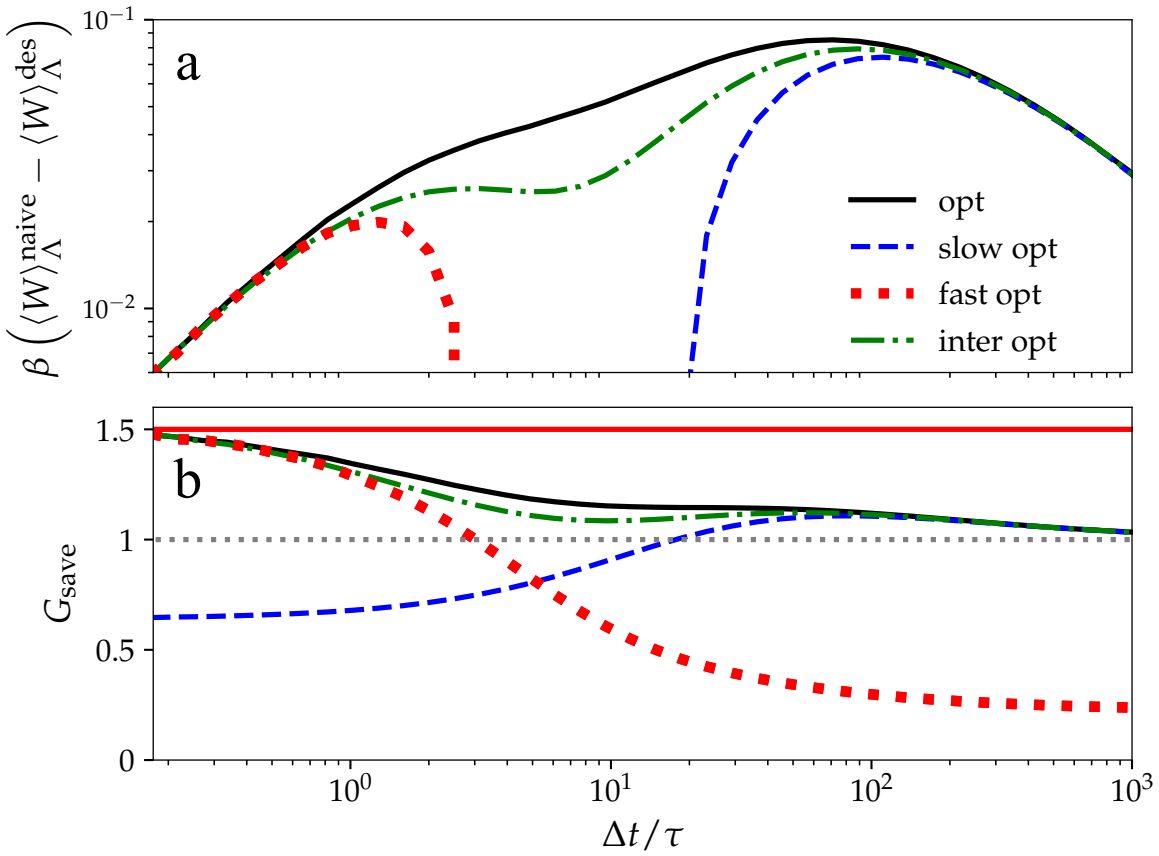

Fig 7.3. Benefit in the breathing harmonic trap from designed protocols relative to the naive (constant-velocity) protocol, as a function of the duration Δt scaled by the fastest integral relaxation time τ. The different designed ("des") protocols include the exact optimal[41] ("opt", solid black), linear-response optimized ("slow opt", dashed blue), STEP ("fast opt", red dots), and interpolated optimal protocol ("inter opt", dash-dotted green). (a) Difference between the work done by the naive (constant-velocity) and designed protocols. (b) Gain $G_{\rm save} \equiv \langle W_{\rm save}\rangle_\Lambda^{\rm des}/\langle W_{\rm save}\rangle_\Lambda^{\rm naive}$ in saved work. Solid red line in (b) denotes the short-duration limit (7.13). Control-parameter endpoints satisfy $\lambda_{\rm i}/\lambda_{\rm f} = 16$, and the interpolated protocol uses $\alpha = 1$ and fastest integral relaxation time $\tau = 1/(2\beta D\lambda_{\rm i})$[81].

7.5 Multiparameter Control

Optimization of multiparameter control protocols has seen a recent surge in interest, primarily driven by possible improvements to nonequilibrium free-energy estimates in fast-switching simulations.[187,188] Previous calculations of minimum-dissipation protocols which observed jumps were limited to one-parameter optimization. A significant advantage of the present approximation is that it permits simple multiparameter control-protocol optimization. Equation (7.11) implies that for multiparameter control the STEP consists of jumps to and from the control-parameter point $\boldsymbol{\lambda}^{\mathrm{STEP}}$.

To illustrate, consider a nine-spin Ising model with frustrated boundary conditions (Fig. 7.4).[76,189] There are two control parameters: magnetic fields $\boldsymbol{h} = (h_{\mathrm{b}}, h_{\mathrm{g}})$ applied to the mid-edge spins (Fig. 7.4a) which initially hold the system in the spin-down state and reverse during the protocol, driving the system to invert its magnetization. Appendix C.4 gives model details.

The power saving (7.12) vanishes at initial and final control-parameter values, respectively corresponding to zero relaxation rate and zero final jump size (Fig. 7.4b). By jumping past control-parameter regions with small power saving, the STEP outperforms the naive protocol for short duration, as quantified by the difference between naive and designed work (Fig. 7.4c) and the gain in saved work (Fig. 7.4d). Indeed, for short duration the STEP more than doubles the work saved by the naive protocol (i.e., has gain greater than two).

7.6 Discussion

I have developed an approximation for work in the fast-protocol limit (7.7) that permits straightforward optimization (7.11) simply from the initial force-relaxation rate (IFRR), Eq. (7.5b). It is shown that jumps are a universal feature of minimum-dissipation protocols in this fast limit, which is illustrated with several model systems under single- (Fig. 7.1) or multiparameter control (Fig. 7.4). Jumps minimize dissipation for fast protocols because the relaxation rate is approximately constant, with no diminishing returns from spending the entire duration at a single control-parameter value. Therefore, the STEP jumps between the fixed control-parameter endpoints to spend the entire duration at the control-parameter value that maximizes the product of the IFRR and the subsequent jump size (7.12). This breaks down for slow protocols since with sufficient time at a single control-parameter value, the relaxation rate decreases over time; indeed, in the slow limit the minimum-dissipation protocol is continuous.[125] These two seemingly disparate limits are combined with a simple interpolation scheme, producing protocols that perform well for any duration (Fig. 7.3).

Since the present derivation is valid for overdamped and Master-equation dynamics, it would be interesting to apply a similar approach to study the optimal control of under-

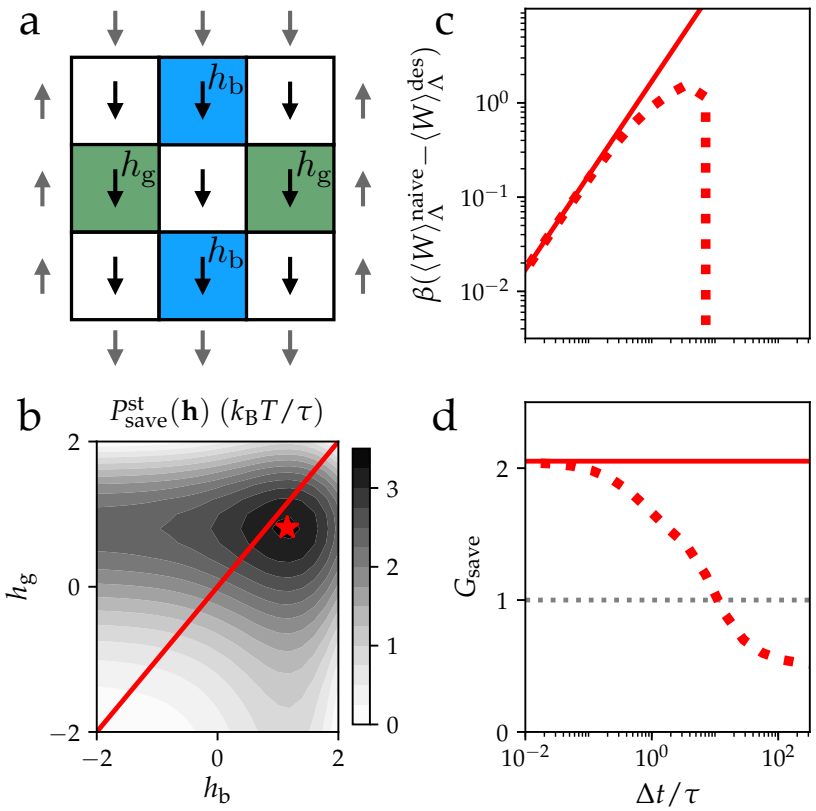

Fig 7.4. a) Nine-spin ferromagnetic Ising model (internal black spins) with fixed boundary conditions (external gray spins). The multiparameter control parameter is two external magnetic fields, $h_{\rm b}$ (blue) applied to horizontal-edge spins and $h_{\rm g}$ (green) applied to vertical-edge spins. b) Short-time power savings (7.12) as function of control parameters ($h_{\rm b}$,$h_{\rm g}$). Red line: naive protocol; red star: $\boldsymbol{h}^{\rm STEP}$ (7.11). c) Work difference between designed and naive protocols (dotted red), and its short-duration approximation (7.7) (solid red). d) Gain $G_{\rm save} \equiv \langle W_{\rm save}\rangle_\Lambda^{\rm des}/\langle W_{\rm save}\rangle_\Lambda^{\rm naive}$ in saved work for multiparameter STEP relative to naive (dotted red), and its short-duration limit (7.13) (solid red). Control-parameter endpoints are $\boldsymbol{h}_{\rm i} = (-2,-2)$ and $\boldsymbol{h}_{\rm f} = (2,2)$, with duration Δt and fastest relaxation time $\tau = N/k_{\rm flip}$, for $N = 9$ spins and single-spin flip attempt rate $k_{\rm flip}$.

damped Langevin dynamics. For quadratic trapping potentials, it has been shown that the optimal protocol has not only jumps but also delta-function peaks in the control parameters at the start and end of the protocol; therefore, it would be interesting to see if the short-time approximation can be generalized to underdamped dynamics.[44]

One important application of minimum-dissipation protocols is to free-energy estimation, which aids the design of novel ligands for targeted protein binding.[138–144] Quite generally, the accuracy of free-energy estimates decreases with increasing dissipation.[81,146,147,155,167,190] Based on the results of Ref. 41, jump protocols have been used to reduce dissipation and improve free-energy estimates,[167] but previously it was unknown whether jumps would always reduce dissipation in these more complex systems, and there was no simple procedure to find the optimal jump size. The present formalism demonstrates that jumps are a general feature and gives a simple optimization procedure applicable to multiparameter control. This makes protocol optimization tractable for a considerably expanded range of systems.

Although this chapter focused on systems with known equations of motion, the IFRR (7.5b) and short-time power savings (7.12) are easily estimated without detailed dynamical information: the system only needs to be equilibrated at a single control-parameter value; the protocol can be very short; the average converges with few samples; and the STEP is found using standard optimization techniques applied to (7.12). The STEP can thus be computed relatively inexpensively, easing determination of minimum-dissipation protocols in rapidly driven complex chemical and biological systems. This opens the door to improve the energetic efficiency in thermodynamic computing[39,191] and the accuracy of nonequilibrium free-energy estimates in simulations and single-molecule experiments.[80,81,147,190]

Chapter 8

Strong-trap approximation

Quadratic trapping potentials are widely used to experimentally probe biopolymers, molecular machines, and drive transitions in steered molecular-dynamics simulations. Approximating energy landscapes as locally quadratic, multidimensional trapping protocols that minimize dissipation are designed. The designed protocols are easily solvable and applicable to a wide range of systems. The approximation does not rely on either fast or slow limits and is valid for any duration provided the trapping potential is sufficiently strong. The utility of the designed protocols is demonstrated with a simple model of a periodically driven rotary motor. These results elucidate principles of effective single-molecule manipulation and efficient nonequilibrium free-energy estimation. This chapter is adapted from the published version in Ref. 43.

In this chapter I consider two types of *protocols*: *constrained-final-distribution* (CFD) protocols and *constrained-final-control-parameter* (CFCP) protocols. CFD protocols assume complete control over the dynamics and drive the system to a specified final probability distribution, guaranteeing that at any driving speed the system will reach its destination. This can be used to model rotary motors like ATP synthase by setting the final state to be identical to the initial but shifted by one period, resulting in one cycle of free-energy transduction in a specified duration.

CFCP protocols drive a finite set of control parameters to specified final control-parameter values. For such protocols, the system does not necessarily keep up with rapid changes in control parameters, and for fast driving the system state remains largely unchanged.[47] For nonequilibrium free-energy estimation, the free-energy change is estimated from work measurements between control-parameter endpoints, so CFCP protocols are the natural choice.

Within the strong-trap approximation, for equal initial and final covariance, the minimum-dissipation CFD protocols are given by explicit equations for the trap center (8.4a) and

stiffness (8.6) that linearly drive the mean between the specified endpoints while maintaining constant covariance. A second optimization (8.10) is performed to achieve CFCP minimum-dissipation protocols. Since the designed CFD protocols can be solved analytically and calculating CFCP protocols only requires performing a minimization over the final mean and covariance (which in some cases is analytic (8.11)), these designed protocols are considerably simpler to determine than previous methods.[47,50,125] For a model rotary motor (Fig. 8.1), the designed protocol tightens the trap as it crosses energy barriers, achieving minimal entropy production (8.7) and maximum efficiency (8.9), provided the trap is sufficiently strong to confine the system within a single well (Fig. 8.2).

8.1 Minimum-Dissipation Quadratic Control

Consider the overdamped motion of a system with diffusivity D driven by a time-dependent potential $V_{\text{tot}}(\boldsymbol{r}, t)$, satisfying the Fokker-Planck equation (3.4). The total potential

$$V_{\text{tot}}(\boldsymbol{r}, t) = V_{\text{land}}(\boldsymbol{r}) + V_{\text{trap}}(\boldsymbol{r}, t) \tag{8.1}$$

is separated into a time-independent component V_{land} (the underlying energy landscape) and a quadratic trapping potential (2.1). For a strong trapping potential, the time-independent component can be expanded up to second order about the mean position $\boldsymbol{\mu}$

$$V_{\text{land}}(\boldsymbol{r}) \approx V_{\text{land}}(\boldsymbol{\mu}) + (\boldsymbol{r} - \boldsymbol{\mu})^\top \nabla V_{\text{land}}(\boldsymbol{\mu}) + \frac{1}{2}(\boldsymbol{r} - \boldsymbol{\mu})^\top \nabla\nabla^\top V_{\text{land}}(\boldsymbol{\mu})(\boldsymbol{r} - \boldsymbol{\mu}) \ , \tag{8.2}$$

with $\nabla\nabla^\top$ the Hessian matrix. Under these assumptions, the probability distribution can be approximated as Gaussian, $p_t(\boldsymbol{r}) \approx \mathcal{N}(\boldsymbol{\mu}_t, \Sigma_t)$, with $\boldsymbol{\mu}_t$ the average position vector and Σ_t the covariance matrix at time t.

Since the probability is approximately Gaussian, the known exact solution for the minimum-dissipation protocol presented in section 4.1.1 is applied: the entropy production is bounded by the squared Wasserstein distance (4.6),[42,123] and is minimized by a linearly varying mean and covariance satisfy (4.7a) and (4.7b) respectively.

The minimum-dissipation protocol is expressed in terms of the trap center and stiffness by solving the dynamical equations of motion (3.4) for the time-dependent mean and covariance

$$\frac{1}{\beta D}\frac{\mathrm{d}\mu_t}{\mathrm{d}t} = K_t(\boldsymbol{r}_t^{\mathrm{c}} - \boldsymbol{\mu}_t) - \nabla V_{\text{land}}(\boldsymbol{\mu}_t) \tag{8.3a}$$

$$\frac{1}{\beta D}\frac{\mathrm{d}\Sigma_t}{\mathrm{d}t} = 2\beta^{-1} - \left[K_t + \nabla\nabla^\top V_{\text{land}}(\boldsymbol{\mu}_t)\right]\Sigma_t - \Sigma_t\left[K_t + \nabla\nabla^\top V_{\text{land}}(\boldsymbol{\mu}_t)\right] \tag{8.3b}$$

and substituting their optima (4.7a) and (4.7b). The trap center and stiffness must respectively satisfy (for a detailed derivation in the absence of an energy landscape see Ref. 42)

$$\boldsymbol{r}_t^{\mathrm{c}} = \boldsymbol{\mu}_t + K_t^{-1}\left[\frac{\Delta\boldsymbol{\mu}}{\beta D\Delta t} + \nabla V_{\mathrm{land}}(\boldsymbol{\mu}_t)\right] , \tag{8.4a}$$

$$K_t = \frac{1}{\beta}\Sigma_t^{-1} - \frac{1}{\beta D}\int_0^\infty \mathrm{d}\nu\; e^{-\nu\Sigma_t}\frac{\mathrm{d}\Sigma_t}{\mathrm{d}t}e^{-\nu\Sigma_t} - \nabla\nabla^\top V_{\mathrm{land}}(\boldsymbol{\mu}_t) , \tag{8.4b}$$

where μ_t is given by (4.7a), and Σ_t by (4.7b). If Σ is diagonal, then Σ_t is given by (4.8), the integral in (8.4b) can be evaluated, and the trap stiffness obeys

$$K_t = \nabla\nabla^\top V_{\mathrm{land}}(\boldsymbol{\mu}_t) + \left(\frac{1}{\beta}I - \frac{\Delta\Sigma^{\frac{1}{2}}}{2\beta D\Delta t}\right)\Sigma_t^{-1}. \tag{8.5}$$

These explicit protocol equations (8.4) are considerably easier to compute than previous methods for determining minimum-dissipation protocols for CFDs, which require solving differential equations or inverting the Fokker-Planck equation.[39,50] By constraining the final covariance matrix after one period (during which the mean completes one rotation) to equal the initial, the driving is periodic: the first two moments are periodic in time. Therefore, to minimize dissipation of a periodic system the covariance remains unchanged throughout the protocol (4.7b). This is achieved when the effective stiffness is constant, i.e.,

$$K_t = K_0 + \nabla\nabla^\top V_{\mathrm{land}}(\boldsymbol{\mu}_0) - \nabla\nabla^\top V_{\mathrm{land}}(\boldsymbol{\mu}_t) . \tag{8.6}$$

If in each rotation the mean travels a distance $\Delta\boldsymbol{\mu}_{\mathrm{rot}}$ in time Δt_{rot}, the resultant entropy production is

$$\Delta S_{\mathrm{prod}} = \frac{\Delta\boldsymbol{\mu}_{\mathrm{rot}}^2}{D\Delta t_{\mathrm{rot}}} , \tag{8.7}$$

that of an overdamped system moving at constant velocity against viscous Stokes drag; i.e., the minimum-dissipation protocol has perfect *Stokes efficiency*.[192]

For a machine transducing free energy ΔF_{neq} (i.e., converting input work into output free energy) between the initial and final distributions with equal covariance, the efficiency is the ratio of output free energy to input work,

$$\eta \equiv \frac{\beta\Delta F_{\mathrm{neq}}}{\beta\Delta F_{\mathrm{neq}} + \Delta S_{\mathrm{prod}}} , \tag{8.8}$$

with the minimum-dissipation protocol achieving the upper bound,

$$\eta_{\max} = \left[1 + \frac{(\Delta\boldsymbol{\mu}_{\rm rot})^2}{\beta D \Delta t_{\rm rot} \Delta F_{\rm neq}}\right]^{-1} . \tag{8.9}$$

Since the entropy production is independent of the free-energy change, a system that travels the same distance but transduces more free energy is more efficient.

8.2 Free-Energy Estimation

Free-energy differences between two equilibrium states of a system can be estimated from nonequilibrium work measurements using the Jarzynski equality or the Crooks fluctuation theorem (chapter 5).[25,26,36] The Jarzynski estimator of the free-energy difference $\Delta F_{\rm eq} \equiv F_{\rm eq}[\boldsymbol{\lambda}_{\Delta t}, K_{\Delta t}] - F_{\rm eq}[\boldsymbol{\lambda}_0, K_0]$ between equilibrium distributions corresponding to constrained initial and final control parameters is (5.2). In general, the statistical error of the free-energy estimate based on Jarzynski's equality increases with dissipation. The connection between statistical error and dissipation is clearest when dissipation is small, where the expected bias and variance are approximately (5.5a) and (5.5b) respectively.[81,146] If dissipation is small, minimizing work also minimizes the bias and variance of free energies estimated from Jarzynski's equality. Similar connections can be made for other free-energy estimators such as Bennett's acceptance ratio (5.3).[81,152,153]

The average work (3.23) for the minimum-dissipation protocol is

$$\begin{aligned}\langle W \rangle =& \frac{1}{2}\mathrm{Tr}\left\{K\left[\Sigma + (\boldsymbol{\mu}-\boldsymbol{\lambda})(\boldsymbol{\mu}-\boldsymbol{\lambda})^\top\right]\right\}_0^{\Delta t} + V_{\rm land}(\boldsymbol{\mu})\big|_0^{\Delta t} + \frac{1}{2}\mathrm{Tr}\left[\nabla\nabla^\top V_{\rm land}(\boldsymbol{\mu})\Sigma\right]_0^{\Delta t} \\ &+ \frac{1}{\beta}\Delta S_{\rm prod}^{\rm min} ,\end{aligned} \tag{8.10}$$

with Tr the trace and $\Delta S_{\rm prod}^{\rm min}$ the lower bound in (4.6). To find the protocol that minimizes work for CFCPs (8.10) is minimized with respect to the final mean $\mu_{\Delta t}$ and covariance $\Sigma_{\Delta t}$, for fixed final trap center $\boldsymbol{\lambda}_{\Delta t}$ and stiffness $K_{\Delta t}$.

For equal initial and final covariance and a flat energy landscape, the final mean is

$$\boldsymbol{\mu}_{\Delta t} = \boldsymbol{\mu}_0 + \left(\frac{2K^{-1}}{\beta D \Delta t} + I\right)^{-1} (\boldsymbol{\lambda}_{\Delta t} - \boldsymbol{\mu}_0) . \tag{8.11}$$

In some more general cases (e.g., energy landscapes represented by low-order polynomials), (8.10) can also be minimized analytically, and in general can be solved numerically with relative ease. Performing this minimization is a considerably simpler task than finding

the minimum-dissipation protocols based on thermodynamic-geometry frameworks, which typically require calculating metric tensors and solving geodesic equations.[77,82] Another benefit of the present method is that it does not rely on either slow-protocol[125] or fast-protocol[47] approximations and is valid at any duration provided the trapping potential is sufficiently strong.

8.3 Rotary Motor

The applicability of the approximation presented within this chapter is demonstrated with a model of a rotary motor inspired by ATP synthase (chapter 2). Consider a one-dimensional periodic energy landscape (2.3) (Fig. 8.1). The protocol is periodic with equal initial and final variances, $\Sigma_0 = \Sigma_{\Delta t}$, starting with the mean position at the center of a well, $\mu_0 = 0$, and terminating after three barrier crossings so that $\mu_{\Delta t} = 3\Delta x_\mathrm{m}$. For the model's periodic energy landscape (2.3) and initial and final means, substituting the optimal (linearly varying) mean (4.7a) and variance (4.8) into (8.4a) and (8.6) respectively, gives the minimum-dissipation protocol

$$r_t^\mathrm{c} = \frac{1}{k_t}\left(\frac{3\Delta x_\mathrm{m}}{\beta D \Delta t} + \frac{\Delta E}{\Delta x_\mathrm{m}} + \frac{\pi E_\mathrm{b}}{\Delta x_\mathrm{m}} \sin\frac{6\pi}{\Delta t}t\right) + \frac{3\Delta x_\mathrm{m}}{\Delta t}t \ , \tag{8.12a}$$

$$k_t = k_0 + \frac{2\pi^2 E_\mathrm{b}}{\Delta x_\mathrm{m}^2} - \frac{2\pi^2 E_\mathrm{b}}{\Delta x_\mathrm{m}^2}\cos\frac{6\pi}{\Delta t}t \ . \tag{8.12b}$$

Figure 8.1 shows the designed intermediate-duration protocol for driving the system over three barriers, numerically estimated from Langevin dynamics integrated with the Euler–Maruyama method[193] with sufficiently small time steps and numerous samples such that numerical inaccuracies are negligible (Appendix A). To maintain constant variance, the designed protocol tightens the trap as it crosses the barriers; to linearly drive the mean between the two wells, the trap center initially jumps ahead of the mean position μ_0, remaining ahead throughout the protocol. For a Gaussian distribution, the 9%, 25%, 75%, and 91% quantiles are evenly spaced, consistent with the linear translation of the quantiles between the two wells, shown in Fig. 8.1 for $k_0 = 2E_\mathrm{b}/x_\mathrm{m}^2$. For a weak trap ($k_0 = E_\mathrm{b}/(2x_\mathrm{m}^2)$), the quantiles are not evenly spaced and exhibit significant deviations from linear temporal evolution, implying that the Gaussian approximation is no longer valid. The crossover from strong to weak trap occurs when $k_0 \sim E_\mathrm{b}/x_\mathrm{m}^2$, since a weaker trap ($k_0 \lesssim E_\mathrm{b}/x_\mathrm{m}^2$) is not sufficient to confine the system within a single well and the distribution can become bimodal, resulting in widely separated quantiles as the system crosses the barriers (Fig. 8.1).

The quadratic approximation is accurate when the initial stiffness is large ($k_0 \gg E_\mathrm{b}/x_\mathrm{m}^2$). When this condition holds, the entropy production and efficiency are well approximated by

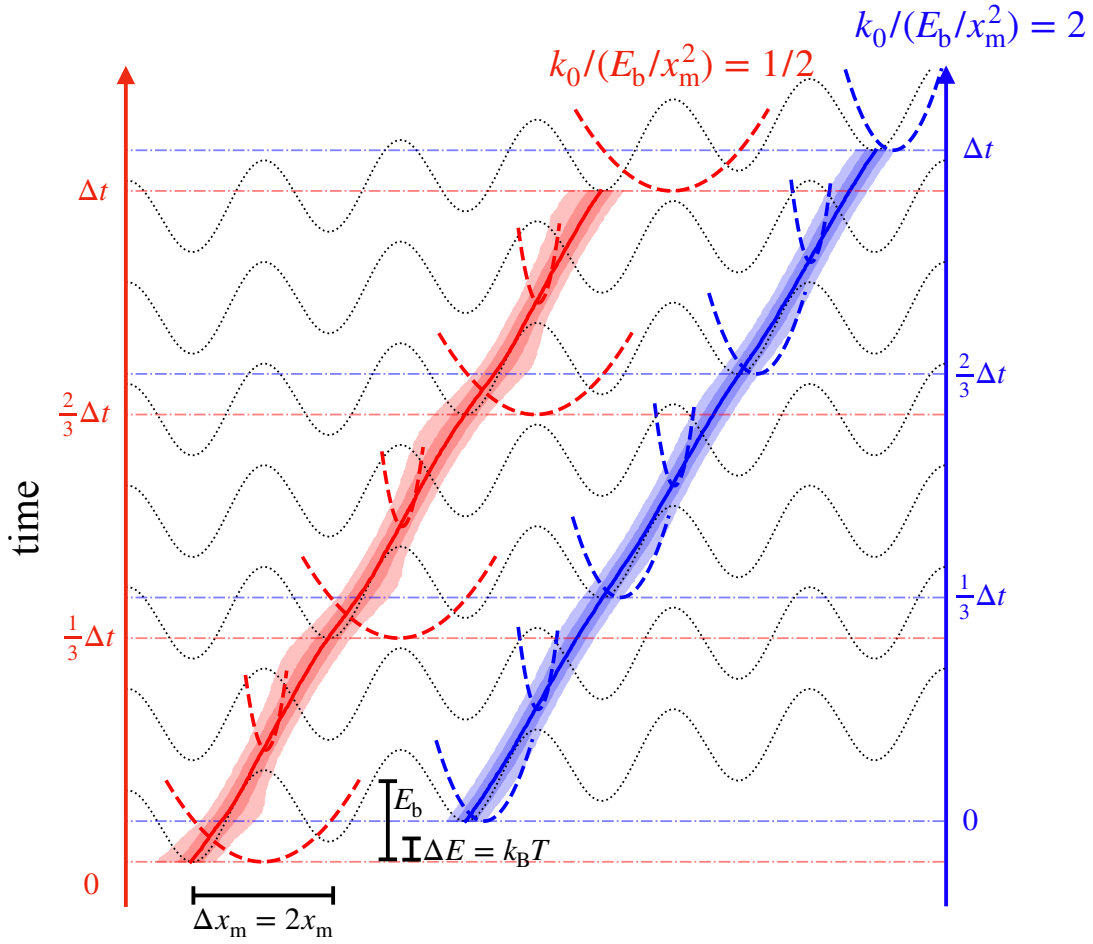

Fig 8.1. Designed protocol for a model rotary motor. Time-dependent protocol for a weak initial stiffness $k_0/(E_b/x_m^2) = 1/2$ (red, left) and intermediate initial stiffness $k_0/(E_b/x_m^2) = 2$ (blue, right) depicting the static potential (dotted/gray), trap potential (dashed), median position (solid), and 9%, 25%, 75%, and 91% quantiles (shaded). The two protocols are offset vertically and horizontally for clarity. The energy offset is $\Delta E = \beta^{-1}$, the barrier height is $E_b = 4\beta^{-1}$, and the protocol duration is $\Delta t = \tau_D$ for diffusion time $\tau_D \equiv \Delta x_m^2/D$ between adjacent wells.

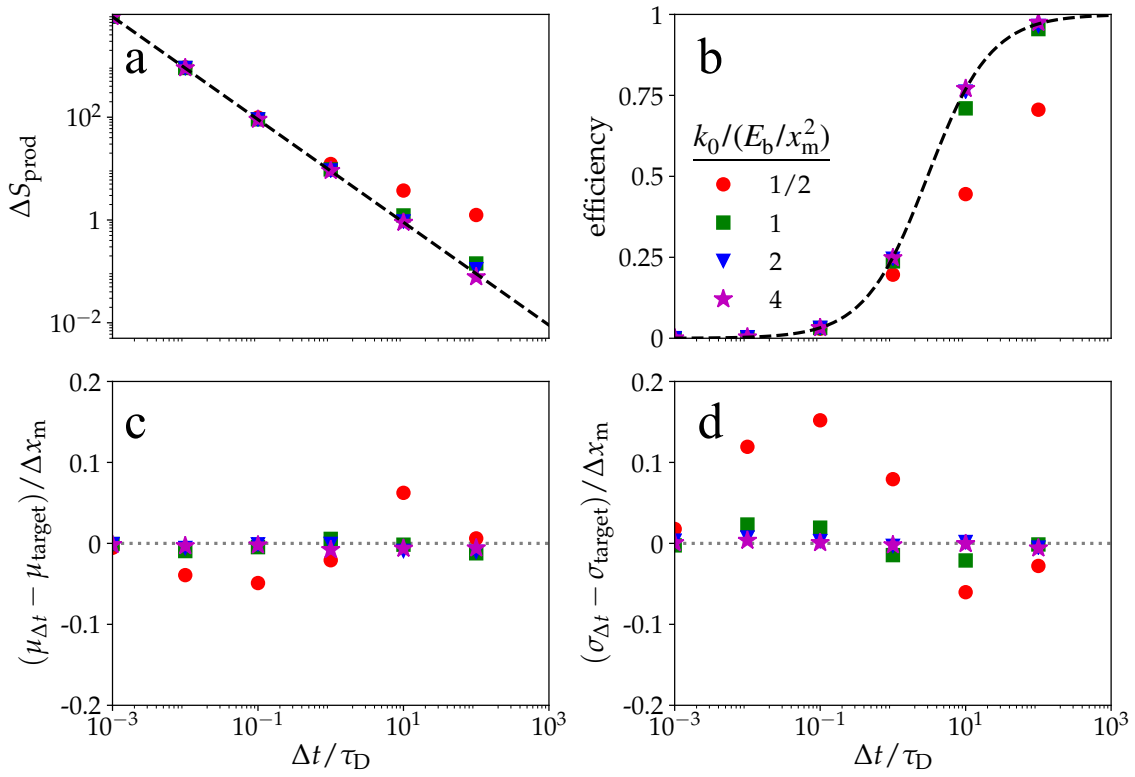

Fig 8.2. Performance of model rotary motor. (a) Entropy production, (b) efficiency, (c) deviation of the final mean position from the target, and (d) deviation of the final standard deviation from the target. Different colors/markers represent different initial stiffnesses k_0. Black dashed curves in (a) and (b): strong-trap approximations (8.7) and (8.9), respectively. The energy offset is $\Delta E = \beta^{-1}$ and the barrier height is $E_\mathrm{b} = 4\beta^{-1}$. Error bars representing bootstrap-resampled 95% confidence intervals are smaller than the markers.

(8.7) and (8.9) at any protocol duration (Fig. 8.2 a/b). Additionally, for a fast protocol whose duration is shorter than the diffusion time between adjacent wells ($\Delta t \ll \tau_{\mathrm{D}} \equiv \Delta x_{\mathrm{m}}^2/D$), the entropy production and efficiency agree with (8.7) and (8.9) even for a relatively weak initial stiffness. Large forces are required to rapidly drive the system, which can only be achieved by the trap potential (since the energy landscape is not dynamically controlled), resulting in the dominant contribution to the force arising from the trap potential. Therefore, the approximation is valid when either the protocol duration is short ($\Delta t \ll \tau_{\mathrm{D}}$) or the initial stiffness is large ($k_0 \gg E_{\mathrm{b}}/x_{\mathrm{m}}^2$).

Despite the quadratic approximation breaking down when both $\Delta t \gtrsim \tau_{\mathrm{D}}$ and $k_0 \lesssim E_{\mathrm{b}}/x_{\mathrm{m}}^2$, the final position's mean and standard deviation remain within 20% of their respective targets, relative to the distance between the wells (Fig. 8.2 c/d). Even when the approximations break down, the designed protocols successfully drive the system to the final desired distribution.

8.4 Discussion

By approximating static energy landscapes as locally quadratic, minimum-dissipation protocols for quadratic trapping potentials have been derived. This approximation does not rely on either slow or fast limits and therefore offers a complementary result to previous work on designing minimum-dissipation protocols in the fast and slow limits.[47,125] Designed protocols based on the present approximation are considerably simpler than previous methods for determining the minimum-dissipation protocols, which require estimating correlation functions and solving geodesic equations. The trap center linearly drives the mean between the specified endpoints (8.4a); if the initial and final covariances are equal, then the stiffness adjusts to maintain constant covariance throughout the protocol (8.6).

The applicability of the approximation is demonstrated with a simple model of a driven rotary motor (Fig. 8.2). When either the initial stiffness is large ($k_0 \gg E_{\mathrm{b}}/x_{\mathrm{m}}^2$) or the duration is short ($\Delta t \ll \tau_{\mathrm{D}}$), the motor achieves the maximum efficiency (8.9). When the initial stiffness is small ($k_0 \lesssim E_{\mathrm{b}}/x_{\mathrm{m}}^2$) and the duration is large ($\Delta t \gtrsim \tau_{\mathrm{D}}$) the motor achieves significantly lower efficiency (difference in efficiency of ~ 0.25) but the designed protocols still drive the system to within 20% of the target endpoints relative to the inter-well distance Δx_{m}.

The formalism presented in this chapter gives insight into the design principles of efficient motors. Achieving maximum efficiency requires full control of the system, which in general would require an infinite number of control parameters; however, full control of Gaussian probability distributions can be achieved with a finite number of parameters. Within the strong-trap approximation, for a d-dimensional system the number of control

parameters required for an arbitrary energy landscape is $d(d+3)/2$: d trap center components (controlling the means) and $d(d+1)/2$ stiffness matrix components (controlling the covariances).

I emphasize that the intermediate states remaining Gaussian in the optimal-transport process is the result of an optimization over all possible distributions connecting Gaussian end-states and not an imposed constraint on the intermediate distributions. This is in contrast to parametric methods for determining the minimum-dissipation protocols, where the intermediate states are constrained to those accessible by the small number of control parameters.[34,125] In general, the minimum-dissipation protocols determined from parametric control will coincide with optimal transport when there are sufficiently many control parameters to access the intermediate distributions of the optimal-transport process; e.g., $d(d+3)/2$ control parameters for a d-dimensional system with a flat energy landscape and a quadratic trapping potential. Otherwise, the full control afforded by the optimal-transport process will achieve less dissipation.

Several of the results presented in this chapter are directly applicable to physical systems. Single-control-parameter (typically the trap center) designed pulling protocols for unfolding DNA hairpins can reduce dissipation.[80] My recent theoretical study[82] (Chapter 9) suggests that dissipation in DNA-hairpin experiments can be significantly further reduced by adding one additional control parameter (trap stiffness), but further control (beyond trap center and stiffness) would do very little to reduce dissipation. Within the present framework this is easily understood. Control over the trap center drives the system over the energy barrier between the folded and unfolded state, but cannot prevent the increase in variance as it crosses the barrier. By tightening the trap as it traverses the barrier, the system's variance remains constant and the barrier is effectively eliminated. If the trap is reasonably stiff, then the distribution is approximately Gaussian, and two control parameters are sufficient for full control of this one-dimensional system. Application of the strong-trap approximation to a barrier-crossing model for parameters relevant to DNA hairpin experiments is given in Chapter 9.

The minimum-dissipation protocols described in the *Free-energy estimation* section can be directly applied to improve estimates of free-energy differences. In steered molecular-dynamics simulations, strong-trap approximations are commonly employed when estimating free-energy differences;[194,195] therefore, the method presented in this chapter is well situated to improve these estimates. More generally, several enhanced-sampling techniques for free-energy estimation add quadratic potentials to smooth potential-energy surfaces[196,197] or trap intermediate states in umbrella sampling.[151] There could be connections between minimum-dissipation protocols and the improved performance from smoothing potential-energy surfaces and optimally spacing intermediate states.[147–151,198,199]

A benefit of the present formalism is that it allows specification of the final distribution by its mean and covariance while using a finite number of control parameters. Previous

methods that specified the final distribution using optimal-transport theory required full control over the potential, in principle requiring infinite control parameters. General designs for parametric control typically constrain final control-parameter values but do not actually achieve a specific target distribution. Being able to specify the final distribution is particularly useful for modeling periodic motors like ATP synthase. Fixing equal initial and final covariance periodically drives the motor with a high degree of precision (Fig. 8.2 c/d) and gives insight into the maximum efficiency of such driving.

Finally, the ease of determining multidimensional designed protocols opens up the possibility to explore a host of new systems, from coupled transport motors pulling cargo[200] to steered molecular-dynamics simulations of complex condensed-matter systems.

Chapter 9

Barrier Crossing

Modern advances in single-molecule biophysics make possible the precise spatial and temporal control of biological systems. Optical tweezers can be used to probe the conformational and energetic properties of biopolymers (DNA and RNA molecules)[8–13] and molecular machines (ATP synthase,[14–16] kinesin,[17–20] and myosin[21–24]). Additionally, computer simulations such as steered molecular dynamics have the freedom to fully control the molecular and trapping potentials. Despite the relative freedom of control, experiments and simulations rarely exploit the possibility of optimized control protocols, and the few that do are generally limited to optimization of a single control parameter.[167,188,201] Using the methods for determining minimum-dissipation protocols for slow (Chapter 4), fast (Chapter 7), and strong (Chapter 8) control, I design minimum-dissipation protocols for driven barrier crossing under two-parameter control of trap center and stiffness.

Two-parameter control allows specification of both the time-dependent mean and variance of the position distribution, and results in qualitatively distinct designed protocols (Fig. 9.5). Such a designed protocol has jumps at the start and end that decrease in size as the duration increases, and slows down and tightens as it crosses the barrier, approximately linearly driving the mean and maintaining roughly constant variance throughout the protocol. For any duration, the designed protocols significantly improve performance in terms of both dissipation and flux compared to naive and one-parameter control (Fig. 9.4). This chapter is adapted from the article published in Ref. 82.

9.1 Thermodynamics

Consider a model system relevant to DNA-hairpin experiments: a Brownian bead driven by a time-dependent quadratic trapping potential with center and stiffness modulated by the

focus and intensity of the laser. This model is also typical of steered molecular-dynamics simulations, which use a time-dependent quadratic potential to drive reactions.[188] The total potential $V_{\text{tot}} = V_{\text{land}} + V_{\text{trap}}$ is the sum of the static hairpin potential (2.2) and time-dependent trap potential (2.1) (shown schematically in Fig. 9.5).

The total work (4.9) can be separated into two components, $W = W_{\text{c}} + W_{\text{s}}$, one for each control parameter. The trap-center component

$$\langle W_{\text{c}} \rangle_{\mathbf{\Lambda}} = \int_0^{\Delta t} \mathrm{d}t \; k(t) \left[x^{\text{c}}(t) - \langle x \rangle_{\mathbf{\Lambda}} \right] \frac{\mathrm{d}x^{\text{c}}(t)}{\mathrm{d}t} \tag{9.1}$$

is analogous to "force-distance" work. The stiffness component

$$\langle W_{\text{s}} \rangle_{\mathbf{\Lambda}} = \frac{1}{2} \int_0^{\Delta t} \mathrm{d}t \left\langle \left[x^{\text{c}}(t) - x \right]^2 \right\rangle_{\mathbf{\Lambda}} \frac{\mathrm{d}k(t)}{\mathrm{d}t} \tag{9.2}$$

resembles "pressure-volume" work, i.e., the stiffness controls the effective volume available to the system, and the variance contributes to an effective pressure resisting changes in trap stiffness.

9.2 Designed protocols

9.2.1 One-Parameter Control

For one-parameter control, in order to gain additional insight into minimum-dissipation protocols, an energy offset and sinusoidal oscillations are added to the double-well potential discussed in Chapter 2:

$$V_{\text{land}}(x) = \left[E_{\text{b}} + A \cos\left(\frac{2\pi x}{x_{\text{o}}} \right) \right] \left[\left(\frac{2x - \Delta x_{\text{m}}}{\Delta x_{\text{m}}} \right)^2 - 1 \right]^2 + \Delta E_{\text{m}} \left(\frac{x}{x_{\text{m}}} \right)^3 . \tag{9.3}$$

The barrier height is E_{b} (Fig. 9.1), the energy offset between the two minima at 0 and $\Delta x_{\text{m}} = 2x_{\text{m}}$ is ΔE_{m}, and the amplitude of the oscillations is A with wavelength x_{o} (Fig. 9.2).

Slow Limit

For a symmetric double-well potential with a trap stiffness comparable to the barrier height ($k \sim E_{\text{b}}/x_{\text{m}}^2$), the friction is strongly peaked at the center of the barrier (Fig. 9.1b). For stiffness significantly smaller ($k \ll E_{\text{b}}/x_{\text{m}}^2$) or larger ($k \gg E_{\text{b}}/x_{\text{m}}^2$) than the barrier height,

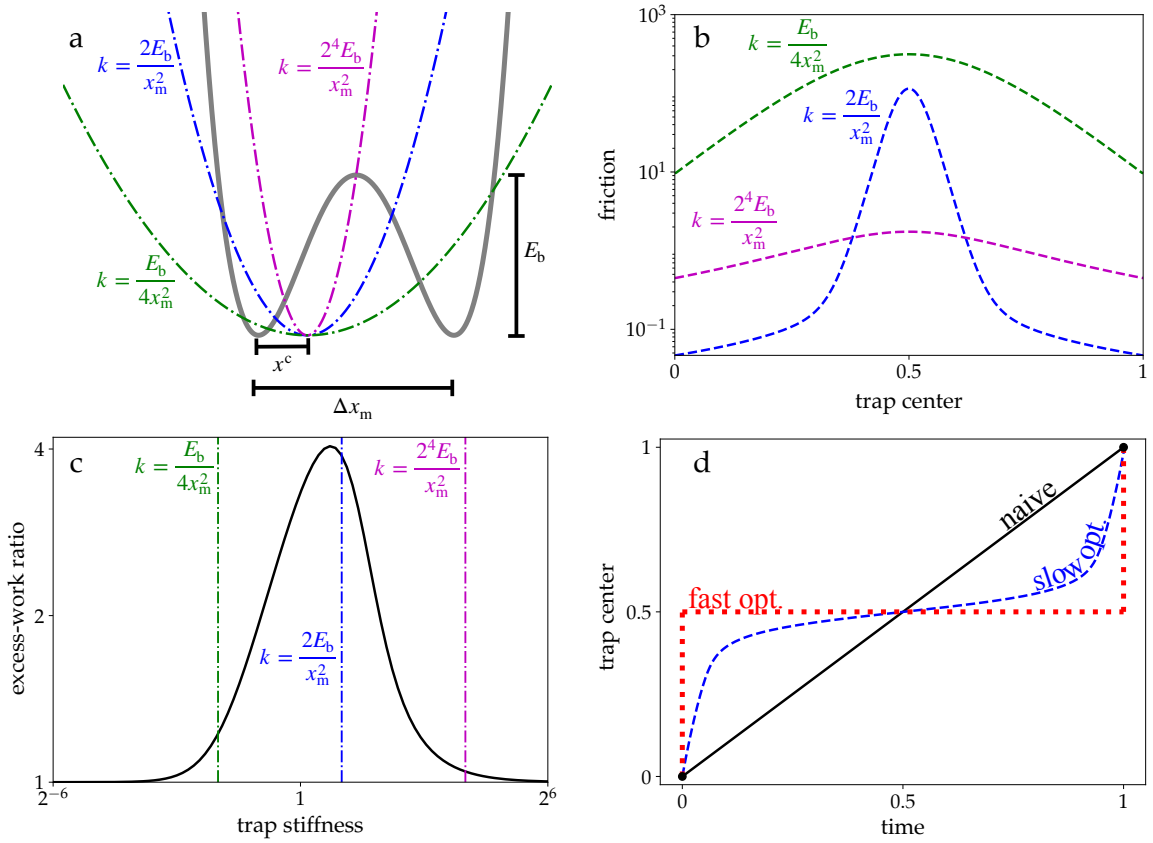

Fig 9.1. a) Double-well potential (2.2) (solid gray) with a barrier of height E_b separating minima at 0 and Δx_m. The trap potential (2.1) (dash-dotted) is centered at x^c. b) Friction (4.16) as a function of the trap center x^c. c) Excess-work ratio (4.19) as a function of trap stiffness. d) Designed protocols for trap stiffness $k = 2E_b/x_m^2$, with "naive" the linear (constant-velocity) protocol, "slow opt." the friction-optimized protocol (4.17), and "fast opt." the STEP (7.11). Throughout, the barrier height is $E_b = 8\beta^{-1}$, there is no energy offset $\Delta E_m = 0$ or oscillations $A = 0$, and trap stiffness is $k = E_b/(4x_m^2)$ (green), $2E_b/x_m^2$ (blue), or $2^4 E_b/x_m^2$ (purple).

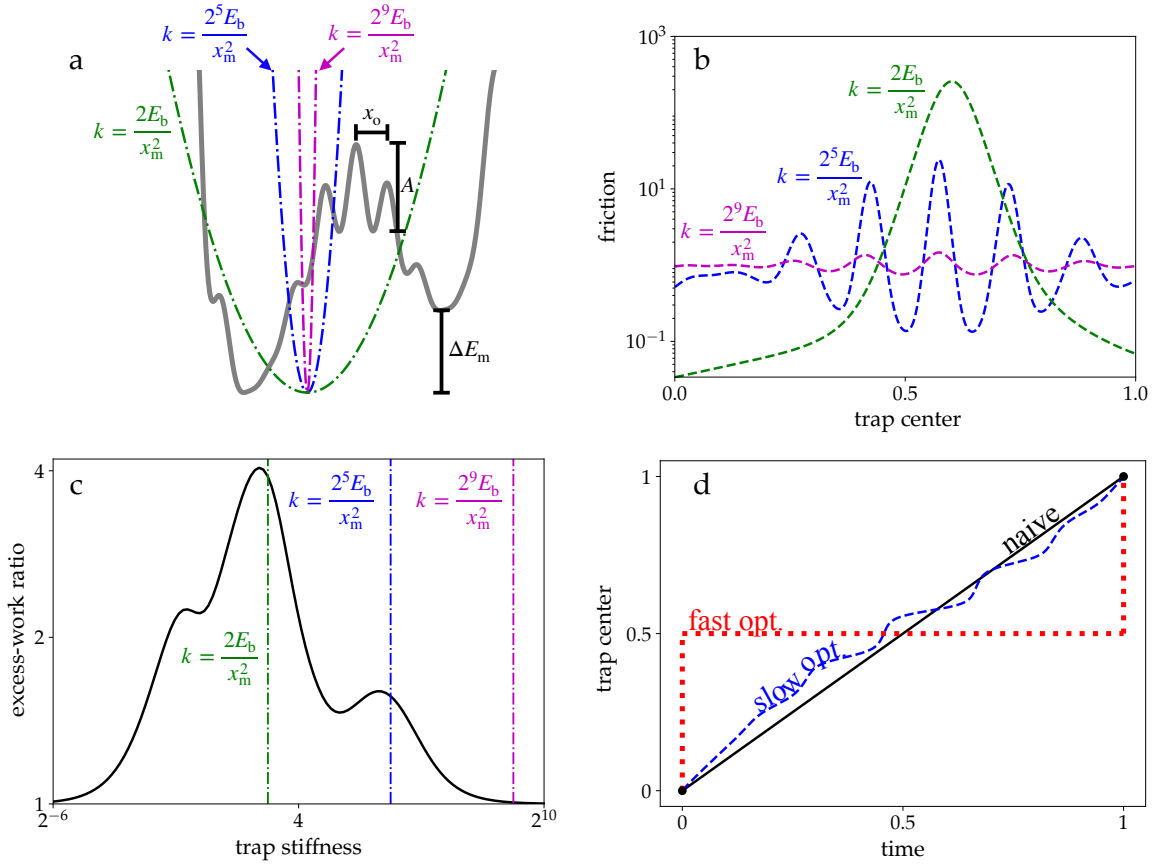

Fig 9.2. a) Double-well potential (2.2) (solid gray) with an energy offset ΔE_m between the minima at 0 and Δx_m. The trap potential (2.1) (dash-dotted) is centered at x^c. b) Friction (4.16) as a function of the trap center x^c. c) Excess-work ratio (4.19) as a function of trap stiffness. d) Designed protocols for trap stiffness $k = 2^5 E_\mathrm{b}/x_\mathrm{m}^2$, with "naive" the linear (constant velocity) protocol, "slow opt." the friction-optimized protocol (4.17), and "fast opt." the STEP (7.11). Throughout, the barrier height is $E_\mathrm{b} = 8\beta^{-1}$, energy offset $\Delta E_\mathrm{m} = 2\beta^{-1}$, amplitude of oscillations is $A = 2\beta^{-1}$ with wavelength $x_\mathrm{o} = x_\mathrm{m}/3$, and trap stiffness is $k = 2E_\mathrm{b}/x_\mathrm{m}^2$ (green), $2^5 E_\mathrm{b}/x_\mathrm{m}^2$ (blue), or $2^9 E_\mathrm{b}/x_\mathrm{m}^2$ (purple).

the friction landscape is relatively flat. For $k \ll E_\mathrm{b}/x_\mathrm{m}^2$, the total potential (3.4) is dominated by the underlying landscape potential (independent of the trap potential), so the friction (4.14) is independent of the trap center. For $k \gg E_\mathrm{b}/x_\mathrm{m}^2$, the total potential (3.4) is dominated by the trap potential (independent of the underlying landscape), and the friction approaches that of a harmonic trap on a flat landscape which is independent of the trap center.

The excess-work ratio (4.19) has a peak at an intermediate trap stiffness (Fig. 9.1c), since the friction for $k \ll E_\mathrm{b}/x_\mathrm{m}^2$ or $k \gg E_\mathrm{b}/x_\mathrm{m}^2$ is relatively flat resulting in a linear LR protocol (4.17) similar to the naive. For a trap stiffness $k \sim E_\mathrm{b}/x_\mathrm{m}^2$, the LR protocol is significantly different from the naive (Fig. 9.1d) resulting in a significant reduction in excess work compared to the naive and hence a large excess-work ratio.

For a double-well potential (9.3) with an energy offset and modulated by sinusoidal oscillations, and a trap stiffness comparable to the barrier height $k \sim E_\mathrm{b}/x_\mathrm{m}^2$, the maximum of the friction is offset from the center of the barrier (Fig. 9.2b) due to the energy offset ΔE_b. For a trap stiffness comparable to the size of oscillation ($k \sim A/x_\mathrm{o}^2$), the friction has corresponding oscillations. For a trap stiffness significantly larger than any of the features of the energy landscape ($k \gg A/x_\mathrm{o}^2$ and $k \gg E_\mathrm{b}/x_\mathrm{m}^2$), the friction is relatively flat. These features are reflected in the ratio of excess work in Fig. 9.2c as peaks at $k \sim E_\mathrm{b}/x_\mathrm{m}^2$ and $k \sim A/x_\mathrm{o}^2 = 18E_\mathrm{b}/x_\mathrm{m}^2 \sim 2^4 E_\mathrm{b}/x_\mathrm{m}^2$. The largest excess-work ratio occurs when the trap stiffness is comparable to the barrier height ($k \sim E_\mathrm{b}/x_\mathrm{m}^2$) which is the largest feature of the energy landscape. There is a third peak in the excess-work ratio for a trap stiffness less than the barrier height ($k < E_\mathrm{b}/x_\mathrm{m}^2$) caused by the energy offset ΔE_m. The oscillations in the friction for $k \sim A/x_\mathrm{o}^2$ are reflected in the slow optimal protocol in Fig. 9.2d.

Fast Limit

In the fast limit, provided the trapping potential is quadratic, the IFRR (7.5b), short-time power saving (7.12), STEP (7.11), and ratio of saved work (7.13) are independent of the underlying energy landscape.

For the model system of a translating harmonic trap, the IFRR (7.5b) is

$$\mathbf{R}_{\boldsymbol{\lambda}_\mathrm{i}}[x^\mathrm{c}(t)] = \beta D k^2 [x^\mathrm{c}(0) - x^\mathrm{c}(t)] \;, \tag{9.4}$$

leading to the short-time power saving

$$P_\mathrm{save}^\mathrm{st}(\boldsymbol{\lambda}) = \beta D k^2 [x_\mathrm{i}^\mathrm{c} - x^\mathrm{c}(t)][x_\mathrm{f}^\mathrm{c} - x^\mathrm{c}(t)] \;, \tag{9.5}$$

which is maximized at the STEP value

$$x^{\mathrm{STEP}} = \frac{x_{\mathrm{i}}^{\mathrm{c}} + x_{\mathrm{f}}^{\mathrm{c}}}{2} \ , \tag{9.6}$$

halfway between the control-parameter endpoints. The STEP therefore jumps to and from the control-parameter endpoints to spend the entire duration at x^{STEP}. This results in a ratio of saved work

$$\frac{\langle W_{\mathrm{save}} \rangle_{\Lambda}^{\mathrm{STEP}}}{\langle W_{\mathrm{save}} \rangle_{\Lambda}^{\mathrm{naive}}} \approx \frac{3}{2} \ . \tag{9.7}$$

These results are independent of the underlying energy landscape and are valid provided the trap potential is quadratic. For higher-order trapping potentials (e.g., quartic) the IFRR will depend on the underlying energy landscape.

For applications to free-energy estimation resulting from quadratic trapping, for example as realized by optical tweezers or steered molecular dynamics, the minimum-dissipation protocol is given by the STEP that spends the entire duration at the control-parameter value halfway between the endpoints. This STEP will result in a factor of ~ 1.5 improvement in saved work compared to the naive (constant-velocity) protocol.

9.2.2 Two-Parameter Control

The symmetric barrier crossing described by (2.2) with quadratic trapping potential (2.1) is studied for two-parameter control. The protocols considered drive the system between the two minima $x_{\mathrm{i}}^{\mathrm{c}} = 0$ and $x_{\mathrm{f}}^{\mathrm{c}} = \Delta x_{\mathrm{m}}$ with equal initial and final stiffness ($k_{\mathrm{i}} = k_{\mathrm{f}}$). With these protocols, control over only trap center can be directly compared to control over both trap center and stiffness.

Slow Limit

This section describes the designed protocols (geodesics) based on the friction matrix for driven barrier crossing under control of both trap center and stiffness (two-parameter control). The two-parameter linear-response (2P LR) protocol changes stiffness most when the initial stiffness is comparable to the scaled barrier height ($k_{\mathrm{i}} \sim E_{\mathrm{b}}/x_{\mathrm{m}}^2$), and leaves stiffness virtually unchanged when the initial stiffness is either large ($k_{\mathrm{i}} \gg E_{\mathrm{b}}/x_{\mathrm{m}}^2$) or small ($k_{\mathrm{i}} \ll E_{\mathrm{b}}/x_{\mathrm{m}}^2$). Physically, large (small) initial stiffness ensures that the initial equilibrium distribution is unimodal (bimodal). Throughout, the stiffness is compared to the *scaled barrier height* $E_{\mathrm{b}}/x_{\mathrm{m}}^2$, essentially comparing the initial energy at the barrier of the trap and the hairpin potential.

For slow driving, the excess work is described by (4.13), where the friction can be directly calculated from (4.16) to yield the friction matrix shown in Fig. 9.3. The geodesics are found by numerically solving (4.18) with specified initial and final trap center and stiffness, as described in Refs. 76,77.

All components of the friction have the largest variation in magnitude across the protocol when the trap stiffness is comparable to the scaled barrier height ($k \sim E_{\mathrm{b}}/x_{\mathrm{m}}^2$). If the stiffness is small ($k \ll E_{\mathrm{b}}/x_{\mathrm{m}}^2$) or large ($k \gg E_{\mathrm{b}}/x_{\mathrm{m}}^2$), then all components of the friction are independent of the trap center. For $k \ll E_{\mathrm{b}}/x_{\mathrm{m}}^2$, the total potential (3.4) is dominated by the hairpin potential (independent of the trap potential), so the friction (4.14) is independent of the trap center and stiffness. For $k \gg E_{\mathrm{b}}/x_{\mathrm{m}}^2$, the total potential is dominated by the trap potential (independent of the hairpin potential), and the friction approaches that of a harmonic trap on a flat landscape, which is also independent of the trap center.

The center-center component $\zeta_{\mathrm{c,c}}$ of the friction matrix is strongly peaked at the barrier (Fig. 9.3). This component is proportional to the force variance $\langle(\delta f_{x^{\mathrm{c}}})^2\rangle_{\boldsymbol{\lambda}} = k\langle(\delta x)^2\rangle_{\boldsymbol{\lambda}}$, which is largest in magnitude at the barrier. The barrier reduces the effective stiffness of the total potential, thereby increasing the position variance. Physically, a distribution sharply peaked at the trap center requires less work to translate than a wider distribution.

The stiffness-stiffness component $\zeta_{\mathrm{s,s}}$ of the friction is proportional to the fourth moment of the position distribution, $\langle(\delta f_k)^2\rangle_{\boldsymbol{\lambda}} = \langle[\delta(x - x^{\mathrm{c}})^2]^2\rangle_{\boldsymbol{\lambda}}/4$, which is largest when the distribution has appreciable probability of extreme values. Therefore, this component of the friction is largest when the total potential is a double well with two widely separated wells. For $k \lesssim E_{\mathrm{b}}/x_{\mathrm{m}}^2$, there is significant probability in the well opposite the trap (i.e., the distribution is bimodal), and pulling the trap closer to the center reduces the friction by reducing the distance between the two minima of the total potential. For $k \gtrsim E_{\mathrm{b}}/x_{\mathrm{m}}^2$, the total potential only has one minimum, and therefore this component of the friction is largest when the (unimodal) position distribution is widest, which occurs at the barrier. Physically, it takes more work to tighten the trap when the system is far from the trap center, scaling as $(x - x^{\mathrm{c}})^4$.

The off-diagonal component $\zeta_{\mathrm{c,s}}$ has both positive contributions, $\zeta_{\mathrm{c,s}}^{+} \equiv \max(\zeta_{\mathrm{c,s}}, 0)$, and negative contributions, $\zeta_{\mathrm{c,s}}^{-} \equiv \max(-\zeta_{\mathrm{c,s}}, 0)$. The off-diagonal components result from cross-correlations between the conjugate forces, and can either increase or decrease the work compared to treating the conjugate forces as uncorrelated (ignoring off-diagonal components).

First consider a weak trap, $k \lesssim E_{\mathrm{b}}/x_{\mathrm{m}}^2$. For $x^{\mathrm{c}} < \Delta x_{\mathrm{m}}/2$, $\zeta_{\mathrm{c,s}}$ is negative so increasing or decreasing both the trap center and stiffness together results in negative contribution to the total work from this component. Tightening the trap as the system is driven over the barrier causes this contribution to reduce the total work. For $x^{\mathrm{c}} > \Delta x_{\mathrm{m}}/2$, $\zeta_{\mathrm{c,s}}$ is positive so the contribution to the total work is negative if the trap center is increased as the stiffness is

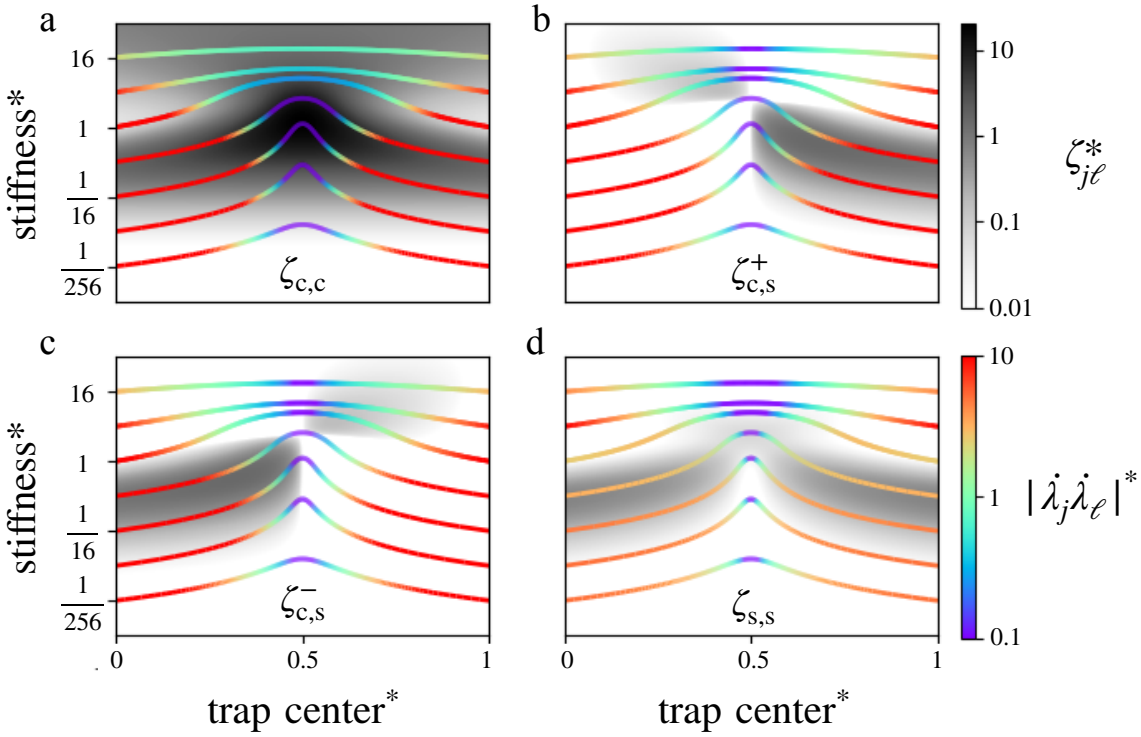

Fig 9.3. Geodesics and components of the friction matrix used to design two-parameter linear-response protocols. Grayscale heatmap: components of the friction as a function of the (dimensionless) trap center* $x^{\mathrm{c}}/\Delta x_{\mathrm{m}}$ and stiffness* $kx_{\mathrm{m}}^2/E_{\mathrm{b}}$. Colored curves: geodesics of the friction for equal initial and final trap stiffness ($k_{\mathrm{i}} = k_{\mathrm{f}}$). Color heatmap: absolute product of control-parameter speeds $\dot{\lambda}_j = \mathrm{d}\lambda_j/\mathrm{d}t$. The positive and negative components of the off-diagonal entry $\zeta_{\mathrm{c,s}}$ are respectively denoted by $\zeta^{+}_{\mathrm{c,s}}$ (b) and $\zeta^{-}_{\mathrm{c,s}}$ (c). A star denotes a scaled (dimensionless) quantity, with the velocities scaled by the average speed, $|\dot{\lambda}_j\dot{\lambda}_\ell|^{*} \equiv |\dot{\lambda}_j\dot{\lambda}_\ell|/(\overline{|\dot{\lambda}_j|}\ \overline{|\dot{\lambda}_\ell|})$, and friction as $\zeta^{*}_{j\ell} \equiv \beta D\zeta_{j\ell}\lambda_j\lambda_\ell/(\lambda^{*}_j\lambda^{*}_\ell x^2_{\mathrm{m}})$.

decreased. Loosening the trap as it is driven away from the barrier causes this contribution to decrease the total work.

For a strong trap ($k \gtrsim E_\mathrm{b}/x_\mathrm{m}^2$), the situation is reversed: tightening the trap as the system is driven up the energy landscape and loosening the trap as it is driven down result in a positive total-work contribution from the off-diagonal component. Since the trap is stiff compared to the hairpin potential, tightening no longer helps pull the system up the energy landscape and instead more tightly confines the system, attenuating thermal fluctuations which would otherwise help kick the system over the barrier.

In the slow limit, the two-parameter linear-response (2P LR) protocol minimizes dissipation by tightening the trap and slowing down as it traverses the barrier (Fig. 9.4). Tightening the trap when approaching the barrier (Fig. 9.4b) helps the system maintain roughly constant variance throughout the protocol and approximately linearly changes the quantiles of the position distribution (Fig. 9.5), which is a generic property for minimum-dissipation protocols in optimal transport under full control (section 4.1). When the trap doesn't tighten (e.g., naive and 1P LR protocols in Fig. 9.5), the variance increases as the system crosses the barrier and the quantiles do not change linearly. Slowing down while crossing the barrier (previously observed for one-parameter (constant-stiffness) barrier crossing[66]) allows time for thermal fluctuations to kick the system over the barrier (Fig. 9.4a).

Fast Limit

For a rapidly driven system, the minimum-dissipation protocol consists of two discrete jumps, spending the entire duration at fixed control-parameter values. This type of discrete protocol requires work

$$\langle W \rangle_{\boldsymbol{\Lambda}} = \left\langle V_\mathrm{tot}(x, \boldsymbol{\lambda}_\mathrm{f}) - V_\mathrm{tot}(x, \boldsymbol{\lambda}) \right\rangle_{\boldsymbol{\Lambda}} + \left\langle V_\mathrm{tot}(x, \boldsymbol{\lambda}) - V_\mathrm{tot}(x, \boldsymbol{\lambda}_\mathrm{i}) \right\rangle_{\boldsymbol{\lambda}_\mathrm{i}} . \tag{9.8}$$

The first term is the change in energy due to a jump from $\boldsymbol{\lambda}$ to $\boldsymbol{\lambda}_\mathrm{f}$, averaged over the distribution at the end of the protocol $\boldsymbol{\Lambda}$, and the second term is the change in energy due to a jump from $\boldsymbol{\lambda}_\mathrm{i}$ to $\boldsymbol{\lambda}$, averaged over the initial equilibrium distribution at $\boldsymbol{\lambda}_\mathrm{i}$.

For short duration Δt, the probability distribution at the conclusion of the protocol is approximated as (chapter 7)[47]

$$p_{\Delta t}(x, \boldsymbol{\Lambda}) \approx \pi_\mathrm{i}(x) + \Delta t \, L(x, \boldsymbol{\lambda}) \pi_\mathrm{i}(x) \tag{9.9a}$$

$$\approx \pi_\mathrm{i}(x) + \Delta t \, \left[L(x, \boldsymbol{\lambda}) - L(x, \boldsymbol{\lambda}_\mathrm{i}) \right] \pi_\mathrm{i}(x) , \tag{9.9b}$$

where $L(x, \boldsymbol{\lambda})$ is the time-evolution operator for the probability distribution at fixed control parameter $\boldsymbol{\lambda}$, and the second line used the fact that the initial equilibrium distribution

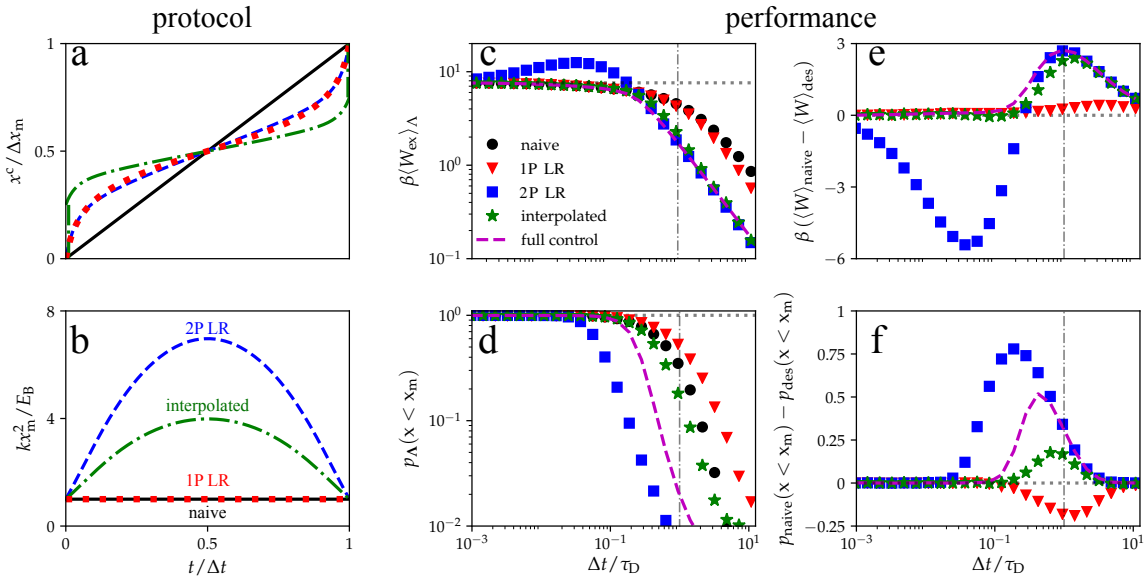

Fig 9.4. Performance of the naive (black), 1P LR (red), 2P LR (blue), and interpolated (green) protocols. (One-parameter control maintains constant stiffness and varies only the trap center.) Protocols show (a) trap center and (b) trap stiffness, as a function of time t normalized by protocol duration Δt. The interpolated protocol is shown for a duration $\Delta t = \tau_D$. (c) Excess work $\langle W_{ex} \rangle_{\mathbf{\Lambda}}$, (d) probability $p_{\Delta t}(x < x_m, \mathbf{\Lambda})$ that a trajectory does not cross the barrier, (e) difference in work between designed and naive protocols, and (f) difference in $p_{\Delta t}(x < x_m, \mathbf{\Lambda})$ between naive and designed protocols, all as functions of protocol duration $\Delta t/\tau_D$ scaled by diffusion time τ_D between the two wells. Purple dashed curve: optimal-transport process under full control.

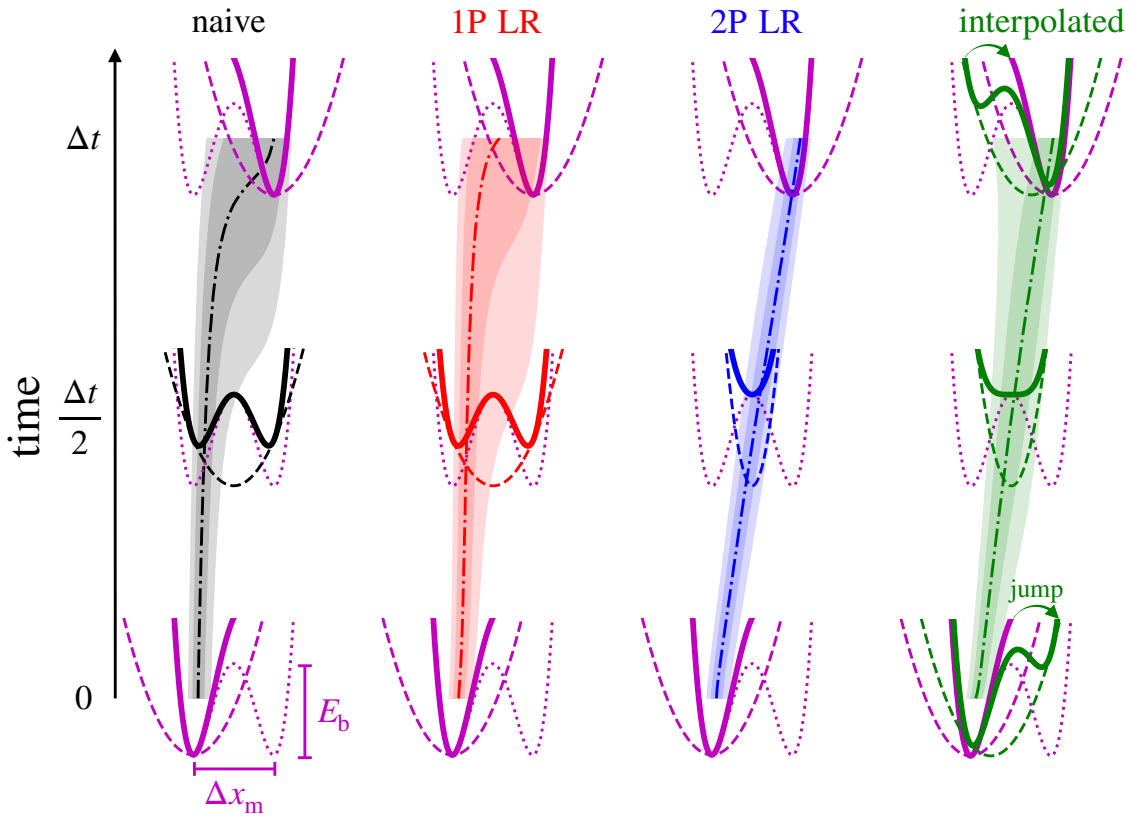

Fig 9.5. Time-dependent protocols for driven barrier crossing at intermediate protocol duration. Naive (black), one-parameter linear response (1P LR, red), two-parameter linear response (2P LR, blue), and interpolated (green). Snapshots of the total (solid), static hairpin (dotted), and time-dependent trap (dashed) potential are shown for $t = 0$, $\Delta t/2$, and Δt. The hairpin, initial, and final potentials are the same across protocols (purple). Dash-dotted curves: median positions during corresponding protocol. Shading: 9%, 25%, 75%, and 91% quantiles, which are approximately evenly spaced for a Gaussian distribution. Barrier height is $E_b = 4\beta^{-1}$, initial and final trap stiffnesses are $k_i = k_f = 4/(\beta x_m^2)$, and protocol duration equals the diffusion time $\tau_D = \Delta x_m^2/(2D)$ between the two wells.

satisfies $L(x, \boldsymbol{\lambda}_\mathrm{i})\pi_\mathrm{i}(x) = 0$. For Fokker-Planck dynamics this gives

$$p_{\Delta t}(x, \boldsymbol{\Lambda}) \approx \pi_\mathrm{i}(x) + \beta D \Delta t \frac{\partial}{\partial x}\Big\{ \big[f_x(x, \boldsymbol{\lambda}) - f_x(x, \boldsymbol{\lambda}_\mathrm{i}) \big] \pi_\mathrm{i}(x) \Big\} \;, \tag{9.10}$$

for force $f_x(x, \boldsymbol{\lambda}) \equiv -\partial V_\mathrm{tot}(x, \boldsymbol{\lambda})/\partial x$. Substituting into (9.8) and rearranging gives

$$\langle W_\mathrm{save} \rangle_{\boldsymbol{\Lambda}} \equiv \big\langle V_\mathrm{tot}(x, \boldsymbol{\lambda}_\mathrm{f}) - V_\mathrm{tot}(x, \boldsymbol{\lambda}_\mathrm{i}) \big\rangle_{\boldsymbol{\lambda}_\mathrm{i}} - \langle W \rangle_{\boldsymbol{\Lambda}} \tag{9.11a}$$

$$= \beta D \Delta t \int \mathrm{d}x \, \big[V_\mathrm{tot}(\boldsymbol{\lambda}) - V_\mathrm{tot}(\boldsymbol{\lambda}_\mathrm{f}) \big] \frac{\partial}{\partial x}\Big\{ \big[f_x(x, \boldsymbol{\lambda}) - f_x(x, \boldsymbol{\lambda}_\mathrm{i}) \big] \pi_\mathrm{i}(x) \Big\} \;, \tag{9.11b}$$

Integrating by parts leads to

$$\langle W_\mathrm{save} \rangle_{\boldsymbol{\Lambda}} = \beta D \Delta t \Big\langle \big[f_x(x, \boldsymbol{\lambda}_\mathrm{f}) - f_x(x, \boldsymbol{\lambda}) \big] \big[f_x(x, \boldsymbol{\lambda}) - f_x(x, \boldsymbol{\lambda}_\mathrm{i}) \big] \Big\rangle_{\boldsymbol{\lambda}_\mathrm{i}} \;. \tag{9.12}$$

The short-time power saving is

$$P^\mathrm{st}_\mathrm{save}(\boldsymbol{\lambda}) = \frac{\langle W_\mathrm{save} \rangle_{\boldsymbol{\Lambda}}}{\Delta t} \tag{9.13a}$$

$$= \beta D \Big\langle \big[f_x(x, \boldsymbol{\lambda}_\mathrm{f}) - f_x(x, \boldsymbol{\lambda}) \big] \big[f_x(x, \boldsymbol{\lambda}) - f_x(x, \boldsymbol{\lambda}_\mathrm{i}) \big] \Big\rangle_{\boldsymbol{\lambda}_\mathrm{i}} \;, \tag{9.13b}$$

and is maximized if

$$\left\langle \frac{\partial f_x(x, \boldsymbol{\lambda})}{\partial \boldsymbol{\lambda}} \left[f_x(x, \boldsymbol{\lambda}) - \frac{f_x(x, \boldsymbol{\lambda}_\mathrm{i}) + f_x(x, \boldsymbol{\lambda}_\mathrm{f})}{2} \right] \right\rangle_{\boldsymbol{\lambda}_\mathrm{i}} = 0 \;. \tag{9.14}$$

This can be achieved by control parameters which for all x satisfy $\partial f_x(x, \boldsymbol{\lambda})/\partial \boldsymbol{\lambda} = 0$ or $f_x(x, \boldsymbol{\lambda}) = [f_x(x, \boldsymbol{\lambda}_\mathrm{i}) + f_x(x, \boldsymbol{\lambda}_\mathrm{f})]/2$.

The minimum-dissipation protocol in the fast limit (the STEP) maximizes the short-time power saving (9.13b) by jumping from and to the control-parameter endpoints to spend the entire duration at control-parameter values $x^\mathrm{STEP} = (x^\mathrm{c}_\mathrm{i} + x^\mathrm{c}_\mathrm{f})/2$, and $k^\mathrm{STEP} = k_\mathrm{i}$. This result is independent of the hairpin potential since $V_\mathrm{tot}(x, \boldsymbol{\lambda}) = [V_\mathrm{tot}(x, \boldsymbol{\lambda}_\mathrm{i}) + V_\mathrm{tot}(x, \boldsymbol{\lambda}_\mathrm{f})]/2$ maximizes the short-time power saving (9.14) for all x independent of $V_\mathrm{land}(x)$ (note $k_\mathrm{f} = k_\mathrm{i}$).

Interpolated Protocols

Given theory describing minimum-dissipation control in both the slow and fast limits, a simple interpolation scheme is developed to design protocols that reduce dissipation at all driving speeds. Similar to the one-parameter case (chapter 7),[47] the interpolated protocol has an initial jump $(\boldsymbol{\lambda}^\mathrm{STEP} - \boldsymbol{\lambda}_\mathrm{i})/(1 + \Delta t/\tau)$ and a final jump $(\boldsymbol{\lambda}_\mathrm{f} - \boldsymbol{\lambda}^\mathrm{STEP})/(1 + \Delta t/\tau)$,

and follows the linear-response path between them,

$$\boldsymbol{\lambda}^{\text{interp}}(t) = \frac{1}{1+\frac{\Delta t}{\tau}}\boldsymbol{\lambda}^{\text{STEP}} + \left(1 - \frac{1}{1+\frac{\Delta t}{\tau}}\right)\boldsymbol{\lambda}^{\text{LR}}(t) \ , \tag{9.15}$$

with τ the crossover duration. This guarantees that the protocol approaches the minimum-dissipation protocol in both the fast and slow limits. For system timescale, the diffusion time $\tau_{\text{D}} \equiv \Delta x_{\text{m}}^2/(2D)$ between wells is used (primarily for its simplicity).

Figure 9.4 shows the interpolated protocol for symmetric barrier crossing at intermediate protocol duration. The interpolated protocol has jumps in the trap center at the start and end of the protocol, and tightens the trap as it crosses the barrier. Figure 9.5 shows the quantiles of the position distribution throughout the interpolated protocol. Since the trap is not as stiff as the 2P LR protocol, as it crosses the barrier it does not drive the quantiles as linearly as the 2P LR protocol does; however, as discussed in the following section, the interpolated protocol nevertheless outperforms the 2P LR in terms of dissipation.

9.2.3 Performance

For comparison to an ideal process, the performance of optimal-transport under full control is evaluated.[39,50,122] Optimal transport (Chapter 4) is used to calculate the minimum work required—assuming complete control over the potential—to move probability from an initial to final distribution within a fixed duration as

$$W_{\text{OT}} = \Delta F_{\text{eq}} + \frac{1}{D\Delta t}\int_0^1 \mathrm{d}y\, [Q_{\text{f}}(y) - Q_{\text{i}}(y)]^2 \ , \tag{9.16}$$

where Q_{f} and Q_{i} are the final and initial quantile functions (inverse cumulative distribution functions). A second optimization over the final probability distribution is performed, subject to constrained initial and final control-parameter endpoints. This yields the minimum work to drive the trap between the two endpoints assuming full control over the potential (rather than just one- or two-parameter parametric control).

Figure 9.4 compares naive, one-parameter linear-response (1P LR), two-parameter linear-response (2P LR), and interpolated protocols. Performance is measured by the average work (the direct target of the protocol design) and the probability $p_{\boldsymbol{\Lambda}}(x < x_{\text{m}})$ that the system remains in its initial well (related to the average flux), which was not directly considered in the design. The barrier height $E_{\text{b}} = 4\beta^{-1}$ is intermediate in the context of DNA hairpins,[12,13] and the initial and final stiffness are comparable to the scaled barrier height, $k_{\text{i}} = k_{\text{f}} = E_{\text{b}}/x_{\text{m}}^2$. For a 1-$\mu$m bead in water at standard temperature and pressure, with inter-well distance $\Delta x_{\text{m}} \approx 20$ nm, the initial and final stiffness correspond to $k_{\text{i}} = k_{\text{f}} \approx 0.16$

pN/nm, the 2P LR protocol reaches a maximum stiffness of $k_{\max} \approx 1.12$ pN/nm, and the diffusion time between wells is $\tau_D \approx 0.4$ s.

For long duration ($\Delta t \gg \tau_D$), the 1P LR protocol requires ($\sim$1.6$\times$) less work than the naive; however, the 2P LR and interpolated protocols most significantly reduce work (Fig. 9.4c; $\sim$5.6$\times$ less than naive, $\sim$3.5$\times$ less than 1P LR, and within 1% of full control). Intermediate-duration designed protocols give the largest-magnitude work reduction $\langle W \rangle_{\text{des}} - \langle W \rangle_{\text{naive}}$: 2P LR and interpolated protocols save $\sim 2.7\,\beta^{-1}$, whereas 1P LR only saves $\sim 0.4\,\beta^{-1}$ (Fig. 9.4e).

1P LR protocols often reduce dissipation but as a side effect also decrease flux, as seen in Fig. 9.4d. 2P LR and interpolated protocols have the opposite effect, decreasing dissipation while increasing flux. For intermediate duration, the 2P LR protocol drives up to 78% and the interpolated up to 17% more probability to the destination well, compared to naive; the 1P LR drives 19% *less*.

For long duration ($\Delta t \gg \tau_D$), two-parameter control provides significant advantages over one-parameter control for both average work and flux; however, for short duration the 2P LR protocol can perform worse than 1P LR and naive (Fig. 9.4c and e; similar behavior has been observed for multiparameter control of the Ising model[77]). For short duration, the system cannot keep up with the rapid changes in the trap potential, and the linear-response approximation breaks down. Although the increased stiffness of the 2P LR protocol results in the strongest driving and hence the greatest flux of the protocols considered here (Fig. 9.4d/f), it does so at the cost of increased dissipation for short duration. Indeed, the minimum-dissipation protocol for short duration ($\Delta t \ll \tau_D$, the STEP) is monotonic and discrete. The interpolated protocol asymptotes to the STEP in the short-duration limit, resulting in reduced dissipation and increased flux at any duration. In terms of dissipation, the interpolated protocol achieves within 1% of the minimum work under full control for short and long duration and remains within 30% of full control at intermediate duration (Fig. 9.4c).

9.2.4 Comparison Between Control Strategies

This section compares naive (constant velocity) and designed protocols based on the methods described in the previous chapters: interpolated protocols combining STEP and slow-protocol approximations (Chapter 7), strong-trap approximation (Chapter 8), and full control (Chapter 4). The naive protocol serves as a baseline which the designed protocols should outperform, and full control as a bound on what parametric control could possibly achieve.

Fig. 9.6 shows the naive and designed protocols for intermediate driving speed, intermediate trap stiffness, and for fixed final control parameters. Every designed protocol has

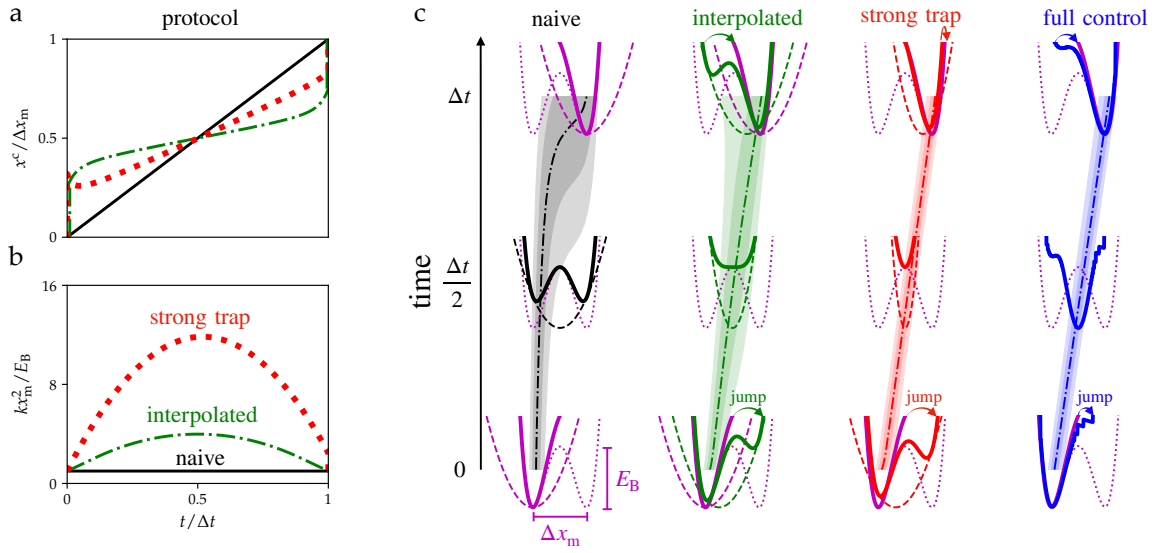

Fig 9.6. Time-dependent trap-center (a) and trap-stiffness (b) protocols for driven barrier crossing at intermediate protocol duration. The protocols are the naive (black), interpolated (green), strong-trap (red), and full-control (blue) protocols. c) Snapshots of the total (solid), static hairpin (dotted), and time-dependent trap (dashed) potential are shown for $t = 0$, $\Delta t/2$, and Δt. The hairpin, initial, and final potentials are the same across protocols (purple). Dash-dotted curves: median positions during corresponding protocol. Shading: 9%, 25%, 75%, and 91% quantiles, which are approximately evenly spaced for a Gaussian distribution. Barrier height is $E_b = 4\beta^{-1}$, initial and final trap stiffnesses are $k_i = k_f = 4\beta^{-1}x_m^{-2}$, and protocol duration equals diffusion time $\tau_D = \Delta x_m^2/(2D)$ between the two wells.

discontinuous jumps at the start and end of the protocol, and slows down and tightens the trap as it crosses the barrier. The behavior of the designed protocols can be understood in terms of the full-control solution. In one dimension the minimum-dissipation protocol linearly drives the quantiles of the probability distribution between the initial and final distributions. In the naive protocol, since it has constant stiffness, the probability distribution spreads out as it crosses the barrier, due to the negative curvature of the energy landscape at the barrier. To compensate for this, the designed protocols tighten as they cross the barrier; additionally, to compensate for the changes in the gradient of the energy landscape, the designed protocols slow down as they cross the barrier.

Fig. 9.7 shows the excess work of the designed protocols compared to the naive protocol. For long duration (slow protocol) all of the designed protocols significantly outperform the naive, with the difference between the minimum dissipation possible from full control

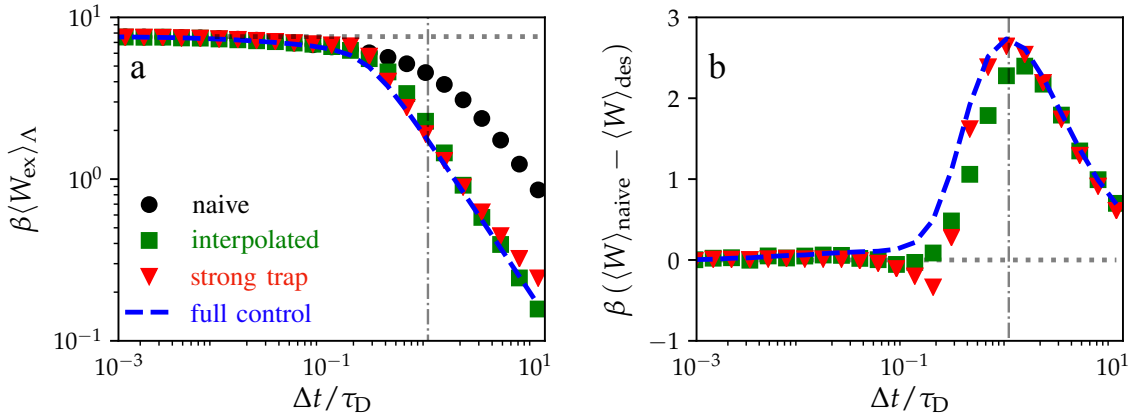

Fig 9.7. Performance of the naive (black circles), interpolated (green squares), strong-trap (red triangles), and full-control (blue dashed) protocols. (a) Excess work $\langle W_{\mathrm{ex}}\rangle_{\mathbf{\Lambda}}$ and (b) work difference $\langle W\rangle_{\mathrm{naive}} - \langle W\rangle_{\mathrm{des}}$ between designed and naive protocols, all as functions of protocol duration $\Delta t/\tau_{\mathrm{D}}$ scaled by diffusion time τ_{D}. Error bars representing bootstrap-resampled 95% confidence intervals are smaller than the markers.

indistinguishable from the dissipation from the interpolated protocol in this limit. While the approximations made in the interpolated protocol become exact in the long-duration limit, the same is not true for the strong-trap approximation. As a result, the strong-trap protocol has slightly higher dissipation in the long-duration limit, but would achieve the minimal dissipation in the limit of high trap stiffness. Furthermore, for intermediate protocol duration ($\Delta t \sim \tau_{\mathrm{D}}$), the strong control performs the best of the approximations since the approximation does not explicitly depend on the protocol duration. For short duration (fast protocols), all the designed protocols perform similarly well.

In summary, the designed protocols perform similarly well, so it seems reasonable to choose the control strategy which is simplest to determine, provided the approximations/assumptions required are satisfied. Since the strong-trap approximation has explicit solutions for the designed protocol, it will generally be the simplest to determine; however, it is not as widely applicable as the interpolated protocols.

9.3 Discussion

Multiparameter control protocols can significantly outperform their one-parameter counterparts, improving both work and flux. For a system undergoing driven barrier crossing,

one-parameter control of only the trap center limits the control over the position distribution, with a large increase in variance as the protocol crosses the barrier (Fig. 9.6). Control over both the trap center and stiffness makes possible approximately linear driving of the position mean and variance between specified endpoints, consistent with optimal-transport protocols that minimize work under full control (Chapter 4).[39,50,122] This significantly reduces the work required to drive the system between the two wells and increases the flux compared to naive and one-parameter control protocols (Fig. 9.4). The main shortcoming of the multiparameter linear-response protocols is that they can perform worse than naive for short duration; however, this issue is remedied by combining linear-response and STEP frameworks to give interpolated protocols that reduce dissipation at any duration. For the model system and parameters explored, the largest reduction in dissipation occurs from one- to two-parameter control, and the dissipation in the two-parameter interpolated protocol is within 30% of full control for intermediate duration and within 1% for short and long duration.

The model system closely resembles DNA-hairpin experiments, with experimentally relevant parameters.[12,13] The results of this chapter reveal general design principles for driven barrier crossing that can be readily implemented experimentally: the designed protocols 1) slow down and tighten the trap as it crosses the energy barrier, thereby driving the mean position between the two wells at constant rate while maintaining constant variance; and 2) jump at the beginning and end of the protocol, with larger jumps for faster protocols. Recent experimental protocols implement one-parameter control and demonstrate significant work reductions from designed protocols.[80] Adding an additional control parameter (trap stiffness) can dramatically improve the performance over the one-parameter counterpart (up to 3.5× less work and ∼80% increased probability of reaching the target well). Although multiparameter control is more difficult to implement, the performance gains can be significant.

Chapter 10

Perspective and Outlook

I have analyzed optimal control in stochastic thermodynamics, including both full control and parametric control (chapter 4). I demonstrate general methods for determining minimum-dissipation protocols for parametric control ranging from weak to strong (chapter 8) and slow to fast (chapter 7). These approximations fill out the four limits of parametric control (Fig. 1.3) and can be combined to design protocols that reduce dissipation at any driving speed. These designed protocols reproduce key features determined by exact solutions for Gaussian distributions and quadratic trapping potentials, such as control-parameter jumps at the start and end of the protocol and linear driving of the distribution quantiles between specified endpoints (chapter 9).

For the model system of driven barrier crossing (chapter 2), interpolated, strong-control, and full-control solutions were compared (chapter 9). The designed protocols significantly outperform the naive (linear) protocol. Strong control has explicit solutions for the minimum-dissipation protocol, making it the simplest approximation to use; however, it is only applicable to overdamped dynamics with strong trapping potentials.

Figure 1.3 shows the limits in which solutions for the minimum-dissipation protocol for parametric control are known. The linear-response and slow-driving approximations have been applied to several different types of systems and control (chapter 4). A promising area of future study would be to explore if extensions and generalizations can be made to strong and fast control. Indeed, it has recently been shown that the fast-protocol approximation can be extended to quantum systems, classical Hamiltonian dynamics, and optimization of the variance of the work distribution.[202]

Another extension to consider is to allow for position-dependent diffusivity, which generically arises when a high-dimensional system is represented in a lower-dimensional space.[203] For example, DNA-hairpin experiments and molecular-dynamics simulations take place

in three spatial dimensions but are often represented as one-dimensional diffusive processes.[13,204,205] This requires averaging out the behavior in the other two dimensions, and any inhomogeneity in these dimensions will result in position-dependent effective diffusivity in the one-dimensional representation. Measured diffusivities in molecular-dynamics simulations often vary with position[204], and although accurate measurements remain a technical challenge, some hairpin experiments report a position-dependent diffusivity.[206] Position-dependent diffusivity can alter the kinetic transition state of protein folding,[207] which will impact the design of minimum-dissipation protocols. Therefore, position-dependent diffusivity may be an important consideration in some applications. The minimum-dissipation protocol under full control in inhomogeneous environments (e.g., position-dependent diffusivity) has been treated in detail in Ref. 119.

An important aspect of designing protocols to minimize dissipation in both experiments and theory is the choice of control parameters and number of control parameters. For the model system of driven barrier crossing, designed protocols with control over both trap center and stiffness (two-parameter control) significantly reduces dissipation compared to designed protocols that can only adjust the trap center (single-parameter control).[82] However, adding even more control parameters does not significantly reduce dissipation any further, because this system is well approximated as a one-dimensional Gaussian, for which the full-control solution only requires two parameters to adjust the mean and variance (section 4.1.1). Although this phenomenon is well explained for one-dimensional overdamped systems, considerably less is known more generally. For example, Ref. 77 compared one-, two-, and four-parameter control of the Ising model and found significant qualitative and quantitative differences between the designed protocols. Since the full-control solution for this system is not yet known, this phenomenon cannot be explained in the same way as for driven barrier crossings. Beyond simply the number of control parameters, it remains an open question as to which control parameters are the most important when designing protocols to minimize dissipation. The choice of control parameters and number of control parameters will be important for experimental and computational applications, such as free-energy estimation.

Leveraging optimal-transport theory appears to be a promising approach towards a deeper understanding of optimal control in stochastic thermodynamics. Full-control solutions based on optimal-transport theory were initially only applicable to continuous classical systems with overdamped dynamics;[50,52] however, recent studies have begun to expand their range of applicability to discrete-state and quantum systems.[53,57–61]

The full-control solutions give an idealized view of optimal control and will always outperform parametric control, but can be used as the ideal solution that parametric control can strive towards and draw insight from. For example, linearly driving the quantiles between the initial and final endpoints is the minimum-dissipation protocol for a one-dimensional system under full control; this is reasonably well reproduced by parametric

control of driven barrier crossing (chapter 9). Furthermore, it has recently been shown that optimal-transport theory can be leveraged to design minimum-dissipation protocols under parametric control,[59] which is a promising new technique for determining exact minimum-dissipation protocols at any driving speed or strength of driving.

The focus of this thesis has been on protocols which reduce the average work or entropy production; however, higher-order moments (e.g., variance or skewness), or individual trajectory optimization[208] may also be of interest for strongly fluctuating systems. Ref. 168 compared for a breathing harmonic trap the protocols that minimize work variance with those that minimize average work, finding that minimum-average-work and minimum-work-variance protocols qualitatively differ for intermediate-to-fast driving speeds. In contrast, for slow near-equilibrium control, the same protocols minimize average work and work variance 6, so a more complete description of minimum-variance protocols far from equilibrium is desirable.

This thesis has focused on systems driven by external control parameters, which is adequate for describing the experimental systems discussed in section 2; however, this does not accurately describe autonomous machines. For example, ATP synthase *in vivo* is driven by a proton gradient across the mitochondrial membrane which drives the coupled F_o and F_1 components. In this system, coupling between the components means that none of the components can be treated as external, and thus it is not obvious how the present discussion of optimal control applies to such autonomous machines. Some first steps towards the description of autonomous molecular machines are discussed in section 4.2.2; however, more work is required towards a full description of efficient autonomous machines.[209]

The majority of the studies on optimal control in stochastic thermodynamics have focused on theoretical understanding and simple toy models. There is a deep understanding of minimum-dissipation protocols at both slow and fast driving speed and both weak and strong driving strength (Fig. 1.3). It would be interesting to see how these results apply to real physical systems and if they are able to achieve the promising results predicted by theory. The two most straightforward applications are to relatively simple experimental model systems (chapter 2)+ in an analogous fashion to Ref. 80, and to free-energy estimation as discussed in chapter 5, in a similar fashion to Refs. 148–151.

References

[1] Steven Blaber and David A Sivak. Optimal control in stochastic thermodynamics. *ArXiv preprint ArXiv:2212.00706*, 2022.

[2] Sadi Carnot, Emile Clapeyron, and Rudolf Clausius. Reflections on the motive power of fire. In Eric Mendoza, editor, *Reflections on the Motive Power of Fire: And Others Papers on the Second Law of Thermodynamics*. New York: Dover Publications, 1960.

[3] Daniel V. Schroeder. *An introduction to thermal physics*. Addison Wesley Longman, 2000.

[4] J.H. Andrew and J.S. Allen. A confirmation of the location of the 1712 'Dudley castle' Newcomen engine at Coneygree, Tipton. *The International Journal for the History of Engineering & Technology*, 79(2):174–182, 2009.

[5] Albert Einstein et al. On the motion of small particles suspended in liquids at rest required by the molecular-kinetic theory of heat. *Ann. Phys.*, 17(549-560):208, 1905.

[6] Jean Perrin. L'agitation moléculaire et le mouvement brownien. *C. R. Acad. Sci. Paris*, 146:967–970, 1908.

[7] Arthur Ashkin. Acceleration and trapping of particles by radiation pressure. *Phys. Rev. Lett.*, 24(4):156, 1970.

[8] Jan Liphardt, Sophie Dumont, Steven B Smith, Ignacio Tinoco, and Carlos Bustamante. Equilibrium information from nonequilibrium measurements in an experimental test of Jarzynski's equality. *Science*, 296(5574):1832–1835, 2002.

[9] Delphine Collin, Felix Ritort, Christopher Jarzynski, Steven B Smith, Ignacio Tinoco, and Carlos Bustamante. Verification of the Crooks fluctuation theorem and recovery of RNA folding free energies. *Nature*, 437(7056):231–234, 2005.

[10] Carlos Bustamante, Steven B Smith, Jan Liphardt, and Doug Smith. Single-molecule studies of DNA mechanics. *Curr. Opin. Struct. Biol.*, 10(3):279–285, 2000.

[11] Carlos Bustamante, Zev Bryant, and Steven B Smith. Ten years of tension: single-molecule DNA mechanics. *Nature*, 421(6921):423–427, 2003.

[12] Michael T Woodside, William M Behnke-Parks, Kevan Larizadeh, Kevin Travers, Daniel Herschlag, and Steven M Block. Nanomechanical measurements of the sequence-dependent folding landscapes of single nucleic acid hairpins. *Proc. Natl. Acad. Sci. U.S.A*, 103(16):6190–6195, 2006.

[13] Krishna Neupane, Feng Wang, and Michael T Woodside. Direct measurement of sequence-dependent transition path times and conformational diffusion in DNA duplex formation. *Proc. Natl. Acad. Sci. U.S.A*, 114(6):1329–1334, 2017.

[14] Shoichi Toyabe, Takahiro Watanabe-Nakayama, Tetsuaki Okamoto, Seishi Kudo, and Eiro Muneyuki. Thermodynamic efficiency and mechanochemical coupling of F1-ATPase. *Proc. Natl. Acad. Sci. U.S.A*, 108(44):17951–17956, 2011.

[15] Shoichi Toyabe, Hiroshi Ueno, and Eiro Muneyuki. Recovery of state-specific potential of molecular motor from single-molecule trajectory. *Europhys. Lett.*, 97(4):40004, 2012.

[16] Kyogo Kawaguchi, Shin-ichi Sasa, and Takahiro Sagawa. Nonequilibrium dissipation-free transport in F1-ATPase and the thermodynamic role of asymmetric allosterism. *Biophys. J.*, 106(11):2450–2457, 2014.

[17] Karel Svoboda, Christoph F Schmidt, Bruce J Schnapp, and Steven M Block. Direct observation of kinesin stepping by optical trapping interferometry. *Nature*, 365(6448):721–727, 1993.

[18] Karel Svoboda and Steven M Block. Force and velocity measured for single kinesin molecules. *Cell*, 77(5):773–784, 1994.

[19] Hiroaki Kojima, Etsuko Muto, Hideo Higuchi, and Toshio Yanagida. Mechanics of single kinesin molecules measured by optical trapping nanometry. *Biophys. J.*, 73(4):2012–2022, 1997.

[20] Alan J Hunt, Frederick Gittes, and Jonathon Howard. The force exerted by a single kinesin molecule against a viscous load. *Biophys. J.*, 67(2):766–781, 1994.

[21] Michael J. Greenberg, Göker Arpağ, Erkan Tüzel, and E. Michael Ostap. A perspective on the role of myosins as mechanosensors. *Biophys. J.*, 110(12):2568–2576, 2016.

[22] Joseph M. Laakso, John H. Lewis, Henry Shuman, and E. Michael Ostap. Myosin I can act as a molecular force sensor. *Science*, 321(5885):133–136, 2008.

[23] Melanie F. Norstrom, Philip A. Smithback, and Ronald S. Rock. Unconventional processive mechanics of non-muscle myosin IIB*. *J. Biol. Chem.*, 285(34):26326–26334, 2010.

[24] Attila Nagy, Yasuharu Takagi, Neil Billington, Sara A. Sun, Davin K.T. Hong, Earl Homsher, Aibing Wang, and James R. Sellers. Kinetic characterization of nonmuscle myosin IIB at the single molecule level*. *J. Biol. Chem.*, 288(1):709–722, 2013.

[25] C. Jarzynski. Nonequilibrium equality for free energy differences. *Phys. Rev. Lett.*, 78:2690–2693, 1997.

[26] Gavin E Crooks. Entropy production fluctuation theorem and the nonequilibrium work relation for free energy differences. *Phys. Rev. E*, 60(3):2721, 1999.

[27] Bjarne Andresen, R Stephen Berry, Abraham Nitzan, and Peter Salamon. Thermodynamics in finite time. I. the step-Carnot cycle. *Phys. Rev. A*, 15(5):2086, 1977.

[28] Peter Salamon, Bjarne Andresen, and R Stephen Berry. Thermodynamics in finite time. II. potentials for finite-time processes. *Phys. Rev. A*, 15(5):2094, 1977.

[29] Bjarne Andresen. Current trends in finite-time thermodynamics. *Angew. Chem. Int. Ed.*, 50(12):2690–2704, 2011.

[30] Yehuda B Band, Oded Kafri, and Peter Salamon. Finite time thermodynamics: Optimal expansion of a heated working fluid. *J. Appl. Phys.*, 53(1):8–28, 1982.

[31] Frank Weinhold. Metric geometry of equilibrium thermodynamics. *J. Chem. Phys.*, 63(6):2479–2483, 1975.

[32] George Ruppeiner. Thermodynamics: A Riemannian geometric model. *Phys. Rev. A*, 20(4):1608, 1979.

[33] Gavin E Crooks. Measuring thermodynamic length. *Phys. Rev. Lett.*, 99(10):100602, 2007.

[34] Peter Salamon and R Stephen Berry. Thermodynamic length and dissipated availability. *Phys. Rev. Lett.*, 51(13):1127, 1983.

[35] Udo Seifert. Stochastic thermodynamics, fluctuation theorems and molecular machines. *Rep. Prog. Phys.*, 75(12):126001, 2012.

[36] Christopher Jarzynski. Equalities and inequalities: Irreversibility and the second law of thermodynamics at the nanoscale. *Annu. Rev. Condens. Matter Phys.*, 2(1):329–351, 2011.

[37] Aidan I Brown and David A Sivak. Toward the design principles of molecular machines. *Physics in Canada*, 73(2), 2017.

[38] Aidan I Brown and David A Sivak. Theory of nonequilibrium free energy transduction by molecular machines. *Chem. Rev.*, 120(1):434–459, 2019.

[39] Karel Proesmans, Jannik Ehrich, and John Bechhoefer. Finite-time Landauer principle. *Phys. Rev. Lett.*, 125:100602, 2020.

[40] John Bechhoefer. *Control Theory for Physicists*. Cambridge University Press, 2021.

[41] Tim Schmiedl and Udo Seifert. Optimal finite-time processes in stochastic thermodynamics. *Phys. Rev. Lett.*, 98(10):108301, 2007.

[42] Paolo Abiuso, Viktor Holubec, Janet Anders, Zhuolin Ye, Federico Cerisola, and Martí Perarnau-Llobet. Thermodynamics and optimal protocols of multidimensional quadratic Brownian systems. *J. Phys. Commun.*, 6(6):063001, 2022.

[43] Steven Blaber and David A. Sivak. Optimal control with a strong harmonic trap. *Phys. Rev. E*, 106:L022103, 2022.

[44] Alex Gomez-Marin, Tim Schmiedl, and Udo Seifert. Optimal protocols for minimal work processes in underdamped stochastic thermodynamics. *J. Chem. Phys.*, 129(2):024114, 2008.

[45] Holger Then and Andreas Engel. Computing the optimal protocol for finite-time processes in stochastic thermodynamics. *Phys. Rev. E*, 77(4):041105, 2008.

[46] Massimiliano Esposito, Ryoichi Kawai, Katja Lindenberg, and Christian Van den Broeck. Finite-time thermodynamics for a single-level quantum dot. *Europhys. Lett.*, 89(2):20003, 2010.

[47] Steven Blaber, Miranda D. Louwerse, and David A. Sivak. Steps minimize dissipation in rapidly driven stochastic systems. *Phys. Rev. E*, 104:L022101, 2021.

[48] Cédric Villani. *Optimal transport: old and new*, volume 338. Springer, 2009.

[49] Filippo Santambrogio. *Optimal transport for applied mathematicians*, volume 55. Springer, 2015.

[50] Erik Aurell, Carlos Mejía-Monasterio, and Paolo Muratore-Ginanneschi. Optimal protocols and optimal transport in stochastic thermodynamics. *Phys. Rev. Lett.*, 106(25):250601, 2011.

[51] Yunxin Zhang. Work needed to drive a thermodynamic system between two distributions. *Europhys. Lett.*, 128(3):30002, 2019.

[52] Muka Nakazato and Sosuke Ito. Geometrical aspects of entropy production in stochastic thermodynamics based on Wasserstein distance. *Phys. Rev. Res.*, 3(4):043093, 2021.

[53] Andreas Dechant. Minimum entropy production, detailed balance and Wasserstein distance for continuous-time Markov processes. *J. Phys. A Math. Theor.*, 55(9):094001, 2022.

[54] Olga Movilla Miangolarra, Amirhossein Taghvaei, Yongxin Chen, and Tryphon T Georgiou. Geometry of finite-time thermodynamic cycles with anisotropic thermal fluctuations. *ArXiv preprint ArXiv:2203.12483*, 2022.

[55] Jean-David Benamou and Yann Brenier. A computational fluid mechanics solution to the Monge-Kantorovich mass transfer problem. *Numerische Mathematik*, 84(3):375–393, 2000.

[56] Karel Proesmans, Jannik Ehrich, and John Bechhoefer. Optimal finite-time bit erasure under full control. *Phys. Rev. E*, 102(3):032105, 2020.

[57] Andreas Dechant, Shin-ichi Sasa, and Sosuke Ito. Geometric decomposition of entropy production in out-of-equilibrium systems. *Phys. Rev. Res.*, 4(1):L012034, 2022.

[58] Kohei Yoshimura, Artemy Kolchinsky, Andreas Dechant, and Sosuke Ito. Geometrical approach to excess/housekeeping entropy production in discrete systems. *ArXiv preprint ArXiv:2205.15227*, 2022.

[59] Adrianne Zhong and Michael R DeWeese. Limited-control optimal protocols arbitrarily far from equilibrium. *ArXiv preprint ArXiv:2205.08662*, 2022.

[60] Tan Van Vu and Keiji Saito. Thermodynamic unification of optimal transport: thermodynamic uncertainty relation, minimum dissipation, and thermodynamic speed limits. *Phys. Rev. X*, 13(1):011013, 2023.

[61] Tan Van Vu and Keiji Saito. Topological speed limit. *Phys. Rev. Lett.*, 130(1):010402, 2023.

[62] Todd R Gingrich, Grant M Rotskoff, Gavin E Crooks, and Phillip L Geissler. Near-optimal protocols in complex nonequilibrium transformations. *Proc. Natl. Acad. Sci. U.S.A.*, 113(37):10263–10268, 2016.

[63] Megan C Engel, Jamie A Smith, and Michael P Brenner. Optimal control of nonequilibrium systems through automatic differentiation. *ArXiv preprint ArXiv:2201.00098*, 2022.

[64] Marcus VS Bonança and Sebastian Deffner. Minimal dissipation in processes far from equilibrium. *Phys. Rev. E*, 98(4):042103, 2018.

[65] Lucas P Kamizaki, Marcus VS Bonança, and Sérgio R Muniz. Performance of optimal linear-response processes in driven Brownian motion far from equilibrium. *ArXiv preprint ArXiv:2204.07145*, 2022.

[66] David A Sivak and Gavin E Crooks. Thermodynamic geometry of minimum-dissipation driven barrier crossing. *Phys. Rev. E*, 94(5):052106, 2016.

[67] Steven Blaber and David A Sivak. Optimal control of protein copy number. *Phys. Rev. E*, 101(2):022118, 2020.

[68] Sebastian Deffner and Marcus VS Bonança. Thermodynamic control—an old paradigm with new applications. *Europhys. Lett.*, 131(2):20001, 2020.

[69] Patrick R Zulkowski, David A Sivak, Gavin E Crooks, and Michael R DeWeese. Geometry of thermodynamic control. *Phys. Rev. E*, 86(4):041148, 2012.

[70] Marcus VS Bonança and Sebastian Deffner. Optimal driving of isothermal processes close to equilibrium. *J. Chem. Phys.*, 140(24):244119, 2014.

[71] Patrick R Zulkowski and Michael R DeWeese. Optimal control of overdamped systems. *Phys. Rev. E*, 92(3):032117, 2015.

[72] Patrick R Zulkowski and Michael R DeWeese. Optimal protocols for slowly driven quantum systems. *Phys. Rev. E*, 92(3):032113, 2015.

[73] Steven J Large and David A Sivak. Optimal discrete control: minimizing dissipation in discretely driven nonequilibrium systems. *J. Stat. Mech.: Theory Exp.*, 2019(8):083212, 2019.

[74] Joseph NE Lucero, Aliakbar Mehdizadeh, and David A Sivak. Optimal control of rotary motors. *Phys. Rev. E*, 99(1):012119, 2019.

[75] Grant M Rotskoff and Gavin E Crooks. Optimal control in nonequilibrium systems: Dynamic Riemannian geometry of the Ising model. *Phys. Rev. E*, 92(6):060102, 2015.

[76] Grant M Rotskoff, Gavin E Crooks, and Eric Vanden-Eijnden. Geometric approach to optimal nonequilibrium control: Minimizing dissipation in nanomagnetic spin systems. *Phys. Rev. E*, 95(1):012148, 2017.

[77] Miranda D. Louwerse and David A. Sivak. Multidimensional minimum-work control of a 2D Ising model. *J. Chem. Phys*, 156(19):194108, 2022.

[78] Adam G. Frim and Michael R. DeWeese. Optimal finite-time Brownian Carnot engine. *Phys. Rev. E*, 105:L052103, 2022.

[79] Adam G Frim and Michael R DeWeese. Geometric bound on the efficiency of irreversible thermodynamic cycles. *Phys. Rev. Lett.*, 128(23):230601, 2022.

[80] Sara Tafoya, Steven J Large, Shixin Liu, Carlos Bustamante, and David A Sivak. Using a system's equilibrium behavior to reduce its energy dissipation in nonequilibrium processes. *Proc. Natl. Acad. Sci. U.S.A*, 116(13):5920–5924, 2019.

[81] Steven Blaber and David A Sivak. Skewed thermodynamic geometry and optimal free energy estimation. *J. Chem. Phys.*, 153(24):244119, 2020.

[82] Steven Blaber and David A Sivak. Efficient two-dimensional control of barrier crossing. *Europhys. Lett.*, 139(1):17001, 2022.

[83] Yu-Han Ma, Dazhi Xu, Hui Dong, and Chang-Pu Sun. Optimal operating protocol to achieve efficiency at maximum power of heat engines. *Phys. Rev. E*, 98(2):022133, 2018.

[84] Yunxin Zhang. Optimization of stochastic thermodynamic machines. *J. Stat. Phys.*, 178(6):1336–1353, 2020.

[85] Paolo Abiuso and Martí Perarnau-Llobet. Optimal cycles for low-dissipation heat engines. *Phys. Rev. Lett.*, 124(11):110606, 2020.

[86] Jin-Fu Chen. Optimizing Brownian heat engine with shortcut strategy. *Phys. Rev. E*, 106(5):054108, 2022.

[87] Frank L Curzon and B Ahlborn. Efficiency of a Carnot engine at maximum power output. *Am. J. Phys.*, 43(1):22–24, 1975.

[88] Christian Van den Broeck. Thermodynamic efficiency at maximum power. *Phys. Rev. Lett.*, 95(19):190602, 2005.

[89] Tim Schmiedl and Udo Seifert. Efficiency of molecular motors at maximum power. *Europhys. Lett.*, 83(3):30005, 2008.

[90] Massimiliano Esposito, Katja Lindenberg, and Christian Van den Broeck. Universality of efficiency at maximum power. *Phys. Rev. Lett.*, 102(13):130602, 2009.

[91] Massimiliano Esposito, Ryoichi Kawai, Katja Lindenberg, and Christian Van den Broeck. Efficiency at maximum power of low-dissipation Carnot engines. *Phys. Rev. Lett.*, 105(15):150603, 2010.

[92] Kay Brandner, Keiji Saito, and Udo Seifert. Thermodynamics of micro-and nano-systems driven by periodic temperature variations. *Phys. Rev. X.*, 5(3):031019, 2015.

[93] Karel Proesmans, Bart Cleuren, and Christian Van den Broeck. Power-efficiency-dissipation relations in linear thermodynamics. *Phys. Rev. Lett.*, 116(22):220601, 2016.

[94] Naoto Shiraishi, Keiji Saito, and Hal Tasaki. Universal trade-off relation between power and efficiency for heat engines. *Phys. Rev. Lett.*, 117(19):190601, 2016.

[95] Yu-Han Ma, Dazhi Xu, Hui Dong, and Chang-Pu Sun. Universal constraint for efficiency and power of a low-dissipation heat engine. *Phys. Rev. E*, 98(4):042112, 2018.

[96] Yu-Han Ma, Ruo-Xun Zhai, Jinfu Chen, CP Sun, and Hui Dong. Experimental test of the $1/\tau$-scaling entropy generation in finite-time thermodynamics. *Phys. Rev. Lett.*, 125(21):210601, 2020.

[97] Harry JD Miller and Mohammad Mehboudi. Geometry of work fluctuations versus efficiency in microscopic thermal machines. *Phys. Rev. Lett.*, 125(26):260602, 2020.

[98] Kay Brandner and Keiji Saito. Thermodynamic geometry of microscopic heat engines. *Phys. Rev. Lett.*, 124(4):040602, 2020.

[99] Olga Movilla Miangolarra, Rui Fu, Amirhossein Taghvaei, Yongxin Chen, and Tryphon T Georgiou. Underdamped stochastic thermodynamic engines in contact with a heat bath with arbitrary temperature profile. *Phys. Rev. E*, 103(6):062103, 2021.

[100] Gentaro Watanabe and Yuki Minami. Finite-time thermodynamics of fluctuations in microscopic heat engines. *Phys. Rev. Res.*, 4(1):L012008, 2022.

[101] Thiago V Acconcia, Marcus VS Bonança, and Sebastian Deffner. Shortcuts to adiabaticity from linear response theory. *Phys. Rev. E*, 92(4):042148, 2015.

[102] Matteo Scandi and Martí Perarnau-Llobet. Thermodynamic length in open quantum systems. *Quantum*, 3:197, 2019.

[103] Kazutaka Takahashi. Shortcuts to adiabaticity applied to nonequilibrium entropy production: an information geometry viewpoint. *New J. Phys.*, 19(11):115007, 2017.

[104] David Guéry-Odelin, Andreas Ruschhaupt, Anthony Kiely, Erik Torrontegui, Sofia Martínez-Garaot, and Juan Gonzalo Muga. Shortcuts to adiabaticity: Concepts, methods, and applications. *Rev. Mod. Phys*, 91(4):045001, 2019.

[105] David Guéry-Odelin, Chris Jarzynski, Carlos A Plata, Antonio Prados, and Emmanuel Trizac. Driving rapidly while remaining in control: classical shortcuts from Hamiltonian to stochastic dynamics. *Rep. Prog. Phys.*, 86(3), 2023.

[106] Carlos J Bustamante, Yann R Chemla, Shixin Liu, and Michelle D Wang. Optical tweezers in single-molecule biophysics. *Nat. Rev. Methods Primers*, 1(1):1–29, 2021.

[107] Paolo Polimeno, Alessandro Magazzu, Maria Antonia Iati, Francesco Patti, Rosalba Saija, Cristian Degli Esposti Boschi, Maria Grazia Donato, Pietro G Gucciardi, Philip H Jones, Giovanni Volpe, et al. Optical tweezers and their applications. *J. Quant. Spectrosc. Radiat. Transf.*, 218:131–150, 2018.

[108] Jeffrey R Moffitt, Yann R Chemla, Steven B Smith, and Carlos Bustamante. Recent advances in optical tweezers. *Annu. Rev. Biochem.*, 77:205–228, 2008.

[109] Avinash Kumar and John Bechhoefer. Nanoscale virtual potentials using optical tweezers. *Appl. Phys. Lett.*, 113(18):183702, 2018.

[110] Avinash Kumar and John Bechhoefer. Shaping arbitrary energy landscapes with feedback. *Physics in Canada*, 75(1), 2019.

[111] Momčilo Gavrilov and John Bechhoefer. Feedback traps for virtual potentials. *Philos. Transact. A Math. Phys. Eng. Sci.*, 375(2088):20160217, 2017.

[112] Yonggun Jun, Momčilo Gavrilov, and John Bechhoefer. High-precision test of Landauer's principle in a feedback trap. *Phys. Rev. Lett.*, 113(19):190601, 2014.

[113] Momčilo Gavrilov and John Bechhoefer. Erasure without work in an asymmetric double-well potential. *Phys. Rev. Lett.*, 117(20):200601, 2016.

[114] Tushar K Saha, Joseph NE Lucero, Jannik Ehrich, David A Sivak, and John Bechhoefer. Maximizing power and velocity of an information engine. *Proc. Natl. Acad. Sci. U.S.A.*, 118(20):e2023356118, 2021.

[115] Tushar K Saha, Joseph NE Lucero, Jannik Ehrich, David A Sivak, and John Bechhoefer. Bayesian information engine that optimally exploits noisy measurements. *Phys. Rev. Lett.*, 129(13):130601, 2022.

[116] Tushar K Saha, Jannik Ehrich, Momčilo Gavrilov, Susanne Still, David A Sivak, and John Bechhoefer. Information engine in a nonequilibrium bath. *ArXiv preprint ArXiv:2208.00288*, 2022.

[117] Krishna Neupane, Ajay P Manuel, John Lambert, and Michael T Woodside. Transition-path probability as a test of reaction-coordinate quality reveals DNA hairpin folding is a one-dimensional diffusive process. *J. Phys. Chem. Lett*, 6(6):1005–1010, 2015.

[118] Jeongmin Hong, Brian Lambson, Scott Dhuey, and Jeffrey Bokor. Experimental test of Landauer's principle in single-bit operations on nanomagnetic memory bits. *Sci. Adv.*, 2(3):e1501492, 2016.

[119] Stefano Bo, Erik Aurell, Ralf Eichhorn, and Antonio Celani. Optimal stochastic transport in inhomogeneous thermal environments. *EPL (Europhysics Letters)*, 103(1):10010, 2013.

[120] Gavin E Crooks. Path-ensemble averages in systems driven far from equilibrium. *Phys. Rev. E*, 61(3):2361, 2000.

[121] Sosuke Ito. Geometric thermodynamics for the fokker-planck equation: Stochastic thermodynamic links between information geometry and optimal transport. *ArXiv preprint ArXiv:2209.00527*, 2022.

[122] David Abreu and Udo Seifert. Extracting work from a single heat bath through feedback. *Europhys. Lett.*, 94(1):10001, 2011.

[123] Ingram Olkin and Friedrich Pukelsheim. The distance between two random vectors with given dispersion matrices. *Linear Algebr. Appl.*, 48:257–263, 1982.

[124] Andreas Dechant and Yohei Sakurai. Thermodynamic interpretation of Wasserstein distance. *ArXiv preprint ArXiv:1912.08405*, 2019.

[125] David A. Sivak and Gavin E. Crooks. Thermodynamic metrics and optimal paths. *Phys. Rev. Lett.*, 108:190602, 2012.

[126] Dibyendu Mandal and Christopher Jarzynski. Analysis of slow transitions between nonequilibrium steady states. *J. Stat. Mech. Theory Exp.*, 2016(6):063204, 2016.

[127] Patrick R Zulkowski, David A Sivak, and Michael R DeWeese. Optimal control of transitions between nonequilibrium steady states. *PloS One*, 8(12):e82754, 2013.

[128] Steven J Large, Raphaël Chetrite, and David A Sivak. Stochastic control in microscopic nonequilibrium systems. *Europhys. Lett.*, 124(2):20001, 2018.

[129] Yoshitsugu Oono and Marco Paniconi. Steady state thermodynamics. *Progress of Theoretical Physics Supplement*, 130:29–44, 1998.

[130] Takahiro Hatano and Shin-ichi Sasa. Steady-state thermodynamics of Langevin systems. *Phys. Rev. Lett.*, 86(16):3463, 2001.

[131] Thomas Speck and Udo Seifert. Integral fluctuation theorem for the housekeeping heat. *J. Phys. A Math. Gen.*, 38(34):L581, 2005.

[132] Hao Ge. Extended forms of the second law for general time-dependent stochastic processes. *Phys. Rev. E*, 80(2):021137, 2009.

[133] Hao Ge and Hong Qian. Physical origins of entropy production, free energy dissipation, and their mathematical representations. *Phys. Rev. E*, 81(5):051133, 2010.

[134] Lorenzo Bertini, Davide Gabrielli, Giovanni Jona-Lasinio, and Claudio Landim. Thermodynamic transformations of nonequilibrium states. *J. Stat. Phys.*, 149(5):773–802, 2012.

[135] L Bertini, D Gabrielli, G Jona-Lasinio, and C Landim. Clausius inequality and optimality of quasistatic transformations for nonequilibrium stationary states. *Phys. Rev. Lett.*, 110(2):020601, 2013.

[136] Lorenzo Bertini, Alberto De Sole, Davide Gabrielli, Giovanni Jona-Lasinio, and Claudio Landim. Quantitative analysis of the Clausius inequality. *J. Stat. Mech. Theory Exp.*, 2015(10):P10018, 2015.

[137] J Nulton, P Salamon, Bjarne Andresen, and Qi Anmin. Quasistatic processes as step equilibrations. *J. Chem. Phys.*, 83(1):334–338, 1985.

[138] Vytautas Gapsys, Servaas Michielssens, Jan Henning Peters, Bert L. de Groot, and Hadas Leonov. Calculation of binding free energies. In Andreas Kukol, editor, *Molecular Modeling of Proteins*, pages 173–209. Springer New York, New York, NY, 2015.

[139] Christina EM Schindler, Hannah Baumann, Andreas Blum, Dietrich Böse, Hans-Peter Buchstaller, Lars Burgdorf, Daniel Cappel, Eugene Chekler, Paul Czodrowski, Dieter Dorsch, et al. Large-scale assessment of binding free energy calculations in active drug discovery projects. *J. Chem. Inf. Model*, 2020.

[140] Bernd Kuhn, Michal Tichý, Lingle Wang, Shaughnessy Robinson, Rainer E Martin, Andreas Kuglstatter, J org Benz, Maude Giroud, Tanja Schirmeister, Robert Abel, et al. Prospective evaluation of free energy calculations for the prioritization of cathepsin l inhibitors. *J. Med. Chem*, 60(6):2485–2497, 2017.

[141] Myriam Ciordia, Laura Pérez-Benito, Francisca Delgado, Andrés A Trabanco, and Gary Tresadern. Application of free energy perturbation for the design of bace1 inhibitors. *J. Chem. Inf. Model*, 56(9):1856–1871, 2016.

[142] Lingle Wang, Yujie Wu, Yuqing Deng, Byungchan Kim, Levi Pierce, Goran Krilov, Dmitry Lupyan, Shaughnessy Robinson, Markus K Dahlgren, Jeremy Greenwood, et al. Accurate and reliable prediction of relative ligand binding potency in prospective drug discovery by way of a modern free-energy calculation protocol and force field. *J. Am. Chem. Soc.*, 137(7):2695–2703, 2015.

[143] Matteo Aldeghi, Vytautas Gapsys, and Bert L de Groot. Accurate estimation of ligand binding affinity changes upon protein mutation. *ACS Cent. Sci.*, 4(12):1708–1718, 2018.

[144] John D Chodera, David L Mobley, Michael R Shirts, Richard W Dixon, Kim Branson, and Vijay S Pande. Alchemical free energy methods for drug discovery: progress and challenges. *Curr. Opin. Struc. Biol.*, 21(2):150–160, 2011.

[145] Andrew Pohorille, Christopher Jarzynski, and Christophe Chipot. Good practices in free-energy calculations. *J. Phys. Chem. B*, 114(32):10235–10253, 2010.

[146] Jeff Gore, Felix Ritort, and Carlos Bustamante. Bias and error in estimates of equilibrium free-energy differences from nonequilibrium measurements. *Proc. Natl. Acad. Sci. U.S.A*, 100(22):12564–12569, 2003.

[147] Daniel K Shenfeld, Huafeng Xu, Michael P Eastwood, Ron O Dror, and David E Shaw. Minimizing thermodynamic length to select intermediate states for free-energy calculations and replica-exchange simulations. *Phys. Rev. E*, 80(4):046705, 2009.

[148] David D. L. Minh. Alchemical grid dock (algdock): Binding free energy calculations between flexible ligands and rigid receptors. *J. Comput. Chem.*, 41(7):715–730, 2020.

[149] Tri T Pham and Michael R Shirts. Identifying low variance pathways for free energy calculations of molecular transformations in solution phase. *J. Chem. Phys.*, 135(3):034114, 2011.

[150] Tri T Pham and Michael R Shirts. Optimal pairwise and non-pairwise alchemical pathways for free energy calculations of molecular transformation in solution phase. *J. Chem. Phys.*, 136(12):124120, 2012.

[151] Soohyung Park and Wonpil Im. Theory of adaptive optimization for umbrella sampling. *J. Chem. Theory Comput.*, 10(7):2719–2728, 2014.

[152] Charles H Bennett. Efficient estimation of free energy differences from Monte Carlo data. *J. Comput. Phys.*, 22(2):245–268, 1976.

[153] Michael R Shirts, Eric Bair, Giles Hooker, and Vijay S Pande. Equilibrium free energies from nonequilibrium measurements using maximum-likelihood methods. *Phys. Rev. Lett.*, 91(14):140601, 2003.

[154] Paul Maragakis, Martin Spichty, and Martin Karplus. Optimal estimates of free energies from multistate nonequilibrium work data. *Phys. Rev. Lett.*, 96(10):100602, 2006.

[155] Seongjin Kim, Yong Woon Kim, Peter Talkner, and Juyeon Yi. Comparison of free-energy estimators and their dependence on dissipated work. *Phys. Rev. E*, 86(4):041130, 2012.

[156] Michael R Shirts and Vijay S Pande. Comparison of efficiency and bias of free energies computed by exponential averaging, the Bennett acceptance ratio, and thermodynamic integration. *J. Chem. Phys.*, 122(14):144107, 2005.

[157] Michael R Shirts and David L Mobley. An introduction to best practices in free energy calculations. In *Biomolecular Simulations*, pages 271–311. Springer, 2013.

[158] Yinglong Miao and J Andrew McCammon. Unconstrained enhanced sampling for free energy calculations of biomolecules: a review. *Mol. Simul.*, 42(13):1046–1055, 2016.

[159] William P Reinhardt and John E Hunter III. Variational path optimization and upper and lower bounds to free energy changes via finite time minimization of external work. *J. Chem. Phys.*, 97(2):1599–1601, 1992.

[160] John E Hunter III, William P Reinhardt, and Thomas F Davis. A finite-time variational method for determining optimal paths and obtaining bounds on free energy changes from computer simulations. *J. Chem. Phys.*, 99(9):6856–6864, 1993.

[161] Cristina Jarque and Bruce Tidor. Computing bounds on free energy changes with one and two dimensional paths. *J. Phys. Chem. B*, 101(45):9402–9409, 1997.

[162] JC Schön. A thermodynamic distance criterion of optimality for the calculation of free energy changes from computer simulations. *J. Chem. Phys.*, 105(22):10072–10083, 1996.

[163] Mark A Miller and William P Reinhardt. Efficient free energy calculations by variationally optimized metric scaling: Concepts and applications to the volume dependence of cluster free energies and to solid–solid phase transitions. *J. Chem. Phys.*, 113(17):7035–7046, 2000.

[164] Peter L Antonelli, Roman S Ingarden, and Makoto Matsumoto. *The theory of sprays and Finsler spaces with applications in physics and biology*, volume 58. Springer Science & Business Media, 2013.

[165] Nobutaka Hirokawa, Yasuko Noda, Yosuke Tanaka, and Shinsuke Niwa. Kinesin superfamily motor proteins and intracellular transport. *Nat. Rev. Mol. Cell Biol.*, 10(10):682–696, 2009.

[166] Wolfgang Junge and Nathan Nelson. ATP synthase. *Annu. Rev. Biochem.*, 84:631–657, 2015.

[167] Philipp Geiger and Christoph Dellago. Optimum protocol for fast-switching free-energy calculations. *Phys. Rev. E*, 81(2):021127, 2010.

[168] Alexandre P. Solon and Jordan M. Horowitz. Phase transition in protocols minimizing work fluctuations. *Phys. Rev. Lett.*, 120:180605, 2018.

[169] David A Pearlman and Peter A Kollman. A new method for carrying out free energy perturbation calculations: dynamically modified windows. *J. Chem. Phys*, 90(4):2460–2470, 1989.

[170] Nandou Lu and David A Kofke. Optimal intermediates in staged free energy calculations. *J. Chem. Phys*, 111(10):4414–4423, 1999.

[171] Randall J Radmer and Peter A Kollman. Free energy calculation methods: a theoretical and empirical comparison of numerical errors and a new method qualitative estimates of free energy changes. *J. Comput. Chem*, 18(7):902–919, 1997.

[172] Di Wu and David A Kofke. Phase-space overlap measures. II. design and implementation of staging methods for free-energy calculations. *J. Chem. Phys*, 123(8):084109, 2005.

[173] Yuji Sugita, Akio Kitao, and Yuko Okamoto. Multidimensional replica-exchange method for free-energy calculations. *J. Chem. Phys*, 113(15):6042–6051, 2000.

[174] David J Earl and Michael W Deem. Parallel tempering: Theory, applications, and new perspectives. *Phys. Chem. Chem. Phys*, 7(23):3910–3916, 2005.

[175] David A Kofke. On the acceptance probability of replica-exchange Monte Carlo trials. *J. Chem. Phys*, 117(15):6911–6914, 2002.

[176] Cristian Predescu, Mihaela Predescu, and Cristian V Ciobanu. The incomplete beta function law for parallel tempering sampling of classical canonical systems. *J. Chem. Phys*, 120(9):4119–4128, 2004.

[177] Aminata Kone and David A Kofke. Selection of temperature intervals for parallel-tempering simulations. *J. Chem. Phys*, 122(20):206101, 2005.

[178] Nitin Rathore, Manan Chopra, and Juan J de Pablo. Optimal allocation of replicas in parallel tempering simulations. *J. Chem. Phys*, 122(2):024111, 2005.

[179] Cristian Predescu, Mihaela Predescu, and Cristian V Ciobanu. On the efficiency of exchange in parallel tempering Monte Carlo simulations. *J. Phys. Chem. B*, 109(9):4189–4196, 2005.

[180] Walter Nadler and Ulrich HE Hansmann. Dynamics and optimal number of replicas in parallel tempering simulations. *Phys. Rev. E*, 76(6):065701, 2007.

[181] John D Chodera and Michael R Shirts. Replica exchange and expanded ensemble simulations as gibbs sampling: Simple improvements for enhanced mixing. *J. Chem. Phys.*, 135(19):194110, 2011.

[182] Robert M Dirks, Huafeng Xu, and David E Shaw. Improving sampling by exchanging Hamiltonians with efficiently configured nonequilibrium simulations. *J. Chem. Theory Comput.*, 8(1):162–171, 2012.

[183] Justin L MacCallum, Mir Ishruna Muniyat, and Kari Gaalswyk. Online optimization of total acceptance in Hamiltonian replica exchange simulations. *J. Phys. Chem. B*, 122(21):5448–5457, 2018.

[184] David Ruelle. General linear response formula in statistical mechanics, and the fluctuation-dissipation theorem far from equilibrium. *Phys. Lett. A*, 245(3-4):220–224, 1998.

[185] Matteo Colangeli, Christian Maes, and Bram Wynants. A meaningful expansion around detailed balance. *J. Phys. A*, 44(9):095001, 2011.

[186] Umberto Marini Bettolo Marconi, Andrea Puglisi, Lamberto Rondoni, and Angelo Vulpiani. Fluctuation–dissipation: response theory in statistical physics. *Phys. Rep.*, 461(4-6):111–195, 2008.

[187] Christophe Chipot and Tony Lelièvre. Enhanced sampling of multidimensional free-energy landscapes using adaptive biasing forces. *SIAM J. Appl. Math*, 71(5):1673–1695, 2011.

[188] Christoph Dellago and Gerhard Hummer. Computing equilibrium free energies using non-equilibrium molecular dynamics. *Entropy*, 16(1):41–61, 2014.

[189] Maddalena Venturoli, Eric Vanden-Eijnden, and Giovanni Ciccotti. Kinetics of phase transitions in two dimensional Ising models studied with the string method. *J. Math. Chem.*, 45:188–222, 2009.

[190] Felix Ritort, Carlos Bustamante, and I Tinoco. A two-state kinetic model for the unfolding of single molecules by mechanical force. *Proc. Natl. Acad. Sci. U.S.A*, 99(21):13544–13548, 2002.

[191] Tom Conte, Erik DeBenedictis, Natesh Ganesh, Todd Hylton, John Paul Strachan, R Stanley Williams, Alexander Alemi, Lee Altenberg, Gavin Crooks, James Crutchfield, et al. Thermodynamic computing. *ArXiv preprint ArXiv:1911.01968*, 2019.

[192] Hongyun Wang and G Oster. The Stokes efficiency for molecular motors and its applications. *Europhys. Lett.*, 57(1):134, 2002.

[193] Peter E Kloeden and Eckhard Platen. Stochastic differential equations. In *Numerical Solution of Stochastic Differential Equations*, pages 103–160. Springer, 1992.

[194] Sanghyun Park, Fatemeh Khalili-Araghi, Emad Tajkhorshid, and Klaus Schulten. Free energy calculation from steered molecular dynamics simulations using Jarzynski's equality. *J. Chem. Phys.*, 119(6):3559–3566, 2003.

[195] Sanghyun Park and Klaus Schulten. Calculating potentials of mean force from steered molecular dynamics simulations. *J. Chem. Phys.*, 120(13):5946–5961, 2004.

[196] Yinglong Miao, Victoria A Feher, and J Andrew McCammon. Gaussian accelerated molecular dynamics: unconstrained enhanced sampling and free energy calculation. *J. Chem. Theory Comput*, 11(8):3584–3595, 2015.

[197] Jinan Wang, Pablo R Arantes, Apurba Bhattarai, Rohaine V Hsu, Shristi Pawnikar, Yu-ming M Huang, Giulia Palermo, and Yinglong Miao. Gaussian accelerated molecular dynamics: Principles and applications. *Wiley Interdiscip. Rev. Comput. Mol. Sci*, 11(5):e1521, 2021.

[198] Xiaohui Wang, Xingzhao Tu, Boming Deng, John ZH Zhang, and Zhaoxi Sun. Bar-based optimum adaptive steered MD for configurational sampling. *J. Comput. Chem.*, 40(12):1270–1289, 2019.

[199] Andreas Mecklenfeld and Gabriele Raabe. Efficient solvation free energy simulations: impact of soft-core potential and a new adaptive λ-spacing method. *Mol. Phys.*, 115(9-12):1322–1334, 2017.

[200] Matthew P Leighton and David A Sivak. Dynamic and thermodynamic bounds for collective motor-driven transport. *ArXiv preprint ArXiv:2202.13992*, 2022.

[201] Marc Rico-Pasto, Regina K Schmitt, Marco Ribezzi-Crivellari, Juan MR Parrondo, Heiner Linke, Jonas Johansson, and Felix Ritort. Dissipation reduction and information-to-measurement conversion in DNA pulling experiments with feedback protocols. *Phys. Rev. X*, 11(3):031052, 2021.

[202] Alberto Rolandi, Martí Perarnau-Llobet, and Harry JD Miller. Optimal control of dissipation and work fluctuations for rapidly driven systems. *ArXiv preprint ArXiv:2212.03927*, 2022.

[203] Robert B Best and Gerhard Hummer. Coordinate-dependent diffusion in protein folding. *Proc. Natl. Acad. Sci. U.S.A.*, 107(3):1088–1093, 2010.

[204] Gerhard Hummer. Position-dependent diffusion coefficients and free energies from Bayesian analysis of equilibrium and replica molecular dynamics simulations. *New J. Phys.*, 7(1):34, 2005.

[205] Krishna Neupane, Ajay P Manuel, and Michael T Woodside. Protein folding trajectories can be described quantitatively by one-dimensional diffusion over measured energy landscapes. *Nat. Phys.*, 12(7):700–703, 2016.

[206] Daniel AN Foster, Rafayel Petrosyan, Andrew GT Pyo, Armin Hoffmann, Feng Wang, and Michael T Woodside. Probing position-dependent diffusion in folding reactions using single-molecule force spectroscopy. *Biophys. J.*, 114(7):1657–1666, 2018.

[207] Jorge Chahine, Ronaldo J Oliveira, Vitor BP Leite, and Jin Wang. Configuration-dependent diffusion can shift the kinetic transition state and barrier height of protein folding. *Proc. Natl. Acad. Sci. U.S.A.*, 104(37):14646–14651, 2007.

[208] Karel Proesmans. Precision-dissipation trade-off for driven stochastic systems. *ArXiv preprint ArXiv:2203.00428*, 2022.

[209] Jannik Ehrich and David A Sivak. Energy and information flows in autonomous systems. *ArXiv preprint ArXiv:2209.10644*, 2022.

[210] A Imparato, L Peliti, G Pesce, G Rusciano, and A Sasso. Work and heat probability distribution of an optically driven Brownian particle: Theory and experiments. *Phys. Rev. E*, 76(5):050101, 2007.

[211] Elena Sellentin, Miguel Quartin, and Luca Amendola. Breaking the spell of gaussianity: forecasting with higher order Fisher matrices. *Mon. Not. R. Astron. Soc.*, 441(2):1831–1840, 2014.

[212] David M Goldberg and David J Bacon. Galaxy-galaxy flexion: Weak lensing to second order. *Astrophys. J*, 619(2):741, 2005.

[213] DJ Bacon, DM Goldberg, BTP Rowe, and AN Taylor. Weak gravitational flexion. *Mon. Not. R. Astron. Soc.*, 365(2):414–428, 2006.

[214] Roy J Glauber. Time-dependent statistics of the Ising model. *J. Math. Phys.*, 4(2):294–307, 1963.

APPENDICES

Appendix A

Numerical Methods

A.1 Overdamped Dynamics

Brownian dynamics simulations in chapters 6-9 are of one-dimensional overdamped dynamics where the system position x obeys

$$\frac{\mathrm{d}x(t)}{\mathrm{d}t} = -\beta D \frac{\partial V_{\mathrm{tot}}(x,t)}{\partial x} + \sqrt{2D}\,\eta \;, \tag{A.1}$$

for standard Gaussian white noise η. This is then solved numerically according to the Euler–Maruyama method[193] where the time steps are discretized as $x(t) \to x_j$ and $t \to t_j$ for the position and time respectively.

For an equilibrium initial condition, the initial position x_0 is randomly drawn from the equilibrium distribution
$\pi_0(x) = \exp[-\beta V_{\mathrm{tot}}(x,0)]/Z_0$ with $Z_0 = \int_{-\infty}^{\infty} \mathrm{d}x \exp[-\beta V_{\mathrm{tot}}(x,0)]$. For Gaussian distributions this is easily achieved from using built-in random number generators.[193]

For non-Gaussian distributions (chapter 9), a random sample from the initial distribution is found by inverse transform sampling: given a cumulative distribution function $\Pi(x) \equiv \int_{-\infty}^{x} \mathrm{d}x\, \pi(x)$, quantile function $\mathcal{Q} = \Pi^{-1}$, and a uniform random variable $Y_1 \in [0,1]$, the random variable $X = \mathcal{Q}(Y_1)$ has the cumulative distribution $\Pi(x)$. The cumulative distribution and quantile functions can be computed, a random number drawn from the uniform distribution, and the initial sample generated by numerically solving $X = \mathcal{Q}(Y_1)$ for initial sample X.

Once the initial sample is drawn, the solution is propagated forward as

$$X_{j+1} = X_j + a\,(X_j, t_j)\,dt + b\,(X_j, \tau_j)\,\eta_j \;, \tag{A.2}$$

where $a(x,t) = -\beta D \partial V_{\text{tot}}(x,t)/\partial x$, $b(x,t) = \sqrt{2D}$, and η_j is an identically distributed random variable with 0 mean and covariance $\langle \eta_j \eta_k \rangle = \delta_{jk} dt$. This is iterated for n_1 steps until the total time elapsed is $n_1 dt = \Delta t$. This procedure yields a single trajectory and is performed n_2 times to estimate averages of quantities. The n_2 trajectories are independent and therefore can be efficiently computed in parallel. The time step dt is chosen to be sufficiently small that further decreasing it changes the curves/markers by less than the size of the markers and curves on final figures. The number n_2 of trajectories is chosen to be sufficiently large such that bootstrap-resampled 95% confidence bounds are smaller than the markers or curves on final figures.

Typical run times on a single computer are on the order of minutes to generate figures shown in this thesis, and seconds or less to compute individual averages.

A.2 Full Control

The time-dependent probability distributions under full control in chapter 9 are computed by linearly interpolating between the initial and final quantile functions for one-dimensional systems. The quantile functions are computed by first integrating the initial and final distributions to determine the cumulative distribution $P(x) = \int_{-\infty}^{x} \mathrm{d}x\, p(x)$ which is then numerically inverted to determine the corresponding quantile function $\mathcal{Q} = P^{-1}$. Once the initial $\mathcal{Q}_{\text{i}}$ and final $\mathcal{Q}_{\text{f}}$ quantile functions are known, the intermediate quantiles $\mathcal{Q}_t$ are determined by linear interpolation between the initial and final quantiles. This yields the optimal-transport solution for the time-dependent quantile function. The time-dependent quantile function is then numerically inverted, $P_t = \mathcal{Q}_t^{-1}$, and differentiated, $p_t(x) = \partial P_t(x)/\partial x$, to determine the optimal-transport solution for the time-dependent probability distribution. Finally, the total potential can be computed according to (4.5), the entropy production by (4.4), and work from (9.16).

For constrained final distributions (CFDs) this is sufficient for determining the optimal-transport solution; however, to compute the optimal transport solution for constrained final control parameters (CFCP), an optimization over the final distribution must be performed. To do this I perform stochastic gradient descent similar to the method described in Ref. 168 for computing minimum-work-variance protocols. I compute the CFD protocol as described above and compute the work from (9.16) before adding a small point perturbation ϵ to the final distribution $p_{\text{f,new}}(x) = c[p_{\text{f}}(x) + \epsilon \delta(x - Y_2)]$, where c maintains normalization and $Y_2 \in [a,b]$ is a uniform random variable with $[a,b]$ spanning the available space in x. Equation (9.16) is then computed for the new distribution and the change to the final distribution is accepted if work has decreased. For numerical calculations, all continuous distributions are approximated by discrete grids of points and delta functions as perturbation to a single grid point.

This method is iterated until work has converged to within an amount smaller than the size of markers in the final figure. The perturbation size ϵ and discretization of the distribution are chosen such that estimated errors in the work are smaller than the markers. This method is most efficient when starting from a good initial guess for the final distribution, which is achieved by starting from known solutions in the slow limit (where the optimal final distribution is the final equilibrium distribution) to find the solution for long duration and slowly decreasing the duration until the fast limit is reached. At each duration, the optimal final distribution is found, this is then used as the initial guess for the next shorter protocol duration. This is compared with the solutions found starting from the fast limit (where the optimal final distribution is the initial equilibrium distribution) and increasing duration to the slow limit. The difference between the two is smaller than the markers and curves shown in all final figures. To check for robustness, a subset of the solutions were compared with solutions starting from uniform distributions, which gave consistent results.

Typical run times on a single computer are on the order of minutes to generate figures shown in this thesis, and seconds or less to compute CFCP protocols.

Appendix B

Skewed Thermodynamic Geometry

This appendix presents supporting information for chapter 6, including explicit expressing for the frictions (B.4a), analysis of finite integration bounds, and a discussion on Finsler geometry.

B.1 Breathing Harmonic Trap

A simple non-trivial system for designing and testing minimum-variance and minimum-bias protocols is the breathing harmonic trap, since its correlation functions can be calculated analytically and it has a non-Gaussian work distribution. Consider a colloidal particle in a harmonic trap with variable stiffness. The particle position x obeys the overdamped Langevin equation,

$$\frac{\mathrm{d}x}{\mathrm{d}t} = -\beta D k(t) x + \sqrt{2D}\,\eta, \tag{B.1}$$

in a trap of time-dependent strength $k(t)$. The control parameter is the trap strength $\lambda = k$, so the conjugate force is $f \equiv -\partial U/\partial k = -\frac{1}{2}x^2$. The joint probability distribution of the particle position and work obeys[168,210]

$$\frac{\partial p(x,w,t)}{\partial t} = -\frac{1}{2}\frac{\mathrm{d}k(t)}{\mathrm{d}t}x^2\frac{\partial p(x,w,t)}{\partial w} + D\frac{\partial}{\partial x}\left[\beta k(t) x p(x,w,t) + \frac{\partial p(x,w,t)}{\partial x}\right]. \tag{B.2}$$

From this, any moment of either the work or position distribution can be calculated, subject to an initial equilibrium condition

$$p(x, w, t = 0) = \pi(x|k_\mathrm{i})\delta(w) \tag{B.3a}$$
$$= [2\pi/(\beta k_\mathrm{i})]^{-1/2} \exp\{-\beta k_\mathrm{i} x^2/2\}\delta(w) \tag{B.3b}$$

with $\delta(w)$ the Dirac delta function.

The force variance (6.19), the Stokes' (6.4) and the supra-Stokes' coefficients (6.6), and the third integral covariance function (6.8) are

$$\langle \delta f^2 \rangle_{k(t)} = \frac{1}{2k^2} \tag{B.4a}$$
$$\zeta[k(t)] = \frac{1}{4Dk^3} \tag{B.4b}$$
$$\zeta^{(2)}[k(t)] = \frac{1}{2D^2k^5} \tag{B.4c}$$
$$\mathcal{C}^{(3)}[k(t), t] \approx \frac{3\beta t}{16Dk^6} + \frac{51}{32D^2k^7} \ , \tag{B.4d}$$

respectively. In (B.4d), terms of order t^{-n} for $n \geq 1$ are neglected. For one-dimensional control, the minimum-variance (precise) and minimum-bias (accurate) protocols that minimize Eq. (6.25b) and (6.26b), respectively can be found analytically. The force-variance-optimized protocol proceeds at velocity $\dot{k} \propto k$, minimum-variance protocol at $\dot{k} \propto k^{3/2}$, and minimum-bias protocol at $\dot{k} \propto k^{5/3}$.

As a simple test of the approximations of Eqs. (6.12), (6.13), and (6.18), Fig. B.1 plots the sum and difference of the first three moments of the excess work from forward and reverse protocols. The forward protocol is chosen to be a decrease in the control parameter (decreasing k), and therefore the reverse increases the control parameter (increasing k). In all cases the exact calculations agree with the approximation for slow protocols (large $\Delta t/\tau_\mathrm{f}^{(1)}$ for slowest relaxation time $\tau_\mathrm{f}^{(1)} = \gamma/(2k_\mathrm{f})$), and overestimate for fast protocols (small $\Delta t/\tau_\mathrm{f}^{(1)}$). For large $\Delta t/\tau_\mathrm{f}^{(1)}$, the first and second moments are approximated by (6.12) and (6.13) so the sums ($n = 1$ and 2, (+) in figure) are both approximated by the Stokes' friction (6.4) and decrease as $1/\Delta t$, while the differences ($n = 1$ and 2, (−) in figure) are proportional to the supra-Stokes' tensor (6.6) and decrease as $1/(\Delta t)^2$. The third moment is approximated by (6.18), so the sum ($n = 3$, (+) in figure) is approximated by the third integral covariance (6.8) and decays as $1/(\Delta t)^2$ (due to the term linear in t in (B.4d)) while the difference ($n = 3$, (−) in figure) is proportional to the supra-Stokes tensor and decays as $1/(\Delta t)^2$.

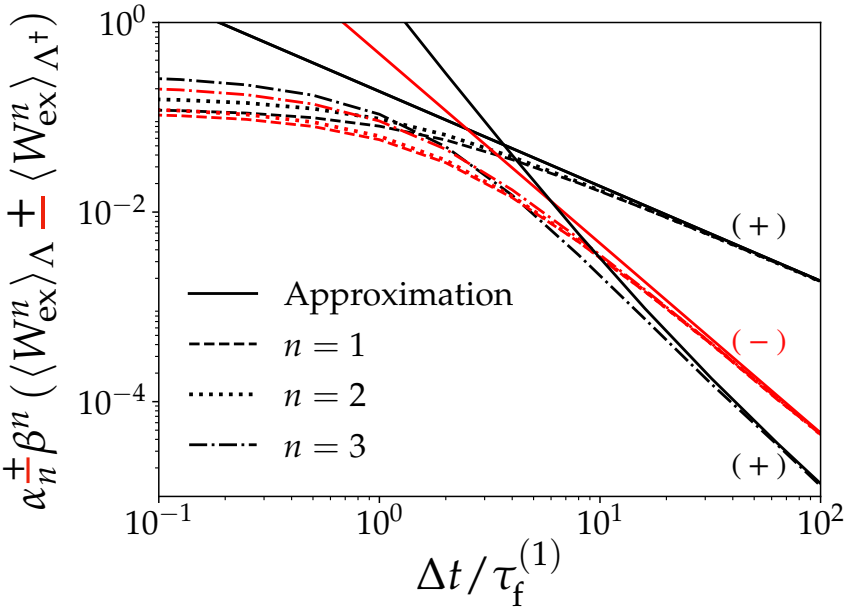

Fig B.1. The sum (black, +) and the difference (red, −) of the moments of excess work for forward and reverse protocols of the breathing harmonic trap, as a function of protocol duration Δt (scaled by the slowest relaxation time $\tau_{\rm f}^{(1)} = (2\beta D k_{\rm f})^{-1}$). Solid lines are the near-equilibrium approximations, given respectively by Eqs. (6.12), (6.13), and (6.18). Dashed ($n = 1$), dotted ($n = 2$), and dash-dotted ($n = 3$) curves show exact results. The protocol $k(t)$ is linear with $k_{\rm f}/k_{\rm i} = 1/2$. The coefficients $\alpha_1^+ = 1/2$, $\alpha_1^- = 2$, $\alpha_2^+ = 1/4$, $\alpha_2^- = 1/3$, $\alpha_3^+ = 1/2$, and $\alpha_3^- = 1/4$ are chosen such that any moment approximated by the same friction coefficient collapses onto a single curve. In all cases the exact calculations agree with the approximation for large $\Delta t/\tau_{\rm f}^{(1)}$.

B.2 Finite Integration Bounds

The infinite integration bound on the friction assumes that correlations relax quickly relative to the protocol duration. For the first two moments, despite the finite integration bound generally yielding a more accurate approximation, the infinite bound considerably simplifies the approximation and allows for straightforward protocol optimization.

The effect of finite integration bounds is significant for two calculations: approximation of fourth- and higher-order moments of the excess work, and next-order approximations (including both leading- and next-to-leading-order contributions) for the moments. In the former, one must treat the bound as finite since the n-time covariance functions do not decay to zero for some subspace of large time arguments.

In more detail, consider the four-time covariance (kurtosis) $\langle \delta f_i(0)\delta f_j(t_2)\delta f_k(t_3)\delta f_\ell(t_4)\rangle_{\boldsymbol{\lambda}(t)}$. When any one of the four times $\{0, t_2, t_3, t_4\}$ significantly differs from the others, the conjugate forces decorrelate, and the kurtosis decays to zero; however, when $t_3 \sim t_4 \gg t_2 \sim 0$, any variables separated by significant time decorrelate, and the kurtosis approaches $\langle \delta f_i(0)\delta f_j(t_2)\rangle_{\boldsymbol{\lambda}(t)}\langle \delta f_k(t_3)\delta f_\ell(t_4)\rangle_{\boldsymbol{\lambda}(t)}$. This limit represents a plane in the (t_2, t_3, t_4) parameter space where the kurtosis asymptotes to a finite value even for large time arguments. Substituting the above into (6.8) for $n = 4$ yields the integral four-time covariance in the limit $t_3 \sim t_4 \gg t_2 \sim 0$,

$$\mathcal{C}^{(3)}_{ijk\ell}[\boldsymbol{\lambda}(t), t] = 3t\, \mathcal{C}^{(1)}_{ij}[\boldsymbol{\lambda}(t), t]\mathcal{C}^{(1)}_{k\ell}[\boldsymbol{\lambda}(t), t] \tag{B.5a}$$

$$= 3t\, \zeta^{(1)}_{ij}[\boldsymbol{\lambda}(t)]\zeta^{(1)}_{k\ell}[\boldsymbol{\lambda}(t)] \ , \quad t \to \infty \ . \tag{B.5b}$$

Since this is the only case that remains finite as $t \to \infty$, the second line is the approximation (to highest order in t) for the integral four-time covariance. Parallel arguments hold for the higher-order moments.

When approximating the average excess work (6.23) with both the Stokes' and supra-Stokes' tensors (6.24), finite integration bounds on the Stokes' friction may be necessary. For finite integration bounds on the Stokes' friction (6.24) is replaced with

$$\mathcal{C}_{ij}[\boldsymbol{\lambda}(t), \dot{\lambda}(t), t] \equiv \mathcal{C}^{(1)}_{ij}[\boldsymbol{\lambda}(t), t] + \frac{1}{4}\zeta^{(2)}_{ijk}[\boldsymbol{\lambda}(t)]\dot{\lambda}_k(t) \ . \tag{B.6}$$

For systems with weakly skewed conjugate-force fluctuation, the contribution from the finite bound on the first term can be comparable in magnitude to the contribution from the supra-Stokes' tensor.

Figures B.2 shows the first and second moments of the excess work for forward and reverse protocols, compared to different approximations. For the mean excess work, the supra-Stokes' tensor contributes with opposite sign from the Stokes' friction for forward

(decreasing k) protocols and with same sign for reverse (increasing k). Since the Stokes'-friction approximation overestimates the excess work in both cases (a,c), adding the supra-Stokes' tensor reduces the accuracy of the approximation for the reverse excess work. This effect is an artifact of the infinite integral bound; indeed, if the bound is kept finite ($\mathcal{C}^{(1)}$ rather than $\zeta^{(1)}$), the first integral autocovariance overestimates excess work for forward protocols and underestimates excess work for reverse protocols, and adding the supra-Stokes' tensor improves the approximation in both cases. Finally, the Stokes' friction does not always overestimate excess work for both forward and reverse protocols. For the second moment in (b,d), the Stokes' friction overestimates excess work for forward protocols and underestimates excess work for reverse protocols, and the supra-Stokes' tensor improves the approximation when either the Stokes' friction or first integral covariance are used.

B.3 Finsler Geometry

The addition of the supra-Stokes' tensor (6.6) comes at the cost of a more complex geometric structure. In contrast to Riemannian geometry, Finsler geometry is not restricted to a quadratic norm. In general, the inner products are not characterized solely by points, but rather by points and directions. Despite this, several useful concepts from Riemannian geometry (notably curvature, length, and geodesics) generalize. There are therefore standard procedures to find the geodesics despite the more complex landscapes induced by the generalized cubic Finsler metric (6.24).[164]

Finsler geometry has several applications in both physics and biology.[164] In the thermodynamic context, the *flexion* tensor[211]

$$\mathcal{F}_{ijk}[\boldsymbol{\lambda}(t)] \equiv \left\langle \frac{\partial^3 \ln \pi(x|\boldsymbol{\lambda})}{\partial\lambda_i \partial\lambda_j \partial\lambda_k} \right\rangle_{\boldsymbol{\lambda}(t)} \tag{B.7}$$

is a Finsler metric arising as the third-order contribution to the near-equilibrium expansion of the relative entropy (Kullback-Leibler divergence) of a probability distribution relative to the equilibrium distribution:[164]

$$D(\pi(x|\boldsymbol{\lambda})||\pi(x'|\boldsymbol{\lambda})|) \equiv \int_{-\infty}^{\infty} \mathrm{d}x\ \pi(x|\boldsymbol{\lambda}) \ln \frac{\pi(x'|\boldsymbol{\lambda})}{\pi(x|\boldsymbol{\lambda})} \tag{B.8a}$$

$$\approx \mathcal{I}_{ij}\Delta\lambda_i\Delta\lambda_j + \mathcal{F}_{ijk}\Delta\lambda_i\Delta\lambda_j\Delta\lambda_k\ . \tag{B.8b}$$

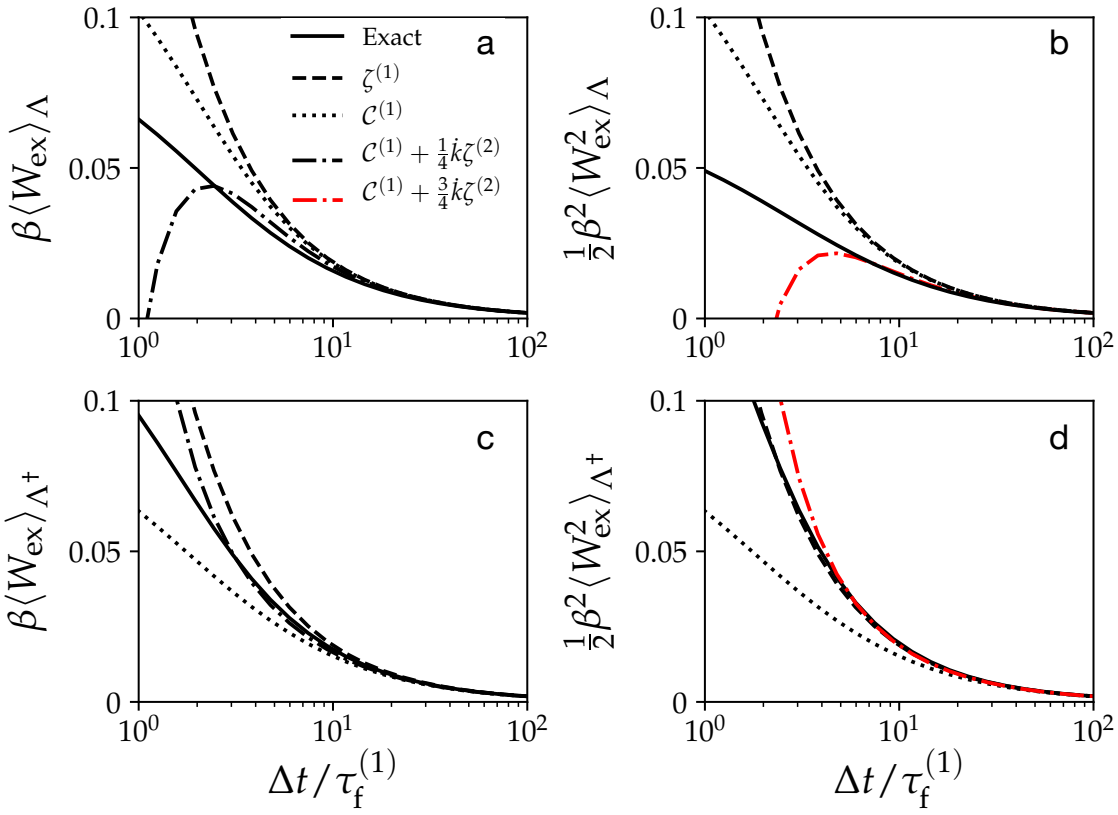

Fig B.2. The first (a/c) and second (b/d) moments of excess works for forward (a,b) and reverse (c,d) protocols of the breathing harmonic trap as a function of protocol time Δt (scaled by the slowest relaxation time $\tau_{\rm f}^{(1)} = (2\beta D k_{\rm f})^{-1}$). The dashed, dotted, and dash-dotted curves are different forms of the near-equilibrium approximation. The protocol $k(t)$ is linear with $k_{\rm f}/k_{\rm i} = 1/2$.

The coskewness tensor (6.21) is related to the flexion tensor by

$$\mathcal{F}_{ijk}[\lambda(t)] = \langle \delta f_i \delta f_j \delta f_k \rangle_{\boldsymbol{\lambda}(t)} + \sum_{\sigma_{ijk}} \left\langle \frac{\partial^2 \ln \pi(x|\lambda)}{\partial \lambda_i \partial \lambda_j} \frac{\partial \ln \pi(x|\lambda)}{\partial \lambda_k} \right\rangle_{\lambda(t)} ,$$

where the sum is over permutations of the indices which yield distinct covariance functions $\sigma_{ijk} = \{123, 132, 321\}$. In weak gravitational lensing[212,213] the flexion tensor is the third-order correction to the shapes of images, which is described as flexing the shape of images from an ellipse towards a banana shape. Similarly, the supra-Stokes' tensor (product of coskewness tensor and integral double relaxation time (6.21)) skews the thermodynamic geometry of minimum-dissipation protocols, as demonstrated in Fig. 6.1.

Appendix C

Fast-Control Model Systems

To support the results of chapter 7, this appendix describes theoretical and numerical calculations for several diverse model systems: translating and breathing harmonic traps, binding and unbinding reactions, and the Ising model.

C.1 Harmonic Trap

Consider a colloidal particle in a harmonic trap with energy $V = \frac{1}{2}k(t)[x - x^{\mathrm{c}}(t)]^2$, for variable trap center $x^{\mathrm{c}}(t)$ and trap stiffness $k(t)$. The particle position x obeys the overdamped Langevin equation,

$$\frac{\mathrm{d}x}{\mathrm{d}t} = -\beta D k(t)[x - x^{\mathrm{c}}(t)] + \sqrt{2D}\,\eta \;, \tag{C.1}$$

The corresponding Fokker-Planck equation (3.1) is

$$\frac{\partial p_\Lambda(x,t)}{\partial t} = L[x, \{k(t), x^{\mathrm{c}}(t)\}]\, p_\Lambda(x,t) \;, \tag{C.2}$$

with time-evolution operator (3.4)

$$L[x, \{k(t), x^{\mathrm{c}}(t)\}] \equiv D\frac{\partial}{\partial x}\left\{\beta k(t)\,[x - x^{\mathrm{c}}(t)] + \frac{\partial}{\partial x}\right\} \;. \tag{C.3}$$

For this system, the two control parameters $x^{\mathrm{c}}(t)$ and $k(t)$ can be treated independently as "translating-trap" and "breathing-trap" models respectively. For the remainder of this appendix I set $\beta = D = 1$.

C.1.1 Translating Trap

In a translating trap, the trap stiffness k is held fixed and the trap center $x^{\mathrm{c}}(t)$ is varied as the control parameter. The conjugate force is therefore $f \equiv -\partial V/\partial x^{\mathrm{c}} = k[x - x^{\mathrm{c}}(t)]$, and the IFRR (7.5b) is

$$R_{x_{\mathrm{i}}^{\mathrm{c}}}[x^{\mathrm{c}}(t)] = k^2[x_{\mathrm{i}}^{\mathrm{c}} - x^{\mathrm{c}}(t)] \ , \tag{C.4}$$

for initial trap center $x_{\mathrm{i}}^{\mathrm{c}}$. Solving (7.11) gives the STEP value

$$x^{\mathrm{c,\ STEP}} = \frac{x_{\mathrm{i}}^{\mathrm{c}} + x_{\mathrm{f}}^{\mathrm{c}}}{2} \ , \tag{C.5}$$

for final trap center $x_{\mathrm{f}}^{\mathrm{c}}$. The STEP jumps the trap center halfway between its initial and final positions, independent of any other system parameters. This is consistent with the exact minimum-dissipation protocol in the fast (short-duration) limit.[41]

C.1.2 Breathing Trap

The breathing trap has fixed trap center ($u = 0$), and time-dependent trap stiffness $k(t)$ as the control parameter. Here the conjugate force is $f \equiv -\partial U/\partial k = -\frac{1}{2}x^2$, so the IFRR (7.5b) is

$$R_{k_{\mathrm{i}}}[k(t)] = 2\left[1 - \frac{k(t)}{k_{\mathrm{i}}}\right] \ , \tag{C.6}$$

for initial stiffness k_{i}. Solving (7.11) gives the STEP value

$$k^{\mathrm{STEP}} = \frac{k_{\mathrm{i}} + k_{\mathrm{f}}}{2} \ , \tag{C.7}$$

where k_{f} is the final trap stiffness. Identical to the translating trap, the STEP jumps to the control-parameter value halfway between the endpoints, independent of other system parameters, consistent with the exact result in the fast (short-duration) limit[41]. The approximate gain (7.13) from the STEP is 3/2, independent of system parameters.

For a slow (long-duration) protocol, the minimum-dissipation protocol is continuous, and can be calculated from the friction coefficient[125]

$$\zeta(k) = \frac{1}{4k^3} \ , \tag{C.8}$$

as $\mathrm{d}k/\mathrm{d}t \propto [\zeta(k)]^{-1/2}$, where the proportionality is set by the control-parameter endpoints. For the interpolated protocol, jumps are added at the beginning and end of respective sizes

$(k^{\mathrm{STEP}} - k_{\mathrm{i}})/(1 + \Delta t/\tau)^{\alpha}$ and $(k_{\mathrm{f}} - k^{\mathrm{STEP}})/(1 + \Delta t/\tau)^{\alpha}$.

C.2 Binding and Unbinding Reaction

I examine a two-state binding/unbinding reaction with binding rate $k_{\mathrm{UB}\to\mathrm{B}}$ and unbinding rate $k_{\mathrm{B}\to\mathrm{UB}}$.[67] I assume the binding rate $k_{\mathrm{UB}\to\mathrm{B}} = k_0$ depends only on the dynamic encounter rate and not on the strength of the chemical potential, and the unbinding rate $k_{\mathrm{B}\to\mathrm{UB}}$ depends on how tightly the molecule is bound, and hence on the chemical-potential difference μ^{chem} between unbound and bound states, as (with $\beta = 1$)

$$k_{\mathrm{B}\to\mathrm{UB}} = k_0 e^{-\mu^{\mathrm{chem}}} \ . \tag{C.9}$$

$\mu^{\mathrm{chem}} = 0$ gives equal binding and unbinding rates, $k_{\mathrm{UB}\to\mathrm{B}} = k_{\mathrm{B}\to\mathrm{UB}}$.

I additionally assume a fixed total number $N_{\mathrm{tot}} = N_{\mathrm{UB}} + N_{\mathrm{B}}$ of molecules, with variable numbers of unbound (N_{UB}) and bound (N_{B}) molecules. The transition-rate matrix is

$$K(\mu^{\mathrm{chem}}) = \begin{bmatrix} k_0 e^{-\mu^{\mathrm{chem}}} & -k_0 \\ -k_0 e^{-\mu^{\mathrm{chem}}} & k_0 \end{bmatrix} \ . \tag{C.10}$$

The excess work for this two-state system driven by a chemical-potential protocol can be solved by numerically integrating

$$\frac{\mathrm{d}\langle N_{\mathrm{B}}\rangle_{\Lambda}}{\mathrm{d}t} = k_0 \left[N_{\mathrm{tot}} - \langle N_{\mathrm{B}}\rangle_{\Lambda} (e^{-\mu^{\mathrm{chem}}(t)} + 1) \right] \ , \tag{C.11}$$

subject to an equilibrium initial condition

$$\langle N_{\mathrm{B}}\rangle_{\mu^{\mathrm{chem}}} = \frac{N_{\mathrm{tot}}}{1 + e^{-\mu^{\mathrm{chem}}}} \ . \tag{C.12}$$

Using (C.11) gives the IFRR (7.5b)

$$R_{\mu_{\mathrm{i}}^{\mathrm{chem}}}[\mu^{\mathrm{chem}}(t)] = -k_0 \left[N_{\mathrm{tot}} - \langle N_{\mathrm{B}}\rangle_{\mu_{\mathrm{i}}^{\mathrm{chem}}} (e^{-\mu^{\mathrm{chem}}(t)} + 1) \right] \ . \tag{C.13}$$

Solving (7.11) gives the STEP value

$$\mu^{\mathrm{chem,STEP}} = \mathcal{W}\left[\left(1 - \frac{N_{\mathrm{tot}}}{\langle N_{\mathrm{B}}\rangle_{\mu_{\mathrm{i}}^{\mathrm{chem}}}} \right) e^{(\mu_{\mathrm{f}}^{\mathrm{chem}} - 1)} \right] + \mu_{\mathrm{f}}^{\mathrm{chem}} - 1 \ , \tag{C.14}$$

where $\mathcal{W}$ is the product log function (Lambert W function), defined as the solution to $\mathcal{W}(z)\exp[\mathcal{W}(z)] = z$. For the special case of $\langle N_{\mathrm{B}}\rangle_{\mu_{\mathrm{i}}^{\mathrm{chem}}} \approx N_{\mathrm{tot}}$ (satisfied as $\mu_{\mathrm{i}}^{\mathrm{chem}} \to \infty$),

the STEP value simplifies to $\mu^{\text{chem,STEP}} \approx \mu_{\text{f}}^{\text{chem}} - 1$. Figure 7.1 shows the STEP for $\mu_{\text{i}}^{\text{chem}} = -3 + \ln 2$ and $\mu_{\text{f}}^{\text{chem}} = 3 + \ln 2$.

In Ref. 67, I derived a simple expressions for the friction

$$\zeta(\mu^{\text{chem}}) = \frac{N_{\text{tot}}}{k_0} \frac{e^{-\mu^{\text{chem}}}}{(1 + e^{-\mu^{\text{chem}}})^3} \ , \tag{C.15}$$

and minimum-dissipation protocol in the slow limit,

$$\frac{\mathrm{d}\mu^{\text{chem}}(t)}{\mathrm{d}t} = \frac{e^{-\mu^{\text{chem}}(t)} \left(e^{\mu_{\text{f}}^{\text{chem}}} - e^{\mu_{\text{i}}^{\text{chem}}} \right)}{\Delta t} \ . \tag{C.16}$$

Equation (C.14) is used to determine an interpolated protocol which satisfies (C.16) with initial jump $(\mu^{\text{chem,STEP}} - \mu_{\text{i}}^{\text{chem}})/(1+\Delta t/\tau)^{\alpha}$ and final jump $(\mu_{\text{f}} - \mu^{\text{chem,STEP}})/(1+\Delta t/\tau)^{\alpha}$.

Figure C.1 shows the benefit from designed protocols compared to naive (constant-velocity) protocols. Consistent with the breathing trap (Fig. 7.3), the difference between the naive and designed work in Fig. C.1 demonstrates the expected $(\Delta t)^{-1}$ scaling of work in the slow (long-duration) limit, (Δt) scaling in the fast (short-duration) limit, and the largest work reduction from designed protocols in the intermediate $(\Delta t/\tau \sim 10)$ regime, achieved by the interpolated protocol. Unlike the breathing trap, for any duration the protocol designed from slow approximations performs better than the naive protocol (seen as a positive difference in Fig. C.1a), but can still be significantly outperformed by a protocol incorporating the fast approximation, as shown by the larger gain from "fast opt" compared to "slow opt" for short protocol duration in Fig. C.1b.

C.3 Single-Spin Ising Model

Consider a single-spin Ising model under the control of an external magnetic field h with Hamiltonian $H(\sigma|h) = -h\sigma$, where $\sigma \in \{-1, 1\}$. The system dynamically evolves according to a master equation with transition-rate matrix

$$K(h) = \begin{bmatrix} -k_1(h) & k_{-1}(h) \\ k_1(h) & -k_{-1}(h) \end{bmatrix} , \tag{C.17}$$

for rates

$$k_1(h) = k_{\text{flip}} \frac{1}{1 + e^{-2\beta h}} \tag{C.18a}$$

$$k_{-1}(h) = k_{\text{flip}} \frac{1}{1 + e^{2\beta h}} \ , \tag{C.18b}$$

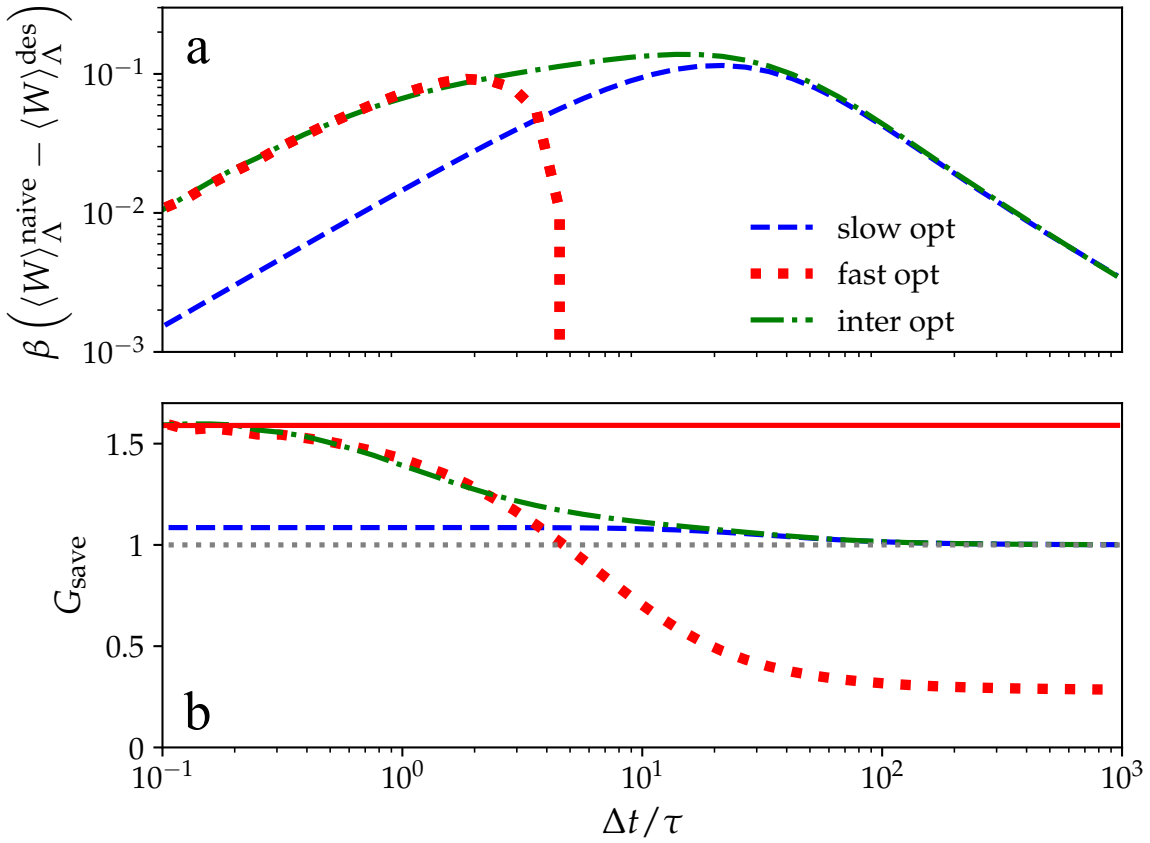

Fig C.1. Benefit in the two-state binding/unbinding reaction system from designed protocols relative to naive (constant-velocity), as a function of total duration Δt scaled by the fastest integral relaxation time τ. The different designed ("des") protocols include the linear-response optimized ("slow opt", dashed blue), STEP ("fast opt", red dots), and interpolated optimal protocol with $\alpha = 1$ ("inter opt", dash-dotted green). (a) Difference between the work in naive (constant-velocity) and designed protocols. (b) Gain $G_{\rm save} \equiv \langle W_{\rm save}\rangle_\Lambda^{\rm des}/\langle W_{\rm save}\rangle_\Lambda^{\rm naive}$ in saved work, with a solid red line denoting the short-duration limit (7.13). Control-parameter endpoints are $\mu_{\rm i}^{\rm chem} = -3 + \ln 2$ and $\mu_{\rm f}^{\rm chem} = 3 + \ln 2$, and the fastest integral relaxation time is $\tau = 1/[k_0(1 + e^{-\mu_{\rm i}^{\rm chem}})]$[67].

where k_{flip} is the rate of spin-flip attempts, and the second RHS factor is the Glauber acceptance probability[214]. The IFRR (7.5b) is

$$R_{h_\text{i}}[h(t)] = \sum_{\sigma\in\{-1,1\}} \sigma K(h(t))\pi_\text{i} \tag{C.19a}$$

$$= k_{\text{flip}} \operatorname{sech}\beta h \ \operatorname{sech}\beta h_\text{i} \ \sinh\beta(h-h_\text{i}) \ , \tag{C.19b}$$

where h_i is the initial magnetic field. The STEP value (7.11) is found by solving the transcendental equation

$$\left[\coth\beta(h^\text{STEP}-h_\text{i}) - \tanh\beta h^\text{STEP}\right]\left(h_\text{f}-h^\text{STEP}\right) = 1 \ . \tag{C.20}$$

From Ref. 125, the generalized friction coefficient $\zeta(h)$ is the product of the equilibrium conjugate-force variance $\langle\delta\sigma^2\rangle_h$ and integral relaxation time $\tau(h) = [k_1(h)+k_{-1}(h)]^{-1} = k_{\text{flip}}^{-1}$, giving

$$\zeta(h) = \beta k_{\text{flip}}^{-1} \operatorname{sech}^2\beta h \ . \tag{C.21}$$

(The relaxation time is derived from the second eigenvalue of the transition-rate matrix (C.17).) In the long-duration limit, this yields the minimum-dissipation protocol

$$\frac{\mathrm{d}h}{\mathrm{d}t} = \frac{2k_\text{B}T}{\Delta t}\left[g\left(\tfrac{1}{2}\beta h_\text{f}\right) - g\left(\tfrac{1}{2}\beta h_\text{i}\right)\right]\cosh\beta h \ , \tag{C.22}$$

where $g(x) \equiv \tan^{-1}[\tanh x]$.

Figure C.2 shows the benefit from designed protocols compared to naive protocols. The results are qualitatively similar to the binding/unbinding reaction system; both are two-state systems with a control parameter that biases the transition rate between the two states, but the rate matrices have different analytical forms.

C.4 Multiparameter Control of Nine-Spin Ising Model

Consider the nine-spin ferromagnetic Ising model depicted in Fig. 7.4. Adjacent spins interact with coupling strength $\beta J = 0.5$, both to the fluctuating spins and fixed-spin boundary conditions. The forces $\mathbf{f} = (m_\text{b}, m_\text{g})$ conjugate to the external magnetic fields $\boldsymbol{h} = (h_\text{b}, h_\text{g})$ are the mean magnetizations of the spins controlled by each field. The spins dynamically evolve according to Glauber dynamics[214].

The IFRR (7.5b) is calculated over the control-parameter space, and the short-time power savings in Fig. 7.4b is obtained from (7.12). Mean works for the naive and de-

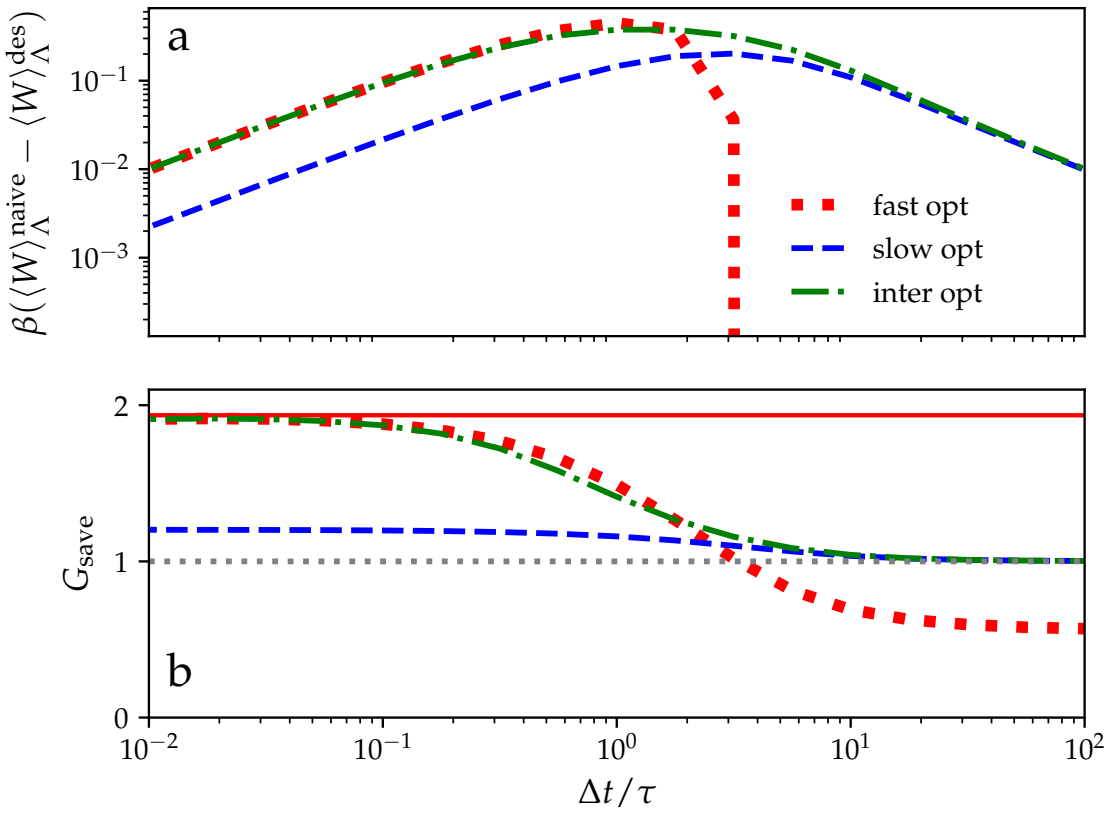

Fig C.2. Benefit in the single-spin Ising model from designed protocols relative to the naive (constant-velocity) protocol, as a function of protocol duration Δt scaled by the integral relaxation time $\tau = k_{\text{flip}}^{-1}$. The different designed ("des") protocols include the linear-response optimized ("slow opt", dashed blue), STEP ("fast opt", red dots), and the interpolated optimal protocol with $\alpha = 1$ ("inter opt", dash-dotted green). (a) Difference between the work by naive (constant-velocity) and by designed ("des") protocols. (b) Gain $G_{\text{save}} \equiv \langle W_{\text{save}}\rangle_\Lambda^{\text{des}} / \langle W_{\text{save}}\rangle_\Lambda^{\text{naive}}$ in saved work, with a solid red line denoting the short-duration limit (7.13). Control-parameter endpoints are $\beta h_{\text{i}} = -2$ and $\beta h_{\text{f}} = 2$.

signed protocols (Fig. 7.4c/d) were calculated by propagating the master equation for protocol durations $\Delta t/\tau$ ranging between 10^{-3} and 10^{3}, with simulation time-step $\mathrm{d}t \in (2 \times 10^{-4}, 2 \times 10^{-1})$, using a fine temporal discretization for short protocol durations and a coarse discretization for long protocol durations.